UNIVERSITY OF WARMIA AND MAZURY IN OLSZTYN

Technical Sciences

20(4) 2017

PUBLISHER UWM

OLSZTYN 2017

The Technical Sciences is indexed and abstracted in BazTech (http://baztech.icm.edu.pl) and in IC Journal Master List (http://journals.indexcopernicus.com)

The Journal is available in electronic form on the web sites
http://www.uwm.edu.pl/techsci (subpage Issues)
http://wydawnictwo.uwm.edu.pl (subpage Czytelnia)

The electronic edition is the primary version of the Journal

PL ISSN 1505-4675
e-ISNN 2083-4527

Address
ul. Jana Heweliusza 14
10-718 Olsztyn-Kortowo, Poland
tel.: +48 89 523 36 61
fax: +48 89 523 34 38
e-mail: wydawca@uwm.edu.pl

Ark. wyd. 8,0, ark. druk. 6,5, nakład 85 egz.
Druk – Zakład Poligraficzny UWM w Olsztynie
zam. nr 22

Contents

Technical Sciences, 2017, 20(4), 321–331

Quarterly peer-reviewed scientific journal
ISSN 1505-4675
e-ISSN 2083-4527
TECHNICAL SCIENCES
Homepage: www.uwm.edu.pl/techsci/

ASSESSMENT OF USEFULNESS OF THE MEMS-BASED INTEGRATED NAVIGATION UNIT IN CAR NAVIGATION

***Marcin Uradziński*[1], *Jacek Rapiński*[1], *Dariusz Tomaszewski*[1], *Michał Śmieja*[2], *Hang Guo*[3], *Songsen Yu*[3], *Xiong Jian*[3]**

[1] Instiute of Geodesy
University of Warmia and Mazury in Olsztyn
[2] Chair of Mechatronics
University of Warmia and Mazury in Olsztyn
[3] Institute of Space Science and Technology
Nanchang University, China

Received 25 March 2016, accepted 28 July 2017, available online 16 August 2017.

Key words: MEMS, inertial navigation, GNSS, GNSS/IMU integration, car navigation.

Abstract

Due to the development of MEMS, there is an opportunity to build a low-cost integrated navigation systems, operating independently of horizon visibility. This paper presents the proposal of an integrated GPS/IMU platform using MEMS technology. In order to verify the performance of a system built at the University of Warmia and Mazury, an experiment was conducted. In this experiment a precise Javad GNSS receiver, commercial grade GPS/IMU XW – ADU5660 and own-built system were used. The experiment was conducted to compare the results obtained from self built device with the working military integrated navigation unit. During the study all three devices were mounted inside moving vehicle. The car drove route inside the Kortowo campus, during which, all equipment performed measurements. Then, the results from both integrated systems were compared with RTK (Real Time Kinematic) results from Javad receiver. Experiments prove that the performance of own device is comparable to the commercial device.

Correspondence: Dariusz Tomaszewski, Instytut Geodezji, Uniwersytet Warmińsko-Mazurski, ul. Oczapowakiego 1, 10-719 Olsztyn, phone: +48 89 523 42 04, e-mail: dariusz.tomaszewski@uwm.edu.pl

Introduction

Positioning and navigation systems are continuously gaining attention in location-based services (LBS) and are becoming a standard feature in modern mobile devices. The development of Micro Electro Mechanical Devices (MEMS) allow to build more and more effective, cheap devices for integrated navigation. Rapid development of various MEMS sensors allows to build smaller and more accurate devices (TANAKA 2007). In the field of navigation the following MEMS sensors are commonly used: gyroscopes, accelerometers, magnetometers, pressure sensors. Integration of these sensors allows to create the Inertial Measurement Unit (IMU). After implementation of navigational algorithms, an IMU module becomes an Inertial Navigation System (INS).

An IMU usually consists of three accelerometers and three gyroscopes. They are mounted on an orthogonal triad. The basic operating principle of inertial navigation is based on Newton's law of motion. It says that an object continues to be in a state of rest or uniform motion, unless acted upon by an external force. The application of any external force generates the acceleration, which is sensed by accelerometers. This acceleration, when integrated twice, provides the change in the state of the object with the respect to the initial conditions. Thus, an INS provides the position and attitude of the object, in the reference to the initial condition (position, velocity and attitude) of the platform (EL-SHEIMY 2004, GODHA, CANNON 2005).

In recent years, attention has focused on the development of sensors that are embedded in the same chip (e.g. accelerometers that detect acceleration in three axes simultaneously). It is achieved using MEMS, Nanoelectromechanical systems (NEMS), and Micro-Opto-Electro-Mechanical Systems (MOEMS) (HOPKINS et al. 2010, BROWN, LU 2004).

Every MEMS-INS is burdened with errors causing degradation of accuracy in time. The main error sources are: incorrect initial alignment of the navigation system, accelerometers and gyroscopes random walk and bias instability, imperfection of the gravity model, imperfect temperature compensation, non-orthogonality and misalignment of the INS sensors (SCHMIDT 2010). Microelectromechanical inertial sensors have proved to be very favorable for new applications, that have gained immediate place on the market. The main advantages of such systems are: small size, extreme ruggedness, low cost and weight. Progressive development of MEMS technology has led to manufacture of the sensors that can be used for precise applications (gyroscopes 0.2°/h, accelerometers 1 mg) (SHIN, EL-SHEIMY 2004).

The use of MEMS micro-systems for navigational applications has the potential to change completely the design and development of future car guidance and control systems (SALYCHEV et al. 2000). Additionally, modern

GNSS/RTK (Real Time Kinematic) techniques allow positioning in the range of a couple of centimetres. For this reason, attempts to put them to practical use for controlling vehicle motion for driver assistance have been made in recent years. The combination of high-accuracy positioning information obtained from GNSS/RTK with high-precision INS sensors can also support the latest concepts in vehicle-control systems, such as: detection of relative vehicle position on a highway or collision avoidance (URADZINSKI et al. 2008).

In recent years a number of INS/GPS system swereconstructed (ZHAO 2011, CHE et al. 2012, NOURELDIN et al. 2009). They were equipped with sensors of a different class and price. As a part of the research, staff of the Institute of Geodesy, built an integrated navigation system consisting of low – cost MEMS parts. Created platform was built with a possibility to implement different integration algorithms. The main idea was to create a navigation system with the cheapest possible components, allowing to perform measurements of suitable accuracy. It this study the INS/GPS integration was performed using loosely coupled integration schemes. The main goal of this paper is to compare the performance of a commercial and an own-built INS/GPS system.

Experiment description

In order to investigate the performance of the own-build GPS/IMU system, a comparative study of the results from two devices was performed.

The own-built MEMS IMU contains of a ADIS MEMS IMU and an uBlox LEA. The commercial IMU is a Chinese XW-ADU5660 (double frequency GPS, GLONASS/IMU) INS Attitude and Azimuth Integrated Navigation System from StarNeto Technology. Dual-frequency Javad Alpha GNSS receiver was used to create a reference trajectory. Both systems were evaluated in different operating environments, specifically in open and semi-urban areas.

The ADU5660 is a Chinese IMU unit with integrated GPS receiver. The producer claims the following accuracy parameters: heading with GPS enabled (0.1°), attitude (0.1°), horizontal position accuracy (2 m), vertical position accuracy (4 m), gyro bias stability (5°/h), accelerometer bias (0.1 mg). The device is depicted in Figure 1.

The ADIS three-axis inertial sensor is a high quality measurement module, consisting of an three-axis accelerometer and three-axis gyroscope. The selected measurement unit has the ability to perform measurements at 1 Hz – 350 Hz sampling rate with 14 bit resolution. The accelerometer mounted inside the IMU module allow to perform readings with a dynamic range from ± 1.7 g. The sensitivity of these device is 0.4625 mg/LSB (Least Significant Byte). Error of accelerometer measurements is characterized by 0.135 m/s/h

Fig. 1. XW-ADU5660 Attitude and Azimuth Integrated Navigation System from StarNeto Technology

velocity random walk coefficient. These values allow to determine the initial attitude of the device with accuracy of 0.02°. Gyroscope installed within ADIS measures angular rate with dynamic ranges from ±75°/s to ±300°/s with smallest possible sensitivity of 0.01832°/s/LSB. Calculated mean gyroscope's angular random walk is 5.69°/h, and the bias stability equals 0.012°/s. These technical conditions allow to achieve high accuracy during subsequent calculations. The ADIS is presented in Figure 2.

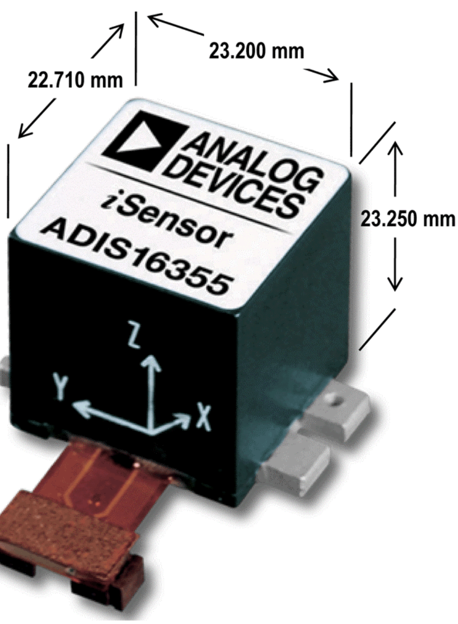

Fig. 2. ADIS MEMS IMU sensor

The own-built device scheme is presented in Figure 3. The main part of this device is ATmega micro-controller which acts as the interface between user and measurement devices. The communication between uBlox LEA GPS receiver and the micro-controller uses UBX protocol. In order to ensure time synchronization between GPS receiver and IMU readings, the receiver provides triggering impulse for ADIS at the 1 Hz frequency. Communication between ADIS and micro-controller is based on serial peripheral interface (SPI). In this experiment measurement results were recorded on a PC. Data transfer was performed using UART RS232 over USB at 230400 baud rate.

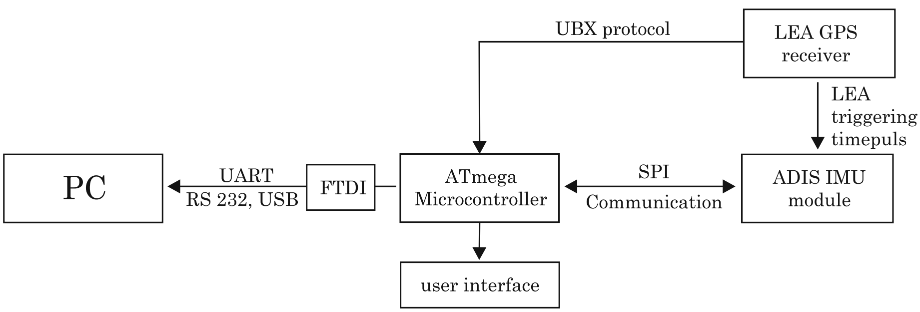

Fig. 3. Scheme of own-built IMU device

The experiment was conducted at the campus of the University of Warmia and Mazury in Olsztyn, Poland. All the equipment was fixed inside the car, with the GNSS antenna mounted on the roof. Both integrated receivers were performing measurements at 50 Hz frequency. This frequency was chosen because it is the only value on which the Chinese receiver operates. The results from 1 Hz GNSS differential, kinematic, post-processed data were used as a reference. The mean error of position obtained from GNSS processing calculated by the Topcon Tools software was 0.03 m. Therefore this trajectory can be considered as a reference for further tests. Figure 4 depicts the trajectory of the car equipped with the GNSS/IMU units.

Reference Javad receiver was connected to the same antenna with both GNSS/IMU units using antenna splitter. The reference trajectory was obtained using double frequency GNSS phase and code measurements kinematic post-processing (KROL reference station). Figure 5 depicts the equipment setup during experiment.

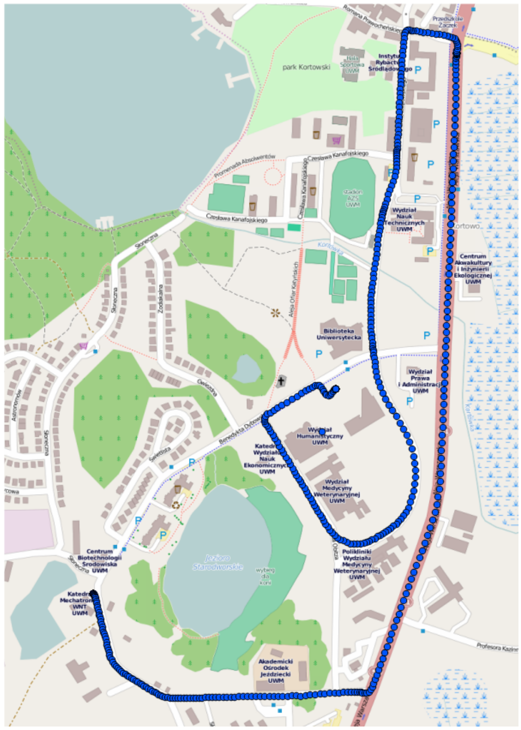

Fig. 4. Trajectory of the car equipped with the GNSS/IMU units

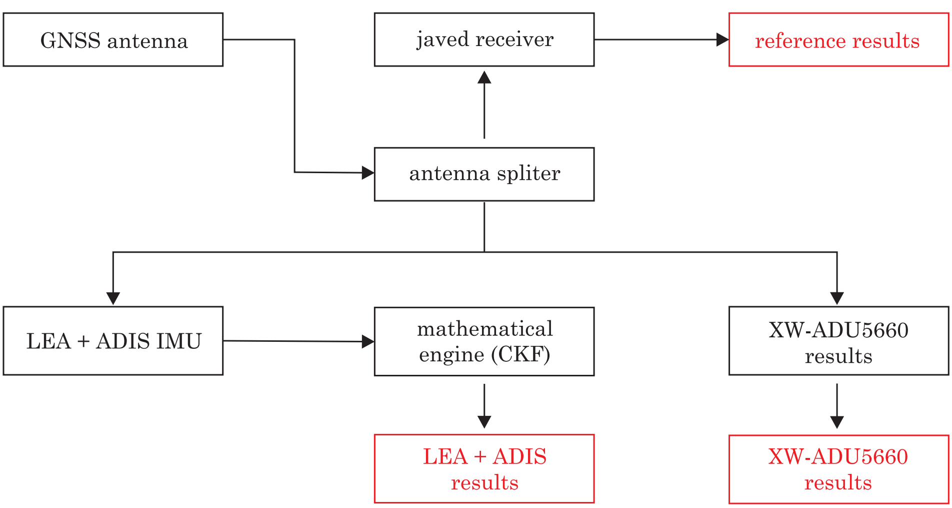

Fig. 5. Equipment setup during experiment

Data processing and results

After collecting data the results were post-processed. In this step the navigation solutions from the GPS and INS are integrated to obtain a positioning solution. Loosely coupled integration strategy was implemented using a closed loop approach. An augmented state Kalman filter was adapted for integration of the INS with GPS for effective sensor error compensation. The specific advantage of such a filter is that the inertial sensor raw measurements are corrected for deterministic errors (which vary with each power-on of the system) more efficiently (HIDE, MOORE 2005, KNIGHT 1999).

In the presented algorithm the state vector has the following form:

$$X = [\varphi_E, \varphi_N, \varphi_U, \delta v_E, \delta v_N, \delta v_U, \delta L, \delta\lambda, \delta h, \xi_x, \xi_y, \xi_z, \nabla_x, \nabla_y, \nabla_z],$$

where:

φ – East, North and Up platform misalignment angles,
δv – East, North and Up velocity errors,
δL, $\delta\lambda$, δh – latitude, longitude, and height errors,
ξ, ∇ – the gyro random drifts and accelerometer random biases respectively.

Measurements were processed with the use of few filtration algorithms. From obtained sets of results the one that was closest to the reference was chosen and presented in the study. The best solution was to use the cubature Kalman filter algorithm (CKF). The CKF provides a systematic solution for high-dimensional nonlinear filtering problems. The CKF is a spherical-radial cubature rule, which makes it possible to compute in numerical way multivariate moment integrals encountered in the nonlinear Bayesian filter. The principle of CKF filtering is presented in the literature (IENKARAN, HAYKIN 2009). Non linear errors dumping method used in the self – built platform was described as in literature (SUN, TANG 2012). The principle of data processing is depicted in Figure 6.

For the purpose of the analysis the differences of results between integrated and reference coordinates were calculated. Computations were made for each Time Of Week (TOW) seconds. Results of the conducted experiment are presented in Figures 7 and 8 and Tables 1 and 2. Figure 7 depicts coordinate differences between XW-ADU5660 IMU device and Javad GNSS receiver postprocessed data. Table 1 presents the summary of the results for XW-ADU5660 Attitude and Azimuth Integrated Navigation system.

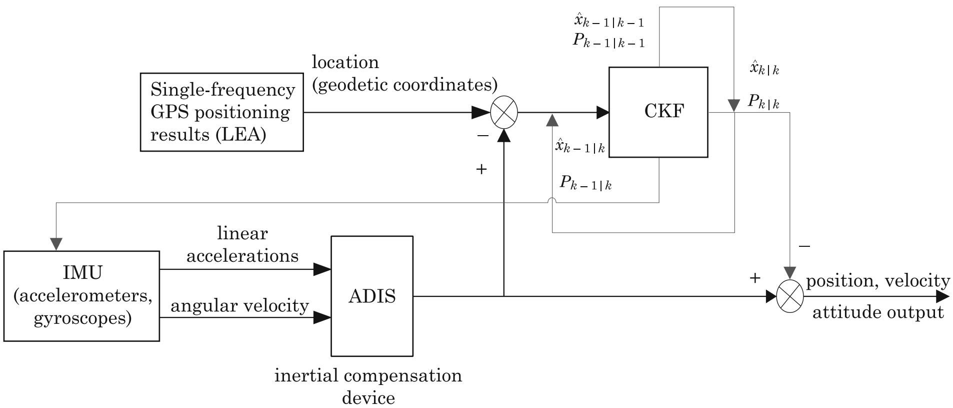

Fig. 6. Block diagram of Global Positioning System/Inertial Navigation combined Solution

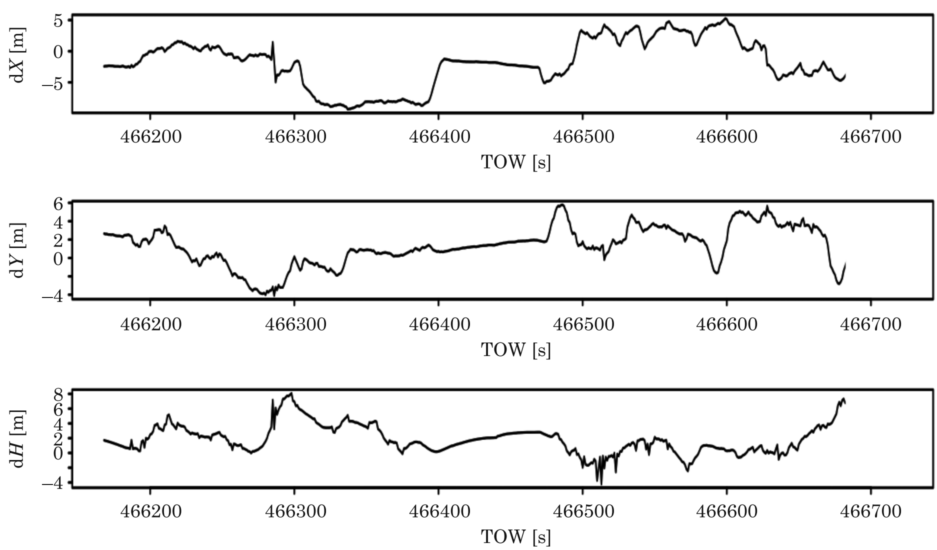

Fig. 7. Coordinate differences between XW-ADU5660 IMU device and Javad GNSS receiver postprocessed data

Figure 8 depicts coordinate differences between ADIS MEMS IMU unit and Javad GNSS receiver postprocessed data. Table 2 presents the summary of the results for ADIS MEMS IMU + uBlox LEA unit.

On the basis of conducted study one can see that the own-built system has slightly worse performance compared to the commercial device. Mean values of X, Y and Z coordinates are similar. For XW-ADU receive they are -3.20, 1.99 and 2.27 for X, Y and Z axis respectively. On the other hand the same values

Table 1

Summary of the results for XW-ADU5660

Specification	dX [m]	dY [m]	dH [m]
Minimum	0.01	0.01	0.01
1st Quartile	1.37	0.91	0.78
Median	-2.49	1.75	1.86
Mean	-3.20	1.99	2.27
3rd Quartile	4.02	2.99	3.41
Maximum	-9.32	5.79	8.07
Standard deviation	3.68	2.03	2.03
Variance	13.58	4.12	4.14

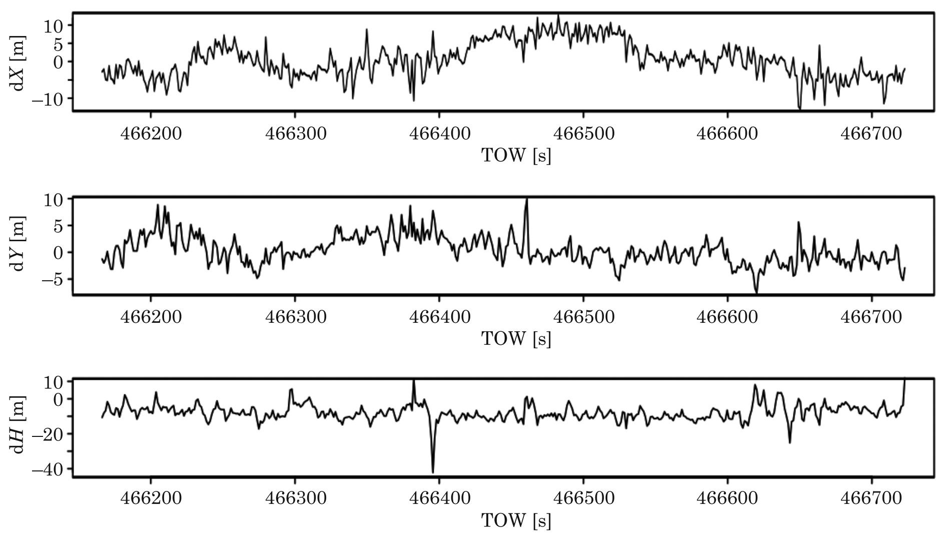

Fig. 8. Coordinate differences between LEA unit and Javad GNSS receiver postprocessed data

Table 2

Summary of the results for ADIS MEMS IMU + uBlox LEA unit

Specification	dX [m]	dY [m]	dH [m]
Minimum	0.01	0.01	0.01
1st Quartile	1.39	0.90	2.56
Median	3.33	1.60	-4.85
Mean	3.86	2.09	-5.09
3rd Quartile	5.78	2.96	6.99
Maximum	12.99	10.43	-38.43
Standard deviation	4.83	2.59	4.58
Variance	23.31	6.72	21.04

for self – build platform are 3.86, 2.09 and -5.09. On the basis of these values it can be concluded that mean accuracy of 2D coordinates obtained from both units is similar. However, value of height obtained from LEA + ADIS system is twice worst. This may be related with the quality of satellite observations made by the LEA receiver. Since it is only a GPS receiver operating on a L1 frequency. Contrasted with ADU GPS, GLONASS dual – frequency receiver, which have better H determination accuracy due to observations made on two carrier frequencies. This phenomenon is not so evident in two-dimensional positioning. Both equipment data was recorded using NMEA protocol. For GPS-only self-built integrated system, the average visible satellites were 7 and PDOP was below 3. For GPS/Glonass XW-ADU5660 navigation system, the average number of satellites was 12 and PDOP was below 1.7

Greater differences in the results can be seen in the analysis of variance and standard deviation for both systems. Obtained variance of results is much bigger for own-built system and maximum residuals are larger than for the XW-ADU5660 INS. This phenomenon can be seen with the naked eye in Figure 8 and Figure 9. Data received from ADIS IMU unit has more noise (bigger variance of residuals) while the results of XW-ADU5660 unit measurements seem to be more smoothed. It can be caused by some initial processing of data performed inside of the XW-ADU5660, while data from own-built systems were not pre-processed at all. The authors can't state what kind of filtering was used in case of commercial device because it is a closed system design.

For the raw GNSS results obtained from both devices there is no significant difference. Only Values of determined height differences are grater, what has been described previously The performance of both receivers is typical for satellite navigation (standard deviation about 3 meters).

Discussion and Summary

One test with XW-ADU5660 INS and ADIS MEMS IMU + uBlox LEA units was conducted to check the performance of the own-designed navigation platform. Results from self-built platform were processed using the same algorithm (CKF). The own-designed system is in the development stage and its open architecture gives more possibilities for further research.

From the car navigation point of view the accuracy obtained from own-built system is satisfactory. The existence of IMU data can improve the reliability of the solution. Navigation can be continued in the case of short time GNSS signal outages without losing accuracy. Some further research such as implementation of receiver autonomous integrity monitor will be performed in the near future.

References

BROWN A., LU Y. 2004. *Performance Test Results of an Integrated GPS/MEMS Inertial Navigation Package*. Proceedings of ION GPS, 21–24 September, Long Beach CA, p. 825–832, U.S. Institute of Navigation, Fairfax VA.

CHE H., LIU P., ZHANG F., WANG Q. 2012. *A Deeply Coupled GPS/INS Integrated Navigation System Suitable for High Dynamic Environments*. J. Sun et al., sud. China Satellite Navigation Conference (CSNC) 2012 Proceedings., Berlin, Heidelberg: Springer Berlin Heidelberg. DOI: 10.1007/978-3-642-29187-6_60.

EL-SHEIMY N. 2004. *Inertial techniques and INS/DGPS Integration*. ENGO 623 – Course Notes, Department of Geomatics Engineering, University of Calgary, Canada.

GODHA S., Cannon M.E. 2005. *Integration of DGPS with a MEMS-Based Inertial Measurement Unit (IMU) for Land Vehicle Navigation Application*. Proceedings of ION GPS, 13–16 September, Long Beach CA, pp. 333–345, U.S. Institute of Navigation, Fairfax VA.

HIDE C.D., MOORE T. 2005. *GPS and Low Cost INS Integration for Positioning in the Urban Environment*. Proceedings of ION GPS, 13–16 September, Long Beach CA, pp. 1007–1015, U.S. Institute of Navigation, Fairfax VA.

HOPKINS R.E., BARBOUR N.M., GUSTAFSON D.E., SHERMAN P. 2010. *Miniature Inertial and Augmentation Sensors for Integrated Inertial/GPS Based Navigation Applications*. NATO RTO Lecture Series, RTO-EN-SET-116, Low-Cost Navigation Sensors and Integration Technology.

IENKARAN A., HAYKIN S. 2009. *Cubature Kalman Filters*. IEEE Trans. Automat. Contr., 54(6): 1254–1269.

KNIGHT D.T. 1999. *Rapid Development of Tightly Coupled GPS/INS Systems*. Aerospace and Electronic Systems Magazine, 12(2): 14–18.

NOURELDIN A., KARAMAT T.B., EBERTS M.D., EL-SHAFIE A. 2009. *Performance enhancement of MEMS--based INS/GPS integration for low-cost navigation applications*. IEEE Transactions on Vehicular Technology, 58(3): 1077–1096.

SALYCHEV O., VORONOV V.V., CANNON M.E., NAYAK R.A., LACHAPELLE G. 2000. *Low Cost INS/GPS Integration: Concepts and Testing*. Proceedings of ION NTM, 26–28 January, Anaheim CA, pp. 98–105, U. S. Institute of Navigation, Fairfax VA.

SCHMIDT G. 2010. *INS/GPS Technology Trends*. NATO RTO Lecture Series. RTO-EN-SET-116. Low-Cost Navigation Sensors and Integration Technology.

SHIN E., EL-SHEIMY N. 2004. *An Unscented Kalman Filter for In-Motion Alignment of Low Cost IMUs*. Proceedings of Position Location and Navigation Symposium IEEE, 26–29 April, pp. 273–279.

SUN F., TANG L.-J. 2012. *INS/GPS integrated navigation filter algorithm based on cubature Kalman filter*. Control and Decision, 27(7): 1032–1036.

TANAKA M. 2007. *An industrial and applied review of new MEMS devices features*. Microelectron. Eng., 84(5–8): 1341–1344.

URADZINSKI M., KIM D., LANGLEY R.B. 2008. *The Usefulness of Internet-based (NTrip) RTK for Navigation and Intelligent Transportation*. Proceedings of ION GNSS 2008, 16-19 September, Savannah, pp. 1437–1445, U. S. Institute of Navigation, Fairfax VA.

ZHAO Y. 2011. *GPS/IMU integrated system for land vehicle navigation based on MEMS*.

Technical Sciences, 2017, 20(4), 333–342

Quarterly peer-reviewed scientific journal
ISSN 1505-4675
e-ISSN 2083-4527
TECHNICAL SCIENCES
Homepage: www.uwm.edu.pl/techsci/

THE EFFECT OF INFLUENCE OF CONSERVATIVE AND TANGENTIAL AXIAL FORCES ON TRANSVERSE VIBRATIONS OF TAPERED VERTICAL COLUMNS

***Jerzy Jaroszewicz*[1], *Leszek Radziszewski*[2], *Łukasz Dragun*[1]**

[1] Faculty of Management
Bialystok University of Technology, Poland
[2] Department of Mechatronics and Machine Design
Kielce University of Technology, Poland

Received 15 December 2016, accepted 10 July 2017, available online 16 August 2017.

K e y w o r d s: transverse vibrations, vertical cantilever, boundary value problem.

A b s t r a c t

The Cauchy function and characteristic series were applied to solve the boundary value problem of free transverse vibrations of vertically mounted, elastically supported tapered cantilever columns. The columns can be subjected to universal axial point loads which considerate – conservative and follower /tangential/ forces, and to distributed loads along the cantilever length. The general form of characteristic equation was obtained taking into account the shape of tapered cantilever for attached and elastically secured. Bernstein-Kieropian double and higher estimators of natural frequency and critical loads were calculated based on the first few coefficients of the characteristic series. Good agreement was obtained between the calculated natural frequency and the exact values available in the literature.

Introduction

Vertical building structures such as towers, chimneys and masts can be modelled using cantilever columns of variable cross sections, loaded at the free end with point-applied forces or along the axis with variable distributed loads. Cantilevers can be elastically supported to the base. Solutions to the boundary

Correspondence: Jerzy Jaroszewicz, Katedra Zarządzania Produkcją, Wydział Inżynierii Zarządzania, Politechnika Białostocka, ul. Ojca Tarasiuka 2, 16-001 Kleosin, e-mail: j.jaroszewicz@pb.edu.pl

value problem of critical loads and free transverse vibrations of a non-prismatic slender rod under the Euler buckling load have been reported in the literature (SZMIDLA, KLUBA 2011).

In paper (KUKLA, SKALMIERSKI 1993), the authors investigated an effect of axial loading on transverse vibrations of the Euler-Bernoulli beam of constant parameters. In JAROSZEWICZ, ZORYJ (2000), authors showed how easy it is to pass from the vibration boundary problem to critical load calculation in terms of divergence and flutter. The authors proposed an original solution to transverse vibration of the cantilever beam under the linearly variable load from dead load, which agreed with Euler's exact solution. In their analyses, the authors used the characteristic series method and introduced formulas for subsequent series coefficients using the influence function or the Cauchy function. To calculate basic natural frequency and critical forces, they used Bernstein-Kieropian double estimators, which helped find functional relationships between these values and the mass-elastic properties of the cantilever (JAROSZEWICZ, ZORYJ 1996). The influence function method in the analysis of the bending curve and relations of elastic supports of the beam with variable parameters was presented in JAROSZEWICZ et al. (2014). Such problems cannot be solved exactly for general function of variable cross section but in special cases, only when the equation is reduced to Euler's equation, special Bessel functions can be used to find the solution (ZORYJ 1982). The approach proposed by the author of this paper to apply the characteristic series method to the analysis of multi-parameter continuous systems seems warranted (JAROSZEWICZ, ZORYJ 1985, 1994. The literature reports analyses of this issue carried out using numerical and analytical methods including the MES, transfer matrix method and approximate methods based on energy principle such as those of Rayleigh-Ritz, Galerkin--Bubnow and Treffz (SOLECKI, SZYMKIEWICZ 1964).

Figure 1 shows three types of well known elastic rods loaded by non-conservative follower forces (BIDERMAN 1972). Figure 1*a* features a cantilever elastic column subjected to a follower torque M, whose vector follows the direction along the tangent to the deformed shaft axis. In Figure 1*b*, the cantilever rod has a rigidly fixed disc. Force P, maintaining the vertical orientation, does not connect to the material points of the disc but slides on its surface. Figure 1*c* shows the cantilever rod forced to the deformed axis of the rod. In all these cases, forces are external. To realize them, external follower devices should be used, such as aerodynamic propellers, pneumatic nozzles or similar systems as external energy sources. These problems are named after the researchers that were first to investigate them, Nikolai's problem, Reut's problem and the Beck's problem, respectively.

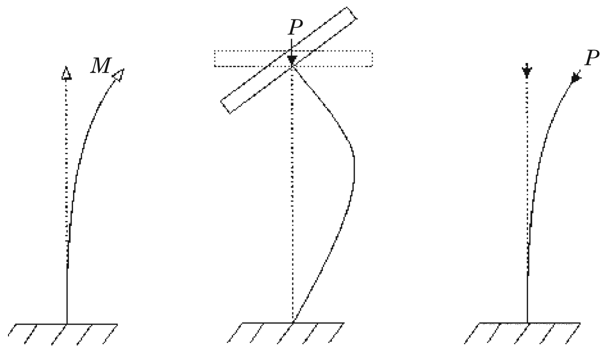

Fig. 1. Cantilever models under non-conservative forces
Source: BIDERMAN (1972).

In BIDERMAN (1972) the boundary problem of vibrations and critical loads is solved for vertical cantilevers elastically supported to the cone-shaped base.

The influence function and the partial discretization method were proposed in JAROSZEWICZ (1999) to solve the boundary value problem of free transverse vibrations of a non-homogeneous cantilever with a concentrated mass attached to its free end. In HAŠČUK, ZORYJ (1999), the authors showed that the influence function method can be effectively used to solve boundary value problems for one-parameter elastic systems with variable distribution of parameters. Universal form of a characteristic equation for a vertical cantilever, which does not

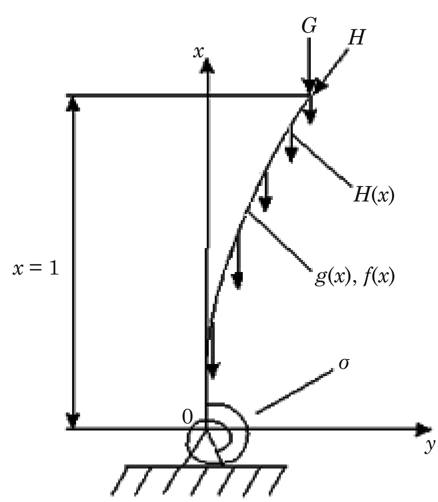

Fig. 2. The model of variable cross section column elastically secured bar with point loads: conservative G and tangential H and with distributed variable load $N(x)$

depend on the cantilever shape or the kind of axial load. The shape of the cantilever and the kind of axial load (JAROSZEWICZ, ZORYJ 1997) were taken into consideration in the form of the influence function. Form of influence function suitable to arbitrary change of a cantilever cross-section and distributed axial load were received.

In this paper, the effect of axial loads on the transverse vibrations of cantilevers with constant and variable cross sections is investigated. The cantilever model under investigation is shown in Figure 2. The following notation is used in Figure 2: $f(x)$, $g(x)$, $N(x)$ are the functions describing the distribution of the flexural rigidity, mass and axial load along the cantilever axis, G and H are the conservative and tangential forces acting at the free end of the cantilever, x and y are Cartesian coordinates, l is the length of the cantilever.

The study involved detailed investigations of vertical tapered cantilevers with geometry characterized by taper ratio γ and load parameter η which take into account conservative force G and tangential force H.

Solving the boundary problem of vibrations of a cone under conservative force *G* and tangential force *H*

The boundary problem reads

$$(f(x)y'')'' + py'' - \Omega^2 g(x)y = 0 \qquad 0 < \sigma < 1 \tag{1}$$

For the homogeneous or uniform cone, suitable mass-elastic parameters could be incorporated in these formulas

$$f(x) = (1 - \gamma x)^4, \quad g(x) = (1 - \gamma x)^2, \quad \gamma = \frac{1}{h_1}, \quad \Omega^2 = \alpha\omega^2, \quad p = \frac{l^2}{f_0}(G + H),$$

$$m_0 = g(x)\,|_x = 0$$

where

h – is length of cone which is parts of sharp cone which length is l,

$J(x)$ – moment of inertia cross section.

E is Young's modulus, I_0 denotes the moment of inertia of the cross section at the fixed end, m_0 is the unit mass corresponding to the cross section at the fixed end, p and ω are the load and frequency parameters, η is the parameter of non-conservatively, and γ is the taper ratio for conical cantilevers and σ is rigidity coefficient of elastic supports.

$$\alpha = \frac{m_0 l^4}{f_0} \qquad \eta = \frac{H}{G + H} \tag{2}$$

The boundary condition for $\gamma(x) \equiv 0$ is as follows

$$y(0) = 0, \quad y'(0) + \sigma''(0) = 0, \quad f(x)y''(x)|_{x=l} = 0, \quad ((f(x)y''(x))' + Gy'(x))|_{x=l} = 0 \tag{3}$$

The boundary conditions in the case when attached cantilever $\sigma = 0$ and with consideration for $N(x)$ can be written as

$$y(0) = y'(0) = 0, \quad f(x)y''(x)|_{x=1} = 0 \text{ and } G \equiv 0 \tag{4}$$

$$(f(x)y''(x)') - N(x)y'(x)|_{x=1} = 0 \tag{5}$$

As in ZORYJ (1982), the general solution has the form

$$y(x,\alpha) = K(x,\alpha) + \dot{K}(x,\alpha) + \ddot{K}(x,\alpha) + \dddot{K}(x,\alpha) \tag{6}$$

where:
$K(x,\alpha)$ – Cauchy's function derivatives with respect to $\dot{K}(x,\alpha) + \ddot{K}(x,\alpha) + \dddot{K}(x,\alpha)$.

Substituting expression (6) into conditions (3–4) yields the system of equations with respect to unknown constants C_0, C_1, C_2 and C_3. Equating the determinant of the above equation to zero, we obtain the characteristic equation.

$$\begin{gathered}\nabla \equiv f(x)[K'(x,\alpha)K'''(x,\alpha) - K'''(x,\alpha)K''(x,\alpha] + \\ +pN(x)[K'(x,\alpha)K''(x,\alpha) - K''(x,\alpha)K'(x,\alpha)] = 0|_{\substack{x=1\\ \alpha=0}}\end{gathered} \tag{7}$$

It is common practice in engineering neglect some loads, namely, $N(x) \equiv 0$ and $G = H - 0$. In this case, characteristic equation (6 and 7) becomes as

$$\nabla \equiv [K''(x,\alpha)\dot{K}'''(x,\alpha) - K'''(x,\alpha)\dot{K}''(x,\alpha)] - K''(x,\alpha)\dot{K}(x,\alpha)]| = 0|_{x=1} \tag{8}$$

The above equations are a direct consequence of the definition of Cauchy's function (JAROSZEWICZ, ZORYJ 1997, 2014). Equation (8) is a universal characteristic equation, taking into account all considered cases of longitudinal load and any change in transverse cross section of the bracket. As will be shown in the following paragraphs, the basic problem of solving the equation (8) is to determine the appropriate form of Cauchy's influence function for the case in question.

The Cauchy function with respect to the four variables corresponding to the bracket of any continuous load ($N(x)$) has the following form JAROSZEWICZ, ZORYJ (1997):

$$K(x,\alpha,p,\mu) = f(\alpha)\sum_{i=0}^{\infty}\mu^i I_i(x,\alpha,p) \tag{9}$$

where:

$$I_i(x\alpha,p,\mu) = \int_{\alpha}^{x} g(t)I_0(x,t,p)I_{i=1}(x,\alpha,p)\mathrm{d}t,$$

$$I_0(x,\alpha,p) = \sum_{k=0}^{\infty}(-p)^k V_k(x,\alpha),$$

$$V_k(x,\alpha) = -\int_{\alpha}^{x} N(t)V_0(x,t)W'_{k-1}(t,\alpha)\mathrm{d}t,$$

$$V_0(x,\alpha) = \int_{\alpha}^{x}\frac{(x-s)(s-\alpha)}{f(s)}\,\mathrm{d}s.$$

The form of the influence function (9) ensures that the characteristic equations will be power series with respect to the parameter with the coefficients A_k dependent on the load parameter p:

$$\sum_{k=0}^{\infty} A_k(l,0)\mu^k = 0 \tag{10}$$

Cantilever loaded conservative and tracking forces

The coefficients of the characteristic series (10) in this case ($N(x)$ 0, $M = 0$) can be determined using the formulas (JAROSZEWICZ, ZORYJ 1997):

$$A_k(x,\alpha) = \sum V_{i,k-i}(x,\alpha) \text{ '4 } p(1-\eta)W_{i,k-i}(x,\alpha) \tag{11}$$

where

$$V_{i,j}(x,\alpha) = (J_i'' J_j''' - J_i''' J_j'')f^2(\alpha)f(x) \tag{12}$$

$$W_{i,j}(x,\alpha) = (J_i J_j'' - J_i'' J_j')f^2(\alpha) \tag{13}$$

The first three coefficients of the series defined by (11) are:

$$A_0(x,\alpha) = V_{00} - p(1-\eta)W_{00} \tag{14}$$

$$A_1(x,\alpha) = V_{01} + V_{10} - p(1-\eta)(W_{01} + W_{10}) \tag{15}$$

$$A_2(x,\alpha) = V_{02} + V_{11} + V_{20} - p(1-\eta)(W_{02} + W_{11} + W_{20}) \tag{16}$$

Considering the truncated cone support, for which stiffness and mass functions have been given the following form of function $J_i(x,\ \alpha)$ i $U(x,\ \alpha)$ (JAROSZEWICZ, ZORYJ 1997):

$$J_0(x,\alpha) = \int_{\alpha}^{x} \frac{(x-t)U(t,\alpha)}{f(t)}\mathrm{d}t \tag{17}$$

$$J_i(x,\alpha) = \int_{\alpha}^{x} g(t)J_0(x,t)J_{i-1}(t,\alpha)\mathrm{d}t \tag{18}$$

$$U(x,\alpha) = \frac{1}{\varphi(x,\alpha)}\sin[\varphi(x,\alpha)(x-\alpha)] \tag{19}$$

$$\varphi(x,\alpha) = \frac{\sqrt{p}}{(1-\gamma x)(1-\gamma\alpha)} \tag{20}$$

with the help of which factors were built (14), (15), (16).

The equating zero to the first coefficient of series (10), we obtain the equation, whose element with respect to the variable p gives the critical load in Euler's sense for the bracket:

$$\eta + (1 - \eta)(1 - \gamma)\left[\cos\frac{\sqrt{p}}{1-\gamma} + \frac{\gamma}{\sqrt{p}}\sin\frac{\sqrt{p}}{1-\gamma}\right] = 0 \tag{21}$$

Example of calculation double estimators of base frequency: lower ω_-^2 and higher ω_+^2 and critical loads

The case of the fixing rigidity $\delta = 0$ and non-conservative load with force $H(G = 0)$ is considered as first. Table 1 summarizes the natural frequencies of the rod depending on the compression force H. Table 2 summarizes the calculated results for the frequencies of the cantilever with the clamping elasticity $\delta \neq 0$ taken into account.

Table 1

Results of calculation natural frequency estimators for the attached cantilever $\delta = 0$

$\gamma = 0$			$\gamma = 0.2$			$\gamma = 0.5$			$\gamma = 0.7$		
p	ω_-^2	ω_+^2	p	ω_-^2	ω_+^2	p	ω_-^2	ω_+^2	p	ω_-^2	ω_+^2
0	12.36	12.36	0	14.81	14.82	1	26.54	26.66	1	43.98	44.60
1	13.25	13.26	1	16.44	16.46	2	33.24	33.50	2	71.27	74.79
5	17.77	17.79	5	25.46	25.55	3	42.06	42.68	3	104.83	119.60
10	26.70	26.81	10	48.81	50.04	4	53.94	55.53	3.1	108.56	125.60
15	43.32	44.10	11	57.05	59.50	5	70.35	75.18	3.2	112.54	132.80
19.5	78.01	96.40	12	67.72	73.38	6	94.36	126.80	–	–	–
19.6	79.32	101.98	13	82.20	104.20	–	–	–	–	–	–

Source: HAŠČUK, ZORYJ (1999).

Table 2

Calculation results from natural frequency estimators for the elastically secured cantilever $0<\delta<20$

$\gamma = 0$			$\gamma = 0.2$			$\gamma = 0.6$			$\gamma = 0.8$		
σ	ω_-^2	ω_+^2	σ	ω_-^2	ω_+^2	σ	ω_-^2	ω_+^2	σ	ω_-^2	ω_+^2
1	2.726	2.727	1	3.262	3.263	1	7.016	7.023	1	11.804	11.843
5	0.664	0.665	5	0.786	0.787	5	1.776	1.777	5	3.037	3.039
10	0.342	0.343	10	0.404	0.405	10	0.917	0.918	10	1.573	1.574
15	0.229	0.230	15	0.271	0.272	15	0.618	0.619	15	1.061	1.062
20	0.173	0.174	20	0.204	0.205	20	0.466	0.467	20	0.800	0.801

Source: HAŠČUK, ZORYJ (1999).

In the Figure 8 shows the results of the critical load calculation for the truncated cone obtained from equation (21) (JAROSZEWICZ, ZORYJ 1997).

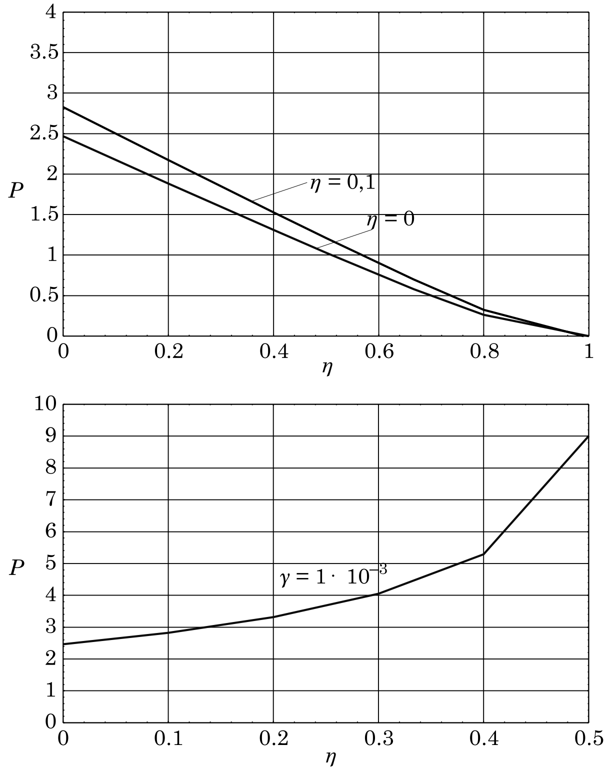

Fig. 3. Euler critical force for a cantilever cone under conservative and follower forces

Conclusion

In the paper shows that the influence function method can be an effective tool for solving the boundary problem of single- and two-parameter elastic systems with variable distribution of parameters. The universal characteristic equation (8), (10) for the vertical tapered cantilevers, which does not depend on the beam shape and axial load type, has been recorded. The shape and type of load is taken into account in the form of an influence function (9) that corresponds to any change in cross-section of the support and continuous axial load with the condition that functions describing stiffness, and the continuous load was total.

In detail, a conical shaped cone with a convergence coefficient was considered γ, γ, which is laden with the conservative force G, the tracking force H. The share of forces G and H is determined by the coefficient of conservatism η. In this case, the integral expressions for the first three members of the characteristic series (14), (15), (16) are derived. The general form of the kth member of the series (11) was also recorded.

Vertical tapered cantilevers with geometry characterized by coefficient γ and subjected to conservative force G and tangential force H defined by load parameter η were investigated in detail.

The method employing characteristic series and equal-tail estimators used in this paper allows obtaining functional relationships for natural frequency estimators and critical loads of flutter and divergence types, which in turn facilitates optimization of mass elastic parameters of the system for the reduction of dynamic loads – the loss of stability and for preventing resonance. This method can be of use in engineering calculations.

References

BIDERMAN V.L. 1972. *Prikladnaja teorija mechaničeskich kolebanij*. Vyssaja Škola, Moskva.

HAŠČUK P., ZORYJ L.M. 1999. *Linijni modeli diskretno-neperervnyh mechanicznych system*. Lviv, Ukrainski technologii, 372.

JAROSZEWICZ J. 1999. *The effect of non-homogenous material properties on transverse vibration of elastic cantilever*. JAM, Kiev, 35(6): 103–110.

JAROSZEWICZ J., ZORYJ L. 1985. *Free transversal vibrations of a cantilever beam with variable cross section*. Eng. Trans., 33(4): 537–547.

JAROSZEWICZ J., ZORYJ L. 1994. *Transversal vibrations and stability of beams with variable parameters*. Int. Appl. Mech.-Eng. Tr., 30(9): 713–720.

JAROSZEWICZ J., ZORYJ L. 1996. *Critical Euler load for a cantilever tapered beam.* J. Theor. Appl. Mech., 4(34): 843–851.

JAROSZEWICZ J., ZORYJ L.M. 1997. *Metody analizy drgań i stateczności kontynualno-dyskretnych układów mechanicznych*. Politechnika Białostocka, Białystok.

JAROSZEWICZ J., ZORYJ L. 2000. *Investigation of axial loads on transverse vibrations of vertical cantilevers of variable parameters*. JAM, Kiev, 36(9): 1242–1251.

JAROSZEWICZ J., ŻUR K., DRAGUN Ł. 2014. *The influence function method in analysis of bending curve and relations of elastic supports of beam with variable parameters*. Journal of Theoretical and Applied Mechanics, 52(1): 247–255.

KUKLA S., SKALMIERSKI B. 1993. *The effect of Axial Load on Transverse Vibrations of an Euler Bernoulli Beam*. J. Theor. and Appl. Mech., 2(31).

SOLECKI R., SZYMKIEWICZ J. 1964. *Układy prętowe i powierzchniowe, obliczenia dynamiczne*. Arkady, Warszawa.

SZMIDLA J., KLUBA M. 2011. *Stateczność i drgania swobodne niepryzmatycznego układu smukłego poddanego obciążeniu eulerowskiemu*. Modelowanie Inżynierskie, 41: 385–394.

ZORYJ L.M. 1982. *Universal characteristic equations in problems on the vibrations and stability of elastic systems*. Tverd. Tela, 6: 155–162.

Technical Sciences, 2017, 20(4), 343–358

Quarterly peer-reviewed scientific journal
ISSN 1505-4675
e-ISSN 2083-4527
TECHNICAL SCIENCES
Homepage: www.uwm.edu.pl/techsci/

A CFD MODEL OF A TWO-PHASE MIXTURE FLOW IN A TEST STAND FOR AIR-BORNE PARTICLE ANALYSIS

***Marta Stachnik*[1], *Gabriel Czachor*[2], *Marek Jakubowski*[1]**

[1] Department of Food Industry Processes and Facilities
Faculty of Mechanical Engineering
Koszalin University of Technology
[2] Institute of Agricultural Engineering
Wrocław University of Environmental and Life Sciences

Received 12 February 2017, accepted 2 August 2017, available online 16 August 2017.

Key words: CFD model, Euler method, two-phase flow, aerosol, air-borne particles.

Abstract

Farmers come across many materials which when being handled generate dust clouds. Even with low concentration these might pose risk of explosion and can carry dangerous microorganisms. To broaden the knowledge about fine dust particles sedimentation and analyze process of particles becoming air-borne, a tunnel air cleaner was designed. Based on the experiment, a CFX simulation was performed using the Eulerian approach and the CFX12.1 software. Presented model is a stedy state two-phase analysis of dust sedimentation. The results show mechanism of dust dispertion over large distance, such as regions of vorticity that seem to be main motor. Presented analysis emphasizes how easily small particles can become resuspended in the air and carried over distance. Acquired knowledge can be applied for safety regulation in many branches of agriculture.

Nomenclature

C_d – mass density of dispersed phase, kg m^{-3}
d_d – average diameter of particles, μm
D_{md} – diffusion coefficient of dispersed phase in a fluid, m s^{-2}
d_u – unit velocity, m s^{-1}
d_y – unit distance between fluid layers, m
$\mathbf{F}$ – additional volumetric forces, N kg^{-1}
f_d – coefficient of flow resistance for dispersed phase, –
g – gravitational acceleration, m s^{-2}
L – distance in the tunnel, m

Correspondence: Marta Stachnik, Katedra Procesów i Urządzeń Przemysłu Spożywczego, Wydział Mechaniczny, Politechnika Koszalińska, ul. Racławicka 15-17, 75-620 Koszalin, e-mail: marta.stachnik@tu.koszalin.pl

p – pressure, Pa
$\mathbf{u}$ – velocity, m s^{-1}
$\mathbf{u}_{slide}$ – velocity in-between phases, m s^{-1}
μ – dynamic viscosity, Pa·s
μ_T – turbulent viscosity, Pa·s
ν – kinematic viscosity, m^2 s^{-1}
ρ – density, kg m^{-3}
ρ_c – density of solid phase, kg m^{-3}
ρ_d – density of dispersed phase, kg m^{-3}
τ – shear stress, N m^{-2}
φ_c – volumetric share of continuous phase, –
φ_d – volumetric share of dispersed phase, –

Introduction

Handling solid material produces clouds of dust. Dust particles are not only a threat to health, but also pose a fire and explosion hazard. An airborne powder of a combustible material has properties similar to a flammable gas mixed with air, and so it can cause an explosion in a closed space. Furthermore, pressure waves from the initial explosion can throw deposited dust into the air in front of the advancing flame, all of which may result in a "secondary" explosion, extending far beyond the original dust cloud (*Hazard Prevention and Control...* 1999). Air cleaning equipment has to be installed everywhere where dust clouds are generated. Selection of a dust control system is based on the desired air quality. The dust control system is required to prevent or minimize the risk of an explosion or fire, and to reduce employee exposure to dust. Moreover, these installations deal with unpleasant odors, improve visibility and lower the probability of an accident (FLAGAAND, SEINFELD 1988, *Hazard Prevention and Control...* 1999).

Farmers deal with many types of biomass that generates dust – fertilizers, forage, wheat, straw or wood chips. Pellets have become very popular for household use, all sorts of straw, wood chips or biomass mix can be used as raw materials. Still, the most common one is straw, because it is usually collected instead of being mixed with the soil. Then it can be used for burning in boilers, either in the form of bales or pellets (OBERNBERGER, THEK 2010, DÖRING 2013).

Computer simulations have become a very useful tool. More and more processes are analyzed using CFD (Computational Fluid Dynamics) simulations. CFD is a proven simulation tool, and it is applicable to almost any field of study. It can be applied to various agricultural issues, such as external atmospheric processes as well as modeling in land and water management, predicting forest fires, air pollution and dust dispersion (LEE et al. 2013).

Although there have been numerous attempts at modeling the sedimentation process, there are still some unresolved issues. DORRELL and HOGG (2010) mathematically modeled sedimentation of bidisperse suspensions in quiescent fluid. Sedimentation process of non-cohesive solid particles in a two-dimensional channel was also modeled by XU and MICHAELIDES (2003). They analyzed particle behavior in a horizontal channel. The simulations showed that the process of sedimentation comprises three stages. During the first stage, the initial particle configuration has key influence on the average velocity of particles and they might form a *V*-shape or *W*-shape front. In the second stage concentration of particles is lower, but strong interactions occur among them. The process highly depends on the formation and destruction of particle clusters. The sedimentation velocity depends on the number of clusters formed and developed velocity field. During the third stage, the concentration becomes low and the particle clusters become stable (XU, MICHAELIDES 2003).

This paper is focused on creating a CFD model of a horizontal tunnel (Fig. 1) using CFX software package. This tunnel will be used to analyze sedimentation of dust to improve modern air cleaning systems. Moreover, the tunnel will be used to analyze the process in which fine particles become airborne, since the majority of research in the field of agriculture focuses on larger ones, such as grains and seeds and not on the fine particles or dust.

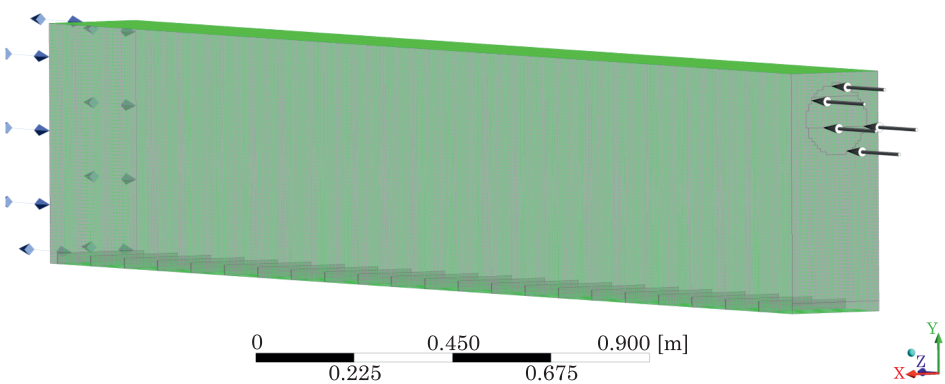

Fig. 1. The geometry of the simulated tunnel and applied mesh

Material and methods

The object of the simulation is a box-shaped tunnel (Fig. 2). Specifications needed for creating three-dimensional model, the computational simulation and validation of the results were obtained in association with The Wrocław University of Environmental and Life Sciences.

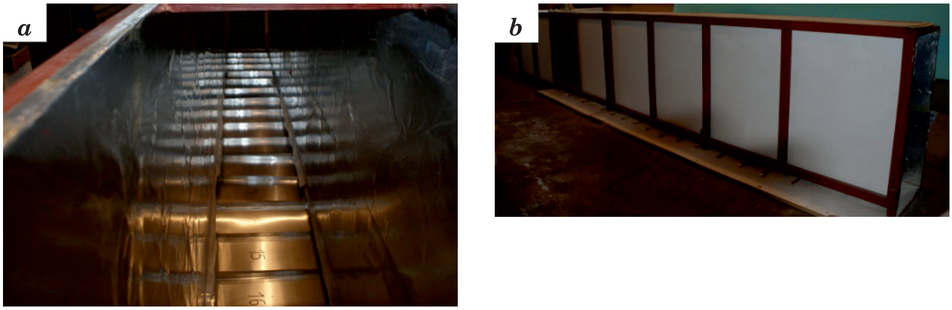

Fig. 2. The experimental tunnel: *a* – view of the sections at the bottom, *b* – general view

Experiment setup

The experiment was performed in a full scale tunnel of the same dimensions as the one used for simulation (Fig. 2). In Figure 3 sections at the bottom are shown. The air was polluted with dust generated during straw pellet production. Analysis of the dust particles' geometry showed that only 10% had their shape close to spherical – for instance index of sphericity higher than 0.9 (CZACHOR et al. 2014). Mastersizer 2000 (Malvern Instruments, UK) was used for measuring particle size of the dust. These measurements were later used to set properties of the simulated dust. Its working principle is based on laser

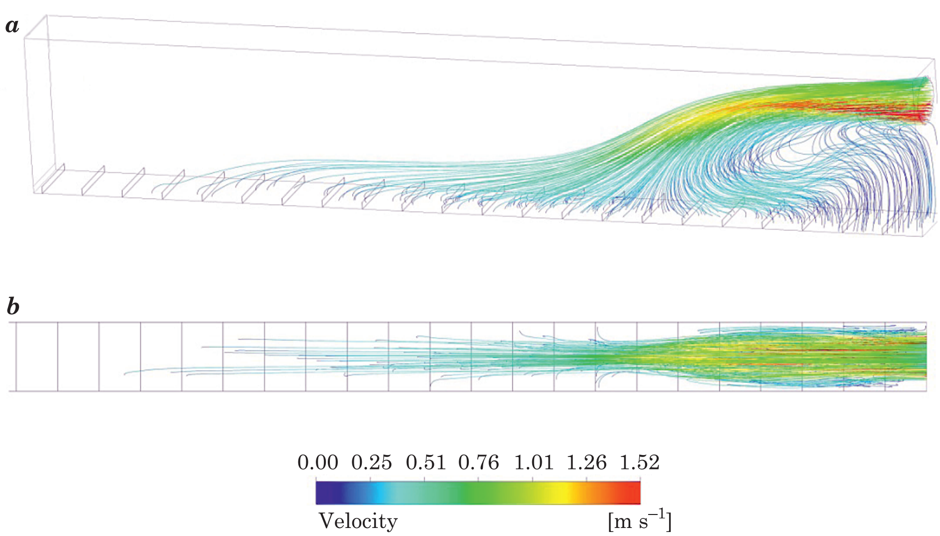

Fig. 3. Particle velocity on particle trace visualization for 300 pcs: *a* – side view, *b* – top view

diffraction. When particles pass through a focused laser beam they scatter light at an angle that is inversely proportional to their size. This angular intensity of the scattered light is measured by a series of photosensitive detectors, providing the final result.

Mathematical model

Based on an Eulerain description of the phases, a two-phase model is presented. The considered flow is steady. The equation of continuity for the flow is formulated by applying the principle of mass conservation to a small volume of fluid. The standard form of this equation for Cartesian coordinates goes as follows (ABBOTT, BASCO 1989):

$$\nabla \cdot (\rho \mathbf{u}) = 0 \tag{1}$$

The velocity distribution of a dispersed phase is represented by the following equation (ABBOTT, BASC 1989, pp. 5–30):

$$\nabla \cdot \varphi_d \left[\mathbf{u} + \varphi_d (1 - c_d) \mathbf{u}_{\text{slide}} - \frac{D_{md}}{\varphi_d} \nabla \varphi_d \right] = - \frac{m_{dc}}{\rho_d} \tag{2}$$

Equation of momentum takes the form of (ABBOTT, BASCO 1989, JAKUBOWSKI et al. 2014):

$$\begin{gathered} \rho \mathbf{u} \cdot \nabla \mathbf{u} = - \nabla [- p + (\mu + \mu_T)(\nabla \mathbf{u} + (\nabla \mathbf{u})^T)] - \\ - \nabla \cdot \{[\rho c_d (1 - c_d)[\mathbf{u}_{\text{slide}} \mathbf{u}_{\text{slide}}\} + \rho \boldsymbol{g} + \mathbf{F} \end{gathered} \tag{3}$$

where

$$\rho = \varphi_c + \varphi_d \rho_d \tag{4}$$

and

$$c_d = \frac{\varphi_d \rho_d}{\rho} \tag{5}$$

A fluid-fluid drag function is modeled using the Schiller-Neumann model, which is specified with the following equation:

$$\frac{3 f_d}{4 d_d \cdot 10^{-6}} \rho_c \left| \mathbf{u}_{\text{slide}} \right| \mathbf{u}_{\text{slide}} = \frac{\rho - \rho_d}{\rho} \nabla_p \tag{6}$$

Schiller-Neumann model is the one available for modeling fluid-particle interaction. This is valid model widely used and giving suitable results. It is used for particles that are sufficiently small and considered spherical. Moreover, this model is suitable for sparsely distributed particles.

The correct limiting behavior in the inertial regimes is ensured by limitation of Reynolds number as follows:

$$f_d = \begin{cases} \frac{24}{\mathrm{Re}_p} (1 + 0.15\ \mathrm{Re}_p^{0.687}) \text{ for } & \mathrm{Re}_p<1000 \\ & Re_p>1000 \end{cases} \tag{7}$$

where Reynolds number is defined as:

$$\mathrm{Re}_p = \frac{d_d \cdot 10^{-6} \rho_c \left|\mathbf{u}_{\mathrm{slide}}\right|}{\mu} \tag{8}$$

For turbulence a standard κ–ε model was used (ZIKANOV 2010, JAKUBOWSKI et al. 2014). It was chosen as it is useful and accurate for free-shear layer flow with relatively small pressure gradient and wall-bounded and internal flow. This model includes two extra transport equations to represent the turbulent properties of the flow. This allows a two equation model to account for history effects like convection and diffusion of turbulent energy. The turbulence kinetic energy (k) is specified with the following equation:

$$\rho \frac{\partial k}{\partial t} + \rho \mathbf{u} \cdot \nabla k = \nabla \cdot [\mu + \sigma_k \mu_T \nabla] + P_k - \rho \beta \mathrm{k} \omega \tag{9}$$

For dissipation the model transport equation can be written as:

$$\rho \frac{\partial \varepsilon}{\partial t} + \rho \mathbf{u} \cdot \nabla \varepsilon = \nabla \cdot \left[\left(\mu + \frac{\mu_T}{\sigma_\varepsilon}\right) \nabla \varepsilon\right] + C_{\varepsilon 1} \frac{\varepsilon}{k} P_k - \rho C_{\varepsilon 2} \frac{\varepsilon^2}{k} \tag{10}$$

Where P_k represents the rate of shear production of k and is given in expanded form as follows:

$$P_k = \mu_T \left(\left[\frac{\partial \mathbf{u}}{\partial y} + \frac{\partial v}{\partial x}\right)^2 + \left(\frac{\partial v}{\partial z} + \frac{\partial \mathbf{w}}{\partial y}\right)^2 + \left(\frac{\partial \mathbf{u}}{\partial z} + \frac{\partial \mathbf{w}}{\partial x}\right)^2\right] + \mu_T \left[2\left(\frac{\partial \mathbf{u}}{\partial x}\right)^2 + 2\left(\frac{\partial v}{\partial y}\right)^2 + 2\left(\frac{\partial \mathbf{w}}{\partial z}\right)^2 \tag{11}$$

and eddy viscosity is modeled as:

$$\mu_T = C_\mu \frac{k^2}{\varepsilon} \tag{12}$$

Computational model assumptions

Studied flow was steady and subsonic. The flow was assumed to be incompressible as there was no pressure change and temperature changes were neglected. Moreover its physicochemical properties were constant. The process was isothermal and there was no occurrence of chemical reactions and such conditions were applied for experimental study. There was no transfer of mass and momentum at the interface of air and dust. Pressure changes were intentionally omitted as those would not have any influence on the process. Based on observation the turbulence was considered as low (1%). Particles were fully coupled to the continuous fluid. Fully coupled particles exchange momentum with the continuous phase, enabling the continuous flow to affect the particles, and the particles to affect the continuous flow. Full coupling is needed to predict the effect of the particles on the continuous phase flow. The drag force was taken into account, it was based on Schiller-Neumann model. As dust particle is simulated to be of a simple shape and it is immersed in a Newtonian fluid – air, which is not rotating relative to the surrounding free stream, the drag coefficient depends only on the particle Reynolds number. The studied process was sedimentation and so the gravitational effect and buoyancy were considered.

In multiphase flow the difference in density between phases produces a buoyancy force. Analyzed flow contained a continuous phase and a dilute dispersed phase, so the value of the buoyancy reference density was set of the continuous phase. This is because the pressure gradient is nearly hydrostatic, so the reference density of the continuous phase cancels out buoyancy and pressure gradients in the momentum equation.

The domain's boundary conditions were set to: reference pressure – 1 atm; gravity – 9.81 m s^{-2} and buoyant reference density was set as 1 kg m^{-3}. The wall boundary conditions were set to no-slip wall option and smooth wall. The fluid layer at the wall had velocity equal to that on the wall. For steady state this velocity was zero:

$$\mathbf{u} = 0 \tag{13}$$

CFD distinguishes between two Coefficients of Restitution specifying particle behavior after collision: parallel coefficient of restitution – was set as 0; and perpendicular coefficient of restitution was set as 0.5, thus particles collision was semi-elastic. The parallel and perpendicular restitution coefficients describe the action of particles when they hit a wall. Dust particles did not stick to the wall nor did they bounce off immediately.

As for initial conditions for air, temperature at the inlet was set to 25°C. In the experiment air velocity was non-uniform. Boundary "Inlet" in the CFD model was divided in three sections, where measured values were applied. For top section: velocity was set at 0.60 m s^{-1}, mass flow rate of $2 \cdot 10^{-5}$ kg s^{-1}. Middle section: velocity was 0.9 m s^{-1}, mass flow rate of $3 \cdot 10^{-5}$ kg s^{-1}. Bottom section: velocity was 1.5 m s^{-1}, mass flow rate of 10^{-4} kg s^{-1}. Particle diameter distribution was based on normal distribution and the flow was uniform.

Relative pressure for opening was set to 0 Pa, what means that at the exit pressure was 1 atm.

Convergence was achieved when the RMS (Root Mean Square) of the normalized residual error reached the value of 10^{-4} for all the equations. This required 1820 loop iterations.

CFD Model

The overall dimensions of the device were: width 0.3 m, depth 4 m, and height 0.7 m (Fig. 1). The center of a round inlet was situated at the height of 0.6 m, and its diameter was 0.14 m. The cleaner was graduated in each dimension with marks for each: 0.3 m along the width (across the bottom of the box), 0.03 m along the height, and 0.18 m along the length.

Properties of the simulated dust were set to: min. diameter 28 μm, max. diameter 64 μm, mean diameter 44 μm, S_d 13 μm and density of 700 kg m^{-3}. Mean distribution of particles' diameters was based on Gaussian distribution. The geometry of the flow domain was created in Cartesian coordinates (X, Y, Z). The length of the tunnel followed the Z axis, width – the X axis, and height – the Y axis. Mesh was created with the meshing tool available as part of ANSYS, and it had 931,023 nodes and 88,420 elements. A structured grid was chosen, so that cells would be hexahedral and would not skew. The domain was divided into the hexahedral mesh. The domain consisted of three boundaries: inlet, outlet and wall. The inlet was divided into three regions. This classification was the result of non-uniform distribution of particles and their velocity at the entrance.

Results and discussion

In turbulent flow there are two well understood mechanisms that influence the mean settling rate. The firsts is due to the non-linear dependence of the drag on the relative velocity at finite Reynolds numbers. The settling velocity decreases with increasing turbulence intensity. The second mechanism is more complex and is due to the preferential trajectories of freely falling particles. Particles do not sample the turbulent flow infirmly, but prefer regions of downwash rather than regions of the up-moving fluid. Particle movement is also influenced by the velocity of the fluid, friction between particle and air and force of gravity.

Particles entered the inlet with the air stream and followed its trajectory. The particle velocity profile is shown in Figure 3 and the velocity profile of the mixture is presented in Figure 4. Dust entered the cleaner at 1.5 m s^{-1} at the bottom of the inlet, 0.9 m s^{-1} in the middle and 0.6 m s^{-1}at the top section of the inlet. Due to gravitational force and air friction, particles lost their velocity and settled at the bottom of the box. Streamline indicated two regions of turbulence (Fig. 5). The swirl that appeared over the stream had no influence on the particles' trajectory. Velocity in this region had average value of 0.27 m s^{-1}. Under the stream at the distance of 1 m a turbulent flow occurred, that carried particles backward. The average velocity of that air whirl was 0.46 m s^{-1}, ranging from 0.53 to 0.36 m s^{-1}. The carried particles lost their velocity to average 0.04 m s^{-1} and settled within the first five sections. Illustration in Figure 3*b* shows that particles formed a *U*-shaped front. This was caused by the horizontal motion of the stream, as opposed to vertical motion which causes formation of a *V*- or *W*-shape front. Three stages mentioned in the introduction and studied by XU and MICHAELIDES (2003) can be partially observed in analyzed flow. Particles initially create uniform flow and it is consistent with initial configuration, meaning that air velocity has strongest affect on particle behavior and here the *U*-shaped front can be observed. The shape resembling more letter *U* than *V* is caused by the horizontality of the flow. Vertical flow creates sharper edges as gravity adds to the flows shape, in analyzed flow gravity worked against it. At the second stage gravity has stronger influence than air, particle clusters become less dense, but no strong interactions occur among them. During the third stage the concentration becomes the lowest. The sedimentation velocity depends rather on strength of the influence of the gravity rather than on the number of clusters formed. Even though there is discrepancy between horizontal and vertical flows particles behave similarly. Heavier particles went off the stream's course immediately, and lighter ones created a rounded front. Dust that entered through the top section of the inlet had an average velocity of 0.6 m s^{-1}, but it was carried by the lower faster stream and those particles accelerated up to between 0.83 and 0.91 m s^{-1} (average) and then slowly descended. Due to friction between the air stream and the edges of inlet, velocity was much lower – average 0.62 m s^{-1}.

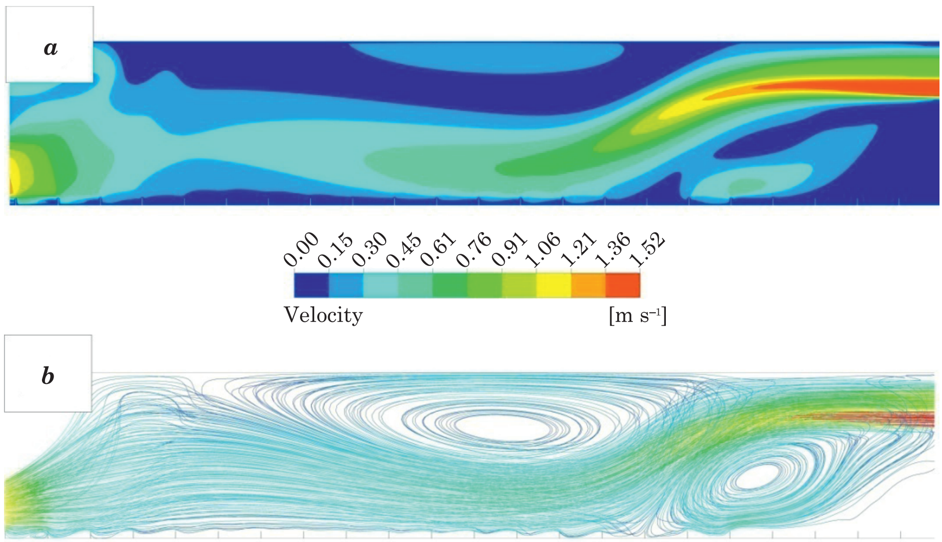

Fig. 4. Velocity in the tunnel: *a* – velocity profile in *ZY* plane for *X* = 0.15 m, *b* – velocity vector plot on a streamline

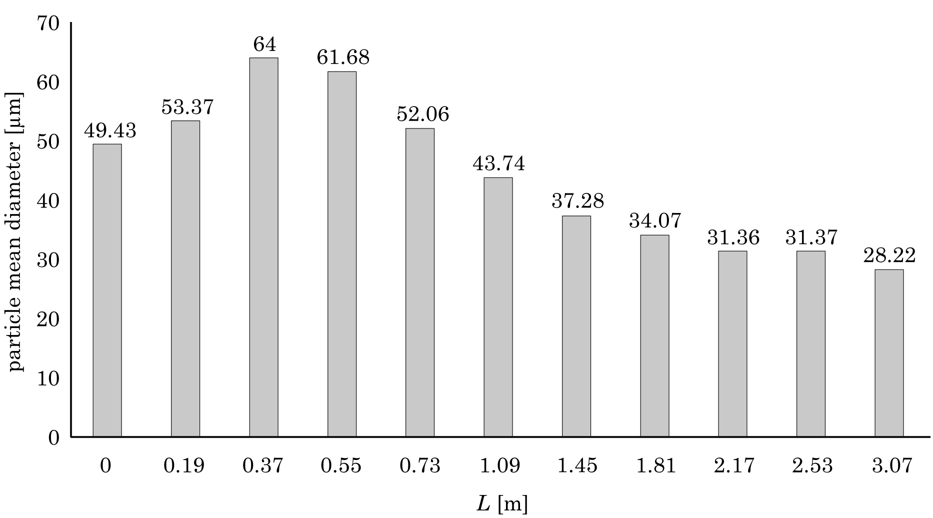

Fig. 5. Experimental mean particle diameter distribution along the tunnel, *L* – length of the tunnel

The first attempt at model verification was done by comparing the velocity distribution. Three planes were placed at specific distances from the inlet – the same ones at which measurements in the tunnel were conducted. Experimental results are listed in the Table 1 and results from computational model are concluded in the Table 2.

Table 1

Velocities measured in the experimental tunnel

Distance from inlet [m] / Height above bottom [m]	Velocity [m s^{-1}]		
	0.10	2.10	3.00
0.10	0.44	0.36	0.31
0.30	0.39	0.53	0.36
0.45	0.45	0.61	0,36
0.60	0.90	0.45	0.25

Table 2

Velocities from CFD model of the tunnel

Distance from inlet [m] / Height above bottom [m]	Velocity [m s^{-1}]		
	0.10	2.10	3.00
0.10	0.02	0.52	0.20
0.30	0.06	0.38	0.33
0.45	0.40	0.07	0.20
0.60	0.90	0.19	0.04

Close to the inlet there was a discrepancy between the calculated and measured velocity. It was due to dividing the inlet into three sections, each having a different velocity, and so air stream in the simulation achieved its uniform velocity later than in the experimental tunnel. Further away from the inlet velocity of the fluid stream was more similar to data presented in the Table 2. Such a discrepancy is a result of simplifications required to perform a computer simulation.

A chi-squared test was conducted, and it showed that there was no significant difference between velocities at 0.10 m and 2.10 m. The critical value for $\alpha = 0.05$ was $p = 0.3519$ and calculated values were $p_{0.10} = 0.01383$ and $p_{2.10} = 0.2009$ respectively. The calculated value of $p_{3.00}$ was equal to 0.7306. Apparently, there was a significant difference between the registered velocities but only at a considerable distance from the inlet.

As predicted, the smallest particles traveled the longest distance, and those of the biggest mean diameter settled at the beginning of the tunnel (Fig. 5, 6). As mentioned before, some particles accumulated within the first few sections because of air stream turbulence.

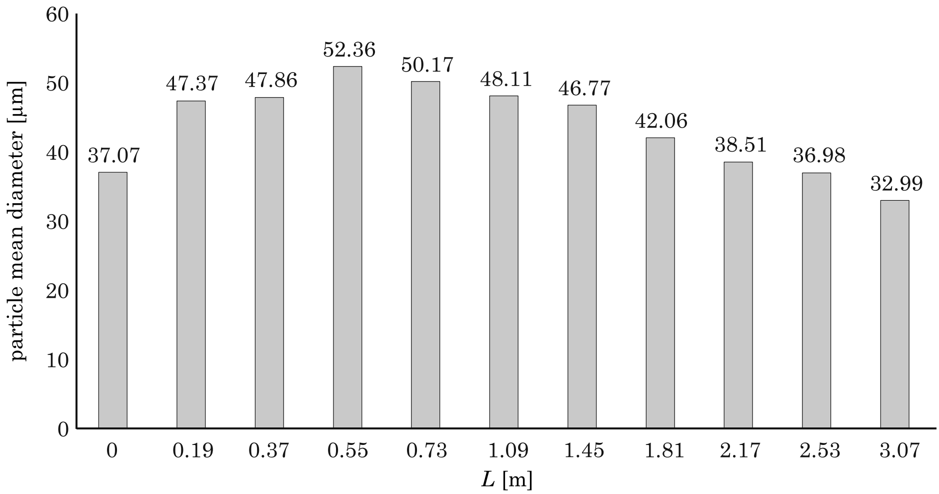

Fig. 6. Simulated particle diameter distribution throughout the tunnel, L – length of the tunnel

Statistic analysis with the use of the chi-square test showed that there was no significant difference between the two distributions. The calculated value p equaled $1.384 \cdot 10^{-6}$ and it was smaller than the critical value $p = 5.226$ for $\alpha = 0.05$. This means that both distributions are similar and CFD model if sufficiently accurate.

Both charts show that the smaller the particle was, the farther it traveled, and the lightest ones went as far as 3.6 meters. Medium-sized particles landed mainly within central segments of the tunnel, but some were carried backward, that is toward the front wall. Particles' mass correlates with their size, thus, mass and mean diameter distributions look similar. The smallest particles were the lightest ones, and they were carried the longest distances by the air stream. Lightest bits of dust had the mean diameter equal to 28.31 μm, and the heaviest particles had the mean diameter of 63.75 μm.

The heaviest particles entered through the bottom and the central parts of the inlet, where the velocity was highest, but they landed soon after. The lightest particles on the other hand came mostly from the top part of the inlet. Despite the fact that their velocity was the lowest they traveled the longest distance due to their small weight – meaning the gravitational pull was weakest, all of which suggests that those particles are the most likely to become airborne. Even the smallest bits can carry pathogenic microbes. WHO classified dust particles into 3 categories: inhalable, thoracic, and respirable fractions. The most dangerous are the respirable ones, because human body is not able to remove them from the air passages (*Hazard Prevention and Control*... 1999). Inhalable fraction consists of particles of the size smaller than 100 μm.

Upper respiratory system: nose, mouth, throat and larynx can stop and remove from the body particles bigger than 30 μm. Particles up to 20 μm reach the middle respiratory system: trachea, bronchi and bronchioles. Respirable fraction consist of particles smaller than 7 μm, those reach alveoli and can stay there up to 3 months (*Hazard Prevention and Control*... 1999). Relative mass distribution was calculated for both experimental and model tunnel and it is presented in Figures 8 and 9 and on the particle track in Figure 7. It can be seen that dust's bits in the CFD model were more evenly distributed along the bottom. Differences between experimental results and data obtained from the CFD analysis come from simplifications implemented in the computational model. Material properties were averaged and humidity of the air and moisture content of the dust were intentionally omitted.

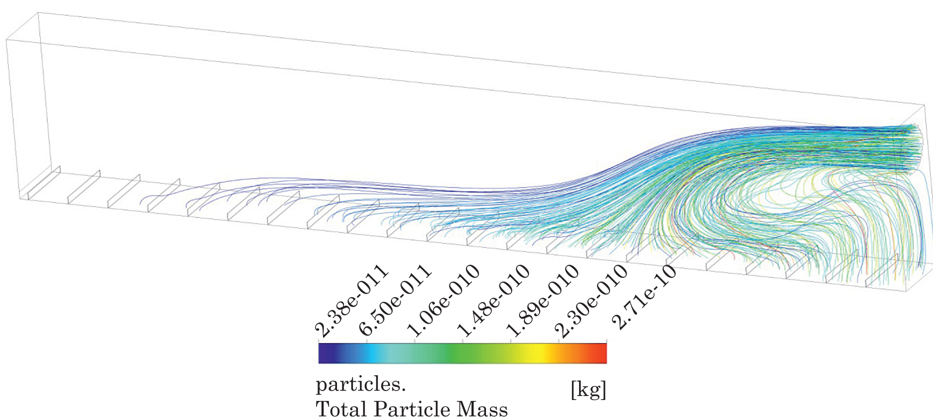

Fig. 7. Particle mass distribution throughout the tunnel

Statistic analysis with the use of the chi-square test showed that there was no significant difference between the experimental and simulated distributions. The calculated value p equaled 0.537 and was smaller than the critical value of 9.380 for α = 0.05. Meaning, both series belonged to the same population.

KOCH and HILL (2001) pointed out that particle inertia plays a very important role in the sedimentation process, in fact, it leads the particles to be thrown out of vortices and to accumulate in regions where the turbulence is lower. This is one of the mechanisms on how particle clusters are formed and sustained. It held true for the analyzed case. As shown in Figure 4*b* there was a vortex under the stream, which pulled back some of the particles to the front of the tunnel (Fig. 8). Moreover, inertia pushed the lightest particles forward.

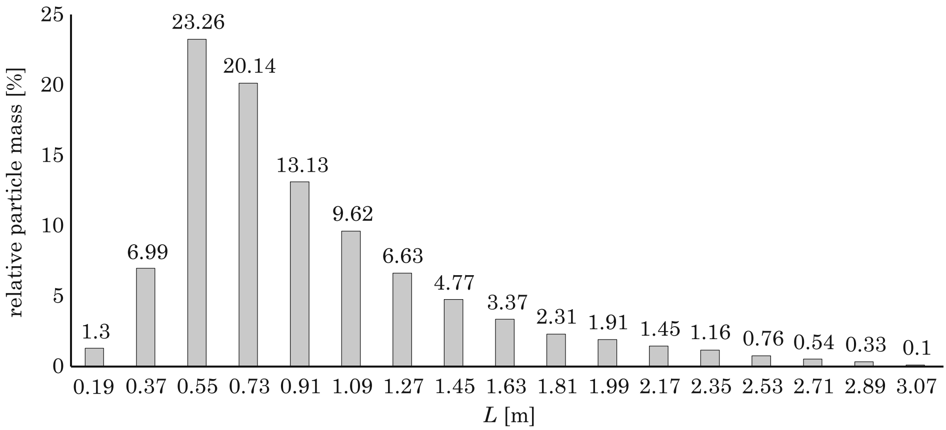

Fig. 8. Experimental relative particle mass distribution throughout the tunnel, L – length of the tunnel

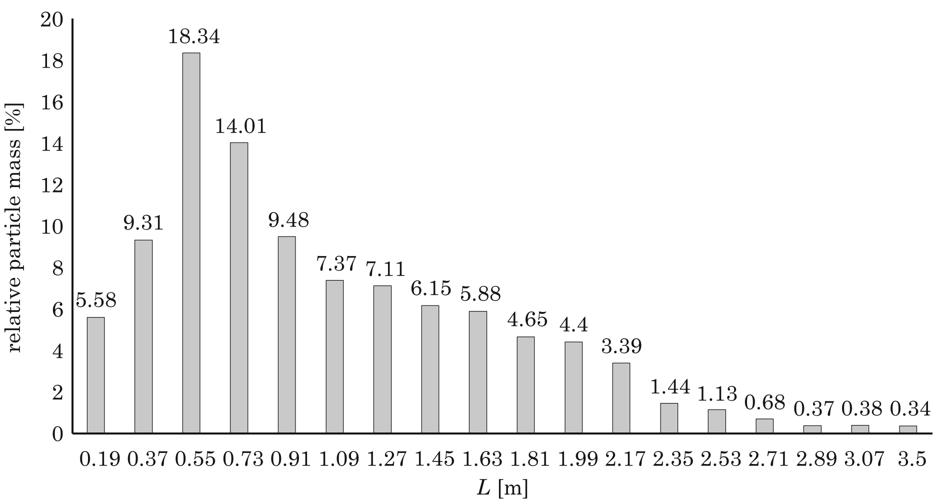

Fig. 9. Simulated relative particle mass distribution throughout the tunnel, L – length of the tunnel

The top of the air stream had lower velocity, however, because of the lower layer having higher velocity, the smallest bits traveled all the way to the exit of the tunnel.

Air streams can occur anytime during when farm materials are being handled, e.g. door opening or in a straw cutter. Moving air even at the speed of 0.6 m s^{-1} can put dust particles in motion. Dust deposits might be moved at a significant distances (here 3 m). In the tunnel air vortexes appeared, those can give insight in particle behavior in highly turbulent air stream.

Conclusions

In this paper a 3D numerical model was used to simulate the flow structure of a horizontal tunnel taking into account the momentum exchange between particles and fluid phase. The verified computational model is accurate. Results obtained via calculations show significant similarity to those from the experiment in terms of particle distribution along the bottom of the tunnel. This proves that simulation was carried out in an appropriate manner and can be used for further investigation. Three important characteristics, gravitational settling and deposition and resuspentions, of particles are included and considered carefully. The simulation results show that gravity has a noticeable influence on larger particles, but for smaller particles the influence of gravity is small and, in general, they share the common dispersion and transport properties of air. The model is extensible to consider more physical effects, such as thermal gradient, pressure changes, surface roughness, electrostatic forces and particle resuspension. As there is lack of simiral analysis presented model will be used to simulate motion and behavior of particles of different size and density found in field of agriculture.

References

ABBOTT M.B., BASCO D.R. 1997. *Computational Fluid Dynamics: An Introduction For Engineers*. Longman Group, UK Limited, p. 5–30.

CECALA A.B., O'BRIEN A.D., SCHALL J., COLINET J.F., FOX W.R., FRANTA R.J., JOY J., REED W.R., REESER P.W., ROUNDS J.R., SCHULTZ M.J. 2012. *Report of Investigations 9689 Dust Control Handbook for Industrial Minerals Mining and Processing, Centers for Disease Control and Prevention National Institute for Occupational Safety and Health Office of Mine Safety and Health Research Pittsburgh*. http://www.cdc.gov/niosh/mining/UserFiles/works/pdfs/2012-112.pdf, p. 28–42 (access: 20.10.2014).

CZACHOR G., BOHDZIEWICZ J., GRYSZKIN A. 2014. *Analysis of the size of dust particles which were formed during pellet production*. Inżynieria Rolnicza, 2(150): 7–13.

DÖRING S. 2013. *Power from Pellets Technology and Applications*. Springer, p. 13–14.

DORRELL R., HOGG A.J. 2010. *Sedimentation of bidisperse suspensions*. International Journal of Multiphase Flow, 36: 481–490.

FLAGAN R.C., SEINFELD J.H. 1988. *Fundamentals of Air Pollution Engineering*. Prentice-Hall Inc., US, http://authors.library.caltech.edu/25069/ p. 391–478 (access: 21.10.2014).

Hazard Prevention and Control in the Work Environment: Airborne Dust. Protection of the Human Environment Occupational Health and Environmental Health Series. 1999. Geneva Hazard prevention and control in the work environment: Airborne dust. http://www.who.int/occupational_health/publications/en/oehairbornedust3 (access: 20.10.2014).

JAKUBOWSKI M., STERCZYSKA M., MATYSKO R., POREDA A. 2014. *Simulation and experimental research on the flow inside a whirlpool separator*. Journal of Food Engineering, 133: 9–15.

KOCH D.L., HILL R.J. 2001. *Inertial effects in suspension and porous-media flows.* The Annual Review of Fluid Mechanics, 33: 619–647.

LEE I., BITOG J.P., SE-WOON H., IL-HWAN S., KYEONG-SEOK K., BARTZANA T., KACIRA M. 2013. *The past, present and future of CFD for agro-environmental applications*. Computers and Electronics in Agriculture, 93: 168–183.

Mastersizer 2000 Integrated systems for particle sizing, http://www.malvern.co.uk/ms2000 (access: 8.11.2015).

MODY V., JAKHETE R.M. 1987. *Dust Control Handbook For Minerals Processing*. Department of the Interior. Washington DC, U.S. https://www.osha.gov/dsg/topicss-1ilicacrystalline/dust/dust_control_handbook.html (access: 21.10.2014).

OBERNBERGER I., THEK G. 2010. *The Pellet Handbook the Production and Thermal Utilization of Pellets*. Earthscan, NY, p. 85–108.

XU Z., MICHAELIDES E. 2003. *The effect of particle interactions on the sedimentation process of non-cohesive particles*. International Journal of Multiphase Flow, 29: 959–982.

ZIKANOV O. 2010. *Essential Computational Fluid Dynamics*. Wiley & Sons, New Jersey, p. 86–102.

Technical Sciences, 2017, 20(4), 359–374

Quarterly peer-reviewed scientific journal
ISSN 1505-4675
e-ISSN 2083-4527
TECHNICAL SCIENCES
Homepage: www.uwm.edu.pl/techsci/

HEURISTIC DERIVATION OF BRINKMAN'S SEEPAGE EQUATION

Ryszard Wojnar

Institute of Fundamental Technological Research
Polish Academy of Sciences Warszawa

Received 14 February 2017, accepted 10 July 2017, avaible online 16 August 2017.

Key words: porosity, Darcy's law, Stokes' equation, successive iterations, Born's approximation.

Abstract

Brinkman's law is describing the seepage of viscous fluid through a porous medium and is more acurate than the classical Darcy's law. Namely, Brinkman's law permits to conform the flow through a porous medium to the free Stokes' flow. However, Brinkman's law, similarly as Schrödinger's equation was only devined. Fluid in its motion through a porous solid is interacting at every point with the walls of pores, but the interactions of the fluid particles inside pores are different than the interactions at the walls, and are described by Stokes' equation. Here, we arrive at Brinkman's law from Stokes' flow equation making use of successive iterations, in type of Born's approximation method, and using Darcy's law as a zero-th approximation.

Introduction

Many problems of interest, involve the motion of fluid through a porous solid, which interacts at every point with the diffusing fluid (MORSE, FESHBACH 1953). The classical equation describing the fluid seepage through a porous solid is known as Darcy's law

$$v = -\frac{K}{\eta}\nabla(p + U) \tag{1}$$

Correspondence: Ryszard Wojnar, Instytut Podstawowych Problemów Techniki, Polska Akademia Nauk, ul. Pawińskiego 5B; 02-106 Warszawa, e-mail: rwojnar@ippt.pan.pl

It expresses the fluid velocity v (understood as the filter velocity rather than as the true velocity in pores) by the gradient of the pressure p and the volume force potential U. The permeability coefficient K describes the porosity of the solid, and η denotes the viscosity of the fluid.

Equation (1) was proposed by Henry Darcy in 1855 on the basis of his experiments (cf. DARCY 1856), and can be motivated by contemporary asymptotical methods (cf. SANCHEZ-PALENCIA 1980). The equation patterned on others transport equations (Fourier's, Ohm's) does not render aptly the specificity of the fluid. A basic objection is that any viscous shear tensor can be derived from it, as the viscous shearing has been neglected. Related to this objection are difficulties in posing the boundary conditions, for example for problems in which the fluid flows concomitantly through porous medium and adjoining empty space.

In the versatile physical heritage of Henri Coenraad Brinkman involving quantum physics, physical chemistry, applied physics (cf. e.g. BRINKMAN, KRAMERS 1930, BRINKMAN 1947) one finds also his equation describing seepage of the fluid through porous medium, cf. (BRINKMAN 1949). The equation gives the following expression for the fluid velocity

$$v = \frac{K}{\eta} [- \nabla(p + U) + \eta' \, \Delta v] \tag{2}$$

Equation (2) is known as Brinkman's equation or Brinkman's seepage law. It is known also as Darcy-Brinkman's equation (cf. VALDES-PARADA et al. 2007).

In comparison with Darcy's Equation (1) the term with Δv was added at the right hand side of Equation (2). The coefficient η' (known also as the effective viscosity) is a modified fluid viscosity which may be different from η. Frequently, $\eta' \approx \eta$. Both, η and η' are assumed to be constant. Equation (2) is completed by the potential U, which was absent in the original Brinkman's paper (BRINKMAN 1949).

Experimental measurements and computer simulation results have suggested that the Darcy-Brinkman equation should incorporate an effective viscosity.

Equation (2) can be written also in the form

$$- \nabla(p + U) = \frac{\eta}{K} v - \eta' \, \Delta v$$

more convenient for a discussion. We see that for low values of K, and small spatial variations of the velocity v this equation is approximated by Darcy's

Equation (1). For high values of K Stokes' equation for a steady flow of fluid with the viscosity η' is obtained (cf. LANDAU, LIFSHITZ 1987)

$$0 = -\nabla(p + U) + \eta' \Delta v$$

Equation (2) was proposed by Brinkman without giving any proof (BRINKMAN 1949).

Indirect, experimental proofs of validity of Brinkman's equation are provided by Gordon S. Beavers and Daniel D. Joseph (BEAVERS, JOSEPH 1967) and by Geoffrey Ingram Taylor (TAYLOR 1971). The proofs are more valuable as, apparently, these authors did not know Brinkman's paper (BRINKMAN 1949).

In theoretical way Brinkman's law was obtained by Enrique Sanchez--Palencia and Thérèse Lévy, who considered the fluid flow through an array of fixed particles (SANCHEZ-PALENCIA 1983, LÉVY 1983) and applied asymptotic expansions in series. These papers deal with idealized models of porous medium, represented by an array of rarely distributed balls. However, both Darcy's and Brinkman's laws are macroscopic ones, and some macroscopic argument seems to be needed in deriving Brinkman's equation.

Francisco J. Valdes-Parada et al. gave a theoretical back-up for the existence and meaning of an effective viscosity for the Stokes flow within a porous medium (VALDES-PARADA et al. 2007).These authors have shown that the use of a slip boundary condition is required to obtain an effective viscosity different from the one corresponding to the fluid phase. The proof is done by means of an up-scaling procedure based on volume averaging methods, which provides a boundary-value problem to compute the underlying effective viscosity (VALDES-PARADA et al. 2007, WHITAKER 1999).

The scattering process of the fluid flow against the porous canals walls suggests an idea of applying Born's approximation used favorably in description of scattering in quantum mechanics (BORN 1926, also MORSE, FESHBACH 1953, SHANKAR 1994). Born's approximation constitutes a version of successive approximation method. We apply it because Brinkman's equation is formally similar to Schrödinger's equation. This approximation, applied in quantum scattering theory consists of taking the incident field in place of the total field as the driving field at each point in the scatterer. In our case, the role of driving field is realised by Darcy's flow. The term *driving field* is explained in Appendix 1. Now, starting from Stokes' flow equation and Darcy's law, we are going to obtain Brinkman's law by Born's method as a correction of Darcy's law.

Brinkman's law derived by Born's approximation

Consider Stokes' equation with potential U

$$0 = -\nabla(p + U) + \eta\,\Delta v \tag{3}$$

and assume that the flow is incompressible, it is

$$\nabla \cdot v = 0 \tag{4}$$

We apply the operator ∇ to Equation (3), and by Equation (4) we get

$$\Delta\,(p + U) = 0 \tag{5}$$

The same harmonicity property has the sum $(p + U)$ in Darcy's law (1) and in Brinkman's law (2).

It was shown by asymptotic methods that Stokes' Equation (3) subject to periodic boundary conditions for the velocity v at walls of pores in a given porous medium leads to Darcy's law (1) (cf. SANCHEZ-PALENCIA 1980, WOJNAR 2014).

Hence, as a zero-th approximation of solution of Equation (3) for the flow in porous medium we take just Darcy's law

$$v^0 = -\frac{K^0}{\eta}\nabla(p + U) \tag{6}$$

where K^0 is a constant. According to the method of Born's approximation, we look for a corrected solution in the form

$$v = v^0 + \lambda\, v^1 \tag{7}$$

where λ is a small number, or, by (6)

$$v = -\frac{K^0}{\eta}\nabla(p + U) + \lambda\, v^1 \tag{8}$$

We substitute the relation (8) into Equation (3), and using harmonicity (5) of the sum $(p + U)$ we get

$$0 = -\nabla(p + U) + \eta\,\Delta\,(\lambda\, v^1) \tag{9}$$

This equation differs from Equation (3) only by notation of the velocity vector, here we have $\lambda\ v^1$ instead of v in (3). Thus, in analogy with the expression (6) the approximated solution of Equation (9) reads

$$\lambda\ v^1 = -\frac{K^1}{\eta}\nabla(p + U) \tag{10}$$

where K^1 is a new constant, or again by Equation (3)

$$\lambda\ v^1 = -\frac{K^1}{\eta}\eta\,\nabla v \tag{11}$$

Therefore, by (8) and (11) we find

$$v = -\frac{K^0}{\eta}\nabla(p + U) - \frac{K^1}{\eta}\eta\,\Delta\, v \tag{12}$$

Now, if we substitute $K^0 \equiv K$ and $K^1 = -Kv'/v$ we get Brinkman's Equation (2). Notice, that introducing the constant K^1 is equivalent to introducing the Brinkman's effective viscosity.

Non-homogeneous porous medium

Now, we show that proposed method of derivating Brinkman's equation can be applied to the linearly non-homogeneous porous medium, it is to the case

$$K = a_0 + a_1x_1 — a_2x_2 + a_3x_3 \tag{13}$$

where:
a_0 and a_i, $i = 1,2,3$ are constants,
while x_i, $i = 1,2,3$ are the position x components.

Just for clarity, apart from the direct symbolic vector notation, we will use the indicial notation. The subscripts range from 1 to 3, and Einstein's summation convention over repeated subscripts is observed.

For a non-homogeneous porous medium Darcy's law still reads

$$v_i^0 = -\frac{K}{\eta}\frac{\partial\,(p + U)}{\partial\, x_i} \tag{14}$$

but now the permeability K depends on the position $x = (x_1, x_2, x_3) = (x_i)$ with $i = 1,2,3$,

$$K = K(x)$$

and, naturally, the viscosity η is constant, it is x – independent. Hence, Stokes' Equation (3) holds

$$-\frac{\partial(p + U)}{\partial x_i,} + \eta \frac{\partial^2 v_i}{\partial x_k \partial x_k} = 0 \tag{15}$$

After applying v – operator to both sides of the last equation, and using the incompressibility condition (4) we get, cf. Equation (5),

$$\frac{\partial^2 (p + U)}{\partial x_k \partial x_k} = 0 \tag{16}$$

On its turn, the incompressibility condition (4) expressed on (14) reads

$$\frac{\partial}{\partial x_i}\left(K \frac{\partial (p + U)}{\partial x_i}\right) = 0 \tag{17}$$

or

$$\frac{\partial K}{\partial x_i} \frac{\partial (p + U)}{\partial x_i} + K \frac{\partial^2 (p + U)}{\partial x_k \partial x_k} = 0$$

or, by (16)

$$\frac{\partial K}{\partial x_i} \frac{\partial (p + U)}{\partial x_i} = 0 \tag{18}$$

Hence, after differentiation

$$\frac{\partial K}{\partial x_i} \frac{\partial^2 (p + U)}{\partial x_k \partial x_i} = -\frac{\partial^2 K}{\partial x_k \partial x_i} \frac{\partial (p + U)}{\partial x_i} \tag{19}$$

As in the previous section, we look for a corrected Darcy's law in the form

$$v_i = -\frac{K^0}{\eta}\frac{\partial(p + U)}{\partial x_i} + \lambda\, v_i^1 \tag{20}$$

We submit the relation (20) into Stokes' Equation (3)

$$-\frac{\partial\,(p + U)}{\partial x_i} + \eta\,\frac{\partial^2}{\partial x_k\,\partial x_k}\left(-\frac{K^0}{\eta}\frac{\partial\,(p + U)}{\partial x_i} + \lambda\, v^1{}_i\right) = 0 \tag{21}$$

Now

$$\frac{\partial}{\partial x_k\,\partial x_k}\left(K^0\frac{\partial(p + U)}{\partial x_i}\right) = \frac{\partial^2 K^0}{\partial x_k\,\partial x_k}\frac{\partial(p + U)}{\partial x_i} + 2\,\frac{\partial K^0}{\partial x_k}\frac{\partial^2(p + U)}{\partial x_k\,\partial x_i} + K^0\,\frac{\partial^3(p + U)}{\partial x_k\,\partial x_k\,\partial x_i}$$

By Equation (16) the last term vanishes, and after substituting (19) we have

$$\frac{\partial^2}{\partial x_k\,\partial x_k}\left(K^0\frac{\partial\,(p + U)}{\partial x_i}\right) = \frac{\partial^2 K^0}{\partial x_k\,\partial x_k}\frac{\partial(p + U)}{\partial x_i} - 2\,\frac{\partial^2 K^0}{\partial x_k\,\partial x_i}\frac{\partial(p + U)}{\partial x_k}$$

and by the linear relation (13) this whole term vanishes. Then, Equation (21) takes form

$$-\frac{\partial\,(p + U)}{\partial x_i} + \eta\,\frac{\partial^2(\lambda\, v_i^1)}{\partial x_k\,\partial x_k} = 0 \tag{22}$$

This is Stokes' type equation with unknown function $\lambda\, v_i^1$. Similarly as in the previous section, we regard Darcy's law to be an approximate solution of this equation

$$\lambda\, v_i^1 = -\frac{K^1}{\eta}\frac{\partial(p + U)}{\partial x_i} \tag{23}$$

or by Stokes' Equation (15)

$$\lambda\, v_i^1 = -\frac{K^1}{\eta}\, \eta\, \frac{\partial^2 v_{\mathrm{i}}}{\partial x_k\, \partial x_k} \tag{24}$$

and after substitution $K^0 \equiv K$ and $K^1 = -K\, \eta'/\eta$ the corrected Darcy's Equation (20) reads

$$v_i = -\frac{K}{\eta}\left(\frac{\partial(p + U)}{\partial x_i} + \eta'\, \frac{\partial^2 v_i}{\partial x_k\, \partial x_k}\right) \tag{25}$$

This is Brinkman's equation again.

Anisotropic viscous fluid

For such a fluid Darcy's law is of the form

$$v_i = -\, \kappa_{ij}\, \frac{\partial(p + U)}{\partial x_j} \tag{26}$$

where κ_{ij} is a symmetric matrix of constant coefficients, and $x = (x_i)$, $i = 1,2,3$ denotes the position. By incompressibility (4) we get

$$\kappa_{ij}\, \frac{\partial(p + U)}{\partial x_i\, \partial x_j} = 0 \tag{27}$$

For flow of anisotropic fluid, Stokes' equation is of the form (cf. LANDAU, LIFSHITZ 1987),

$$-\frac{\partial(p + U)}{\partial x_i} + \frac{\partial}{\partial x_i}\left(\eta_{ijmn}\, \frac{\partial v_m}{\partial x_n}\right) = 0$$

where η_{ijmn} is the viscosity tensor. It satisfies the symmetry conditions

$$\eta_{ijmn} = \eta_{mnij} = \eta_{jimn} = \eta_{ijnm}$$

For constant coefficients η_{ijmn} we get the following form of Stokes' equation

$$- \frac{\partial (p + U)}{\partial x_i} + \eta_{ijmn} \frac{\partial^2 v_m}{\partial x_j \, \partial x_n} = 0 \tag{28}$$

We apply operator $\kappa_{ik} \; \partial / \partial \, x_k$ to both sides of the last equation, and get

$$- \kappa_{ik} \frac{\partial^2 (p + U)}{\partial x_k \, \partial x_i} + \kappa_{ik} \; \eta_{ijmn} \frac{\partial^2 v_m}{\partial x_n \, \partial x_n \, \partial x_n} = 0 \tag{29}$$

or by (27)

$$\kappa_{ik} \; \eta_{ijmn} \frac{\partial^2 v_m}{\partial x_n \, \partial x_n \, \partial x_n} = 0$$

We look for a corrected seepage equation in the form

$$v_i = - \kappa_{ij} \frac{\partial (p + U)}{\partial x_j} + \lambda \; v_i^1 \tag{30}$$

where v^1 is a correction. We submit the expression (30) into Stokes' Equation (28) and receive

$$- \frac{\partial (p + U)}{\partial x_i} + \eta_{ijmn} \frac{\partial^2}{\partial x_j \; \partial x_n} \left(- \kappa_{mk} - \frac{\partial (p + U)}{\partial x_k} + \lambda \; v_m^1 \right) = 0$$

or

$$- \frac{\partial (p + U)}{\partial x_i} + \eta_{ijmn} \; \kappa_{mk} - \frac{\partial^3 (p + U)}{\partial x_j \; \partial x_n \; \partial x_k} + \eta_{ijmn} \frac{\partial^2 (\lambda \; v_m^1)}{\partial x_j \; \partial x_n} = 0 \tag{31}$$

If the vector r defined as

$$r_i \equiv \eta_{ijmn} \; \kappa_{mk} \frac{\partial^3 (p + U)}{\partial x_j \; \partial x_n \; \partial x_k} \tag{32}$$

vanishes, it is, if

$$r_i = 0 \tag{33}$$

Equation (31) takes the Stokesian form, cf. Equation (28),

$$-\frac{\partial(p + U)}{\partial x_i} + \eta_{ijmn} \frac{\partial^2(\lambda\ v_m^1)}{\partial x_i\ \partial x_n} = 0 \tag{34}$$

and we arrive at the situation, similar to that after Equation (9) for the isotropic problem. Thus, the velocity correction v^1 satisfies Darcy's type equation

$$\lambda\ v_i^1 = -\ \kappa_{ij} \frac{\partial(p + U)}{\partial x_j}$$

or, by (34)

$$\lambda\ v_i^1 = -\ \kappa_{ij}\ \eta_{kjmn} \frac{\partial^2 v_m}{\partial x_j\ \partial x_n} \tag{35}$$

Substitution into (30) gives

$$v_i = -\ \kappa_{ik} \left(\frac{\partial(p + U)}{\partial x_k} + \eta_{kjmn} \frac{\partial^2 v_m}{\partial x_j\ \partial x_n} \right) \tag{36}$$

what is a form of Brinkman's equation for seepage of an anisotropic fluid through a porous medium. But (36) was obtained with the assumption (33) only.

A discussion for cubic anisotropy of the fluid

For isotropic fluid

$$\eta_{ijmn} = \eta(\delta_{im}\delta_{jn} + \delta_{in}\delta_{jm}) + \left(\zeta + \frac{2}{3}\eta\right) \delta_{mn}\ \delta_{ij}$$

Thus, the number of non-zero moduli (the viscosities) for an isotropic fluid is two: η and ζ. We observe that now

$$\eta_{1111} - \eta_{1122} - 2\eta_{1212} = 0$$

The least number of non-zero moduli (the viscosity tensor components) for cubic anisotropy (the next most symmetric fluid after the isotropic one), obtained by a suitable choice of the co-ordinate axes is three (cf. LANDAU, LIFSHITZ 1970). We take the axes along the three fourth-order axes of symmetry. The symmetry is tetragonal, and there remain only three different moduli of viscosity: η_{1111}, η_{1122} and η_{1212}.

For the cubic symmetry the permeability tensor is isotropic (cf. LANDAU, LIFSHITZ 1970), it is $\kappa_{ij} = \kappa\,\delta_{ij}$ and the vector r defined by (32) is

$$r_i \equiv \kappa\,\eta_{ijkn} \frac{\partial^3 (p + U)}{\partial x_j\, \partial x_n\, \partial x_k}$$

For $i = 1$ and for the cubic symmetry of the tensor η_{ijmn} we get

$$r_1 = \kappa \frac{\partial}{\partial x_1} \left[\eta_{1111} \frac{\partial^2 (p + U)}{\partial x_1^2} + (2\eta_{1212} + \eta_{1122}) \left(\frac{\partial^2 (p + U)}{\partial x_2^2} + \frac{\partial^2 (p + U)}{\partial x_3^2} \right) \right] \quad (37)$$

and similar expressions for $i = 2$ and $i = 3$. Strictly speaking, only for an isotropic case, when

$$\eta_{1111} - 2\eta_{1212} - \eta_{1122}$$

the term in braces reduces to full Laplacian, but one may hope that components r_i, $i = 1,2,3$ can be neglected, when the difference $(\eta_{1111} - \eta_{1212} - 2\eta_{1122})$ is small. Thus, Brinkman's equation can be derived also for *nearly isotropic* fluids of cubic symmetry.

Conclusions

Applying an heuristic method of Born's approximation we have derived Brinkman's equation as a corrected Darcy's law. The derivation was given for isotropic Newtonian fluid for isotropic porous medium, with constant permeability, and with permeability linearly dependent on space coordinates. For anisotropic cubic fluids our methods works only in approximation.

Perhaps our method reconstructs Brinkman's reasoning. As it was mentioned in Introduction, the form of Brinkman's equation resembles somewise the time independent quantum wave equation, and Brinkman, who worked much in quantum physics surely knew Born's approximation method. Perhaps we have found the way of his arrival to his equation.

Appendix 1: Born's approximation

This method of successive approximation is a basic tool of calculus. It enables to solve a vast array of problems that other methods cannot handle. Also the scattering of particles on a potential $V(r)$ can be described by a successive approximation method, when we treat the potential as a perturbation. This is Born's approximation method (cf. also SAFRONO 2011, VALENTÍ 2014).

Time independent Schrödinger's wave equation can be written in the form

$$\Delta u + k^2 u - \lambda U(r)\, u = 0 \tag{38}$$

where

$$k^2 = \frac{2mE}{\mathrm{h}^2} \qquad \text{and} \qquad \lambda U = \frac{2mV}{\mathrm{h}^2}$$

Here k is a wave vector, $k = |k|$, and E is a total energy of the particle of the mass m. The parameter λ expresses the smallness of the disturbing term with the potential $V(r)$. The vector $r = (x, y, z)$ determines the position, and $r - |r|$. The value of the reduced Planck constant is: $\mathrm{h} = 1.054571800\ (13) \times 10^{-34}\ \mathrm{J \cdot s}$.

In zero-th approximation, it is for $\lambda = 0$ we have

$$u^0 = \mathrm{e}^{ikz}$$

as a solution of the equation

$$\Delta u^0 + k^2 u^0 = 0 \tag{39}$$

As the first approximation we take the sum

$$u = u^0 + \lambda u^1$$

We substitute this expression into (38) and after accounting for (39) we get

$$\Delta u_1 + k^2 u^1 = U(r)u^0 \tag{40}$$

This nonhomogeneous differential equation for the function u^1 has the general solution

$$u^1 = u^0 - \frac{1}{4\pi} \int \mathrm{d}\, r' \, \frac{\mathrm{e}^{ik}(r - r')}{|\, r - r' \,|} \, U(r') \, u^0(r')$$

The obtained result may be the starting point of the Born series.

In this example we see that in scattering theory and in particular in quantum mechanics, the Born approximation consists of taking the incident field in place of the total field as the *driving field* at each point in the scatterer.

Applications: The Born approximation is used in several different physical contexts.

In neutron scattering, the first-order Born approximation is almost always adequate, except for neutron optical phenomena like internal total reflection in a neutron guide, or grazing-incidence small-angle scattering.

The Born approximation has also been used to calculate conductivity in bilayer graphene (KOSHINO, ANDO 2006), and to approximate the propagation of long-wavelength waves in elastic media (GUBERNATIS et al. 1977).

Born's approximation conceived for scattering problems in quantum mechanics has been used extensively in seismological studies to describe seismic scattering by small-scale heterogeneities in the Earth. It is shown that geometrical ray effects, like the travel-time perturbation, ray bending and focusing, are contained within the Born scattering formalism, provided these effects are small (cf. HUDSON, HERITAGE 1981, COATES, CHAPMAN 1990).

Appendix 2: Meaning of Brinkman's effective viscosity

For the illustration of meaning of the effective viscosity η' in Brinkman's equation (2), let us consider steady flow of the liquid with a velocity v between two fixed parallel planes in the presence of a constant pressure gradient. It means that the pressure is a linear function of the coordinate x along the direction of flow. Let the exterior potential of volume forces vanish, $U = 0$. Hence

$$\frac{\partial p}{\partial x} \equiv - \gamma$$

where:
γ – constant.

We take one of these planes as the $x\ z$ – plane, with the x – axis in the direction of v. The distance between the planes is h, and the space for $-\infty < y < 0$ and $h < y < \infty$ is occupied by a porous medium with the permeability K and is permeated by the same liquid flowing under the same pressure gradient. It is clear that all quantities depend only on y, and that the fluid velocity is everywhere in the is x – direction. Thus, in the region $h > y > 0$ the flow is described by Stokes' equation

$$\frac{\mathrm{d}^2 v}{\mathrm{d}y^2} + \frac{\gamma}{\eta'} = 0 \tag{41}$$

The seepage in regions for $-\infty < y < 0$ and $h < y < \infty$ is described by Brinkman's equation

$$\frac{\mathrm{d}^2 v}{\mathrm{d}y^2} - \frac{\eta}{\eta' K}\, v + \frac{\gamma}{\eta'} = 0 \tag{42}$$

The integration of Equations (41) and (42) gives:

in the region $-\infty < y < 0$

$$v = b_1\, \mathrm{e}^{a\, y} + \frac{K}{\eta}\, \gamma$$

in the region $0 < y < h$

$$v = -\frac{\gamma}{2\ \eta}\, y^2 + Cy + C_1$$

and in the region $h < y < \infty$

$$v = b_2\, \mathrm{e}^{-ay} + \frac{K}{\eta}\, \gamma,$$

where

$$a = \sqrt{\frac{\eta}{\eta' K}} \tag{43}$$

Both solutions in the regions $-\infty < y < 0$ and $h < y < \infty$ vanish for $y \to -\infty$ and for $y \to \infty$, respectively.

The constants b_1, b_2, C and C_1 are determined from the boundary conditions for $y = 0$ and $y = h$ in which the continuity of the velocity field and the shear strain rates is assumed. The result is

$$C = \frac{\gamma}{2\eta} h,\ C_1 = \frac{\gamma}{\eta}\left(\frac{h}{2a} + K\right), \quad b_1 = \frac{\gamma}{2\eta}\frac{h}{a} \quad \text{and} \quad b_2 = \frac{\gamma}{2\eta}\frac{h}{a}\mathrm{e}^{ah}.$$

Thus, the solution in the region $0 < y < h$ reads

$$v = \frac{\gamma}{2\eta}\left(h\, y - y^2 + \frac{h}{2a} + K\right)$$

and for the case of not permeable walls, it is for $K \to 0$, and in consequence $a \to \infty$, cf. the formula (43),

$$v \to \frac{\eta}{2\eta}(h - y)\, y$$

what represents Hagen-Poiseuille's type flow in two dimensions (cf. LANDAU, LIFSHITZ 1987).

According to the formula (43) the influence of the effective viscosity η' is similar. Vanishing of η' leads to the infinite value of the constant a, and the immediate extinction of the exponential terms in the solutions. Then in the regions $-\infty < y < 0$ and $h < y < \infty$ Darcy's seepage is existing only.

References

BEAVERS G.S., JOSEPH D.D. 1967. *Boundary conditions at a naturally permeable wall*. Journal of Fluid Mechanics, 30(1): 197–207.

BORN M. 1926. *Quantenmechanik der Stossvorgange*. Zeitschrift für Physik, 37(12): 863–867.

BRINKMAN H.C. 1949. *A calculation of the viscous force exerted by a flowing fluid on a dense swarm of particles*. Applied Scientific Research, 1(1): 27–34.

BRINKMAN H.C. 1956. *Applications of spinor invariants in atomic physics*. Series in physics. North--Holland Publishing Co., Amsterdam.

BRINKMAN H.C., KRAMERS H.A. 1930. *Zur Theorie der Einfangung von Elektronen durch h – Teilchen*. Proceedings Koninklijke Akademie van Wetenschappen te Amsterdam, 33: 973–984.

COATES R.T., CHAPMAN C.H. 1990. *Ray perturbation theory and the Born approximation*. Geophysical Journal International, 100(3): 379–392.

DARCY H. 1856. *Les Fontaines publiques de la ville de Dijon*. Dalmont, Paris.

GUBERNATIS J.E., DOMANY E., KRUMHANSL J.A., HUBERMAN M. 1977. *The Born approximation in the theory of the scattering of elastic waves by flaws*. Journal of Applied Physics, 48(7): 2812–2819.

HUDSON J.A., HERITAGE J.R. 1981. *The use of the Born approximation in seismic scattering problems*. Geophysical Journal International, 66(1): 221–240.

KOSHINO M., ANDO TS. 2006. *Transport in bilayer graphene: Calculations within a self-consistent Born approximation*. Physical Review B, 73(24): 245–403.

LANDAU L.D., LIFSHITZ E.M. 1970. *Theory of elasticity*. Volume 7 of Course of Theoretical Physics, 2nd English ed. Translated from the Russian by J.B. Sykes, W.H. Reid. Pergamon Press, Oxford – New York – Toronto – Sydney – Paris – Braunschweig.

LANDAU L.D., LIFSHITZ E.M. 1987. *Fluid mechanics*. Volume 6 of Course of Theoretical Physics, 2nd English ed. Translated from the Russian by J.B. Sykes, W.H. Reid. Pergamon Press, Oxford – New York – Beijing – Frankfurt – Sa Paulo – Sydney – Tokyo – Toronto.

LÉVY Th. 1983. *Fluid flow through an array of fixed particles*. International Journal of Engineering Science, 21(1): 11–23.

MORSE M., FESHBACH H. 1953. *Methods of theoretical physics*. Part I. McGraw-Hill Book Company, New York – Toronto – London.

MORSE M., FESHBACH H. 1953. *Methods of theoretical physics*. Part II. McGraw-Hill Book Company, New York – Toronto – London.

RINKMAN H.C. 1947. *A calculation of the viscosity and the sedimentation constant for solutions of large chain molecules taking out account the hampered flow of solvent through these molecules*. Physica (Utrecht), 13(8): 447–448.

SAFRONO M. 2011. *The Born approximation*. Lecture 24. http://www.physics.udel.edu/~msafrono/425-2011/Lecture %2024.pdf

SANCHEZ-PALENCIA E. 1980. *Non-homogeneous media and vibration theory*. Springer Verlag, Berlin.

SANCHEZ-PALENCIA E. 1983. *On the asymptotics of the fluid array of fixed obstacles*. International Journal of Engineering Science, 20(12): 1291–301.

SHANKAR R. 1994. *Principles of quantum mechanics*. Second edition. Plenum Press, New York, London.

TAYLOR G.I. 1971. *A model for the boundary condition of a porous material*. Part 1. Journal of Fluid Mechanics, 49(2): 319–326.

VALDES-PARADA F.J., OCHOA-TAPIA J.A., ALVAREZ-RAMIREZ J. 2007. *On the effective viscosity for the Darcy-Brinkman equation*. Physica A, Statistical Mechanics and its Applications, 3851): 69–79.

VALENTI R. 2014. *Quantum mechanics II*. SS 2014, Institut fur Theoretische Physik, Universitat Frankfurt. http://itp.uni-frankfurt.de/~valenti/SS14/QMII_2014_chap1.pdf

WHITAKER S. 1999. *The method of volume averaging*. Kluwer Academic Publisher, Amsterdam.

WOJNAR R. 2014. *Flow of Stokesian fluid through a cellular medium and thermal effects*. Bulletin of the Polish Academy of Sciences: Technical Sciences, 62(2): 1–9.

Technical Sciences, 2017, 20(4), 375–389

UNIWERSYTET WARMIŃSKO-MAZURSKI W OLSZTYNIE

Quarterly peer-reviewed scientific journal

ISSN 1505-4675
e-ISSN 2083-4527

TECHNICAL SCIENCES

Homepage: www.uwm.edu.pl/techsci/

USE OF TECHNOLOGY BUILDING INFORMATION MODELING (BIM) IN THE DESIGN HIGH BUILDING BASED ON INNOVATIVE APPROACH DESIGN CAE/CAD

Elżbieta Pilecka, Dariusz Szwarkowski

Faculty of Civil Engineerin
Cracow University of Technology, Poland

Received 5 May 2017, accepted 7 September 2017, available online 2 October 2017.

Key words: BIM, CAE/CAD, MES, spatial model, reinforced concrete structure.

Abstract

BIM – Building Information Modeling is the fastest growing branch of modern design and execution of buildings. In the United States there is a requirement for the design of public investment based on BIM technology. Similar legislation has been in force since 2016 in the United Kingdom. In the near future also in Poland, it becomes necessary the use of BIM technology in the implementation of investments co-financed from European Union funds. The most important part in the design of a new approach is the treatment of structural parts of geometric models, as information which can be changed as desired at any stage of design. A comprehensive approach to design using BIM technology allows to carry out a series of analysis and collision detection at the design stage, in order to reduce costs at the stage of execution of the investment. The paper presents the design of the structural part of a reinforced concrete building, multi-storey in BIM technology. It uses an innovative design approach, enabling the analysis of the object using CAD (Computer Aided Design), which previously was based BIM method and a new approach based on the method of CAE (Computer Aided Engineering), which permit the object generated in BIM, static-strenght analysis. The article presents opportunities and benefits of BIM methods, using innovative design CAE/CAD.

Correspondence: Dariusz Szwarkowski, Wydział Inżynierii Lądowej, Politechnika Krakowska im. Tadeusza Kościuszki, ul. Warszawska 24, 31-155 Kraków, phone: 12 628 25 66, e-mail: dszwarkowski@pk.edu.pl

Introductions

BIM development

The use of BIM technology in the design stage of a construction project helps to reduce the total cost of the investment (TOMALA 2016). BIM technology with the ability to assess the quality of the solutions already at the modeling stage, the preparation of project documentation, significantly improves the quality of documentation and reduce errors. Several studies carried out in the US (TOMALA 2016) for various types of construction, showed a significant decrease in the overall cost of construction, in the case of an increase of 2–3% of the costs aimed at improving the design documentation. Despite the increase in initial costs, it contributes to the reduction of the cost to the value forecast, calculated as the difference between the value of fixed investments, and the actual costs in relation to the value predicted at the time of completion of the entire project (Fig. 1).

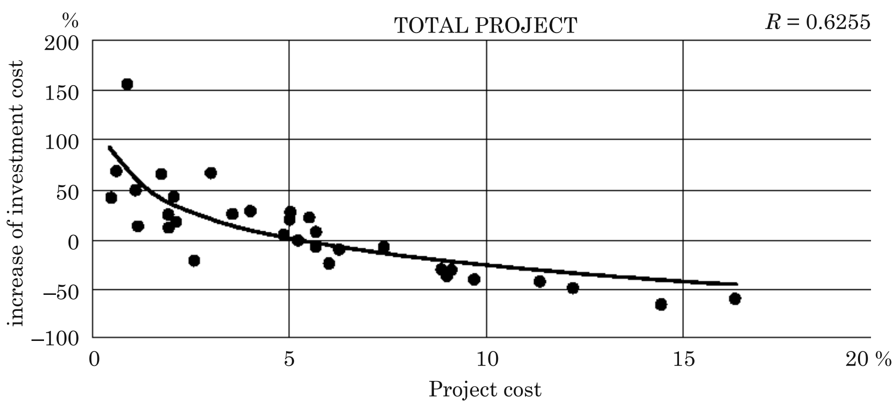

Fig. 1. The dependence of the increase initial costs, to the total cost of the project
Source: based on TOMALA (2016).

The use of BIM in the construction industry, will play an increasingly important due to the advantages of accurate design documentation. The dynamic development of the design using BIM can be observed in the US market in 2007–2012 (BIM 2012). For the past four years the share of use of BIM technology in the development of projects increased by 28% in 2008, up to 71% in 2012. This is related to the obligation to draw up documents in public procurement in the US, realized in BIM technology. In the UK, Germany and

France, the level of implementation of BIM in the public procurement system is similar and represented 36% (KIVINIEMI 2010).

BIM assumptions

BIM Technology is a building information model. It is also understoodas a parametric, computational representation of the model, combined with the various structural, finishing and installation elements. Made by designers, engineers, architects, contractors and subcontractors (TOMALA 2016). Also, the concept of BIM is defined as building information modeling, concerning its geometry, space, or estimating the cost of its construction. Means the process of creating and managing data from the whole life cycle of the project. Starting from the design phase and ending with the restoration of the object, or its liquidation. With each step, under the premise of BIM data should be provided to enable a comprehensive assessment of the behaviour of a building. Figure 2 illustrates the steps of data management of the different stages of life design. In addition to the existing management scheme 3D data also appear requirements for information management, the collection and processing in terms of

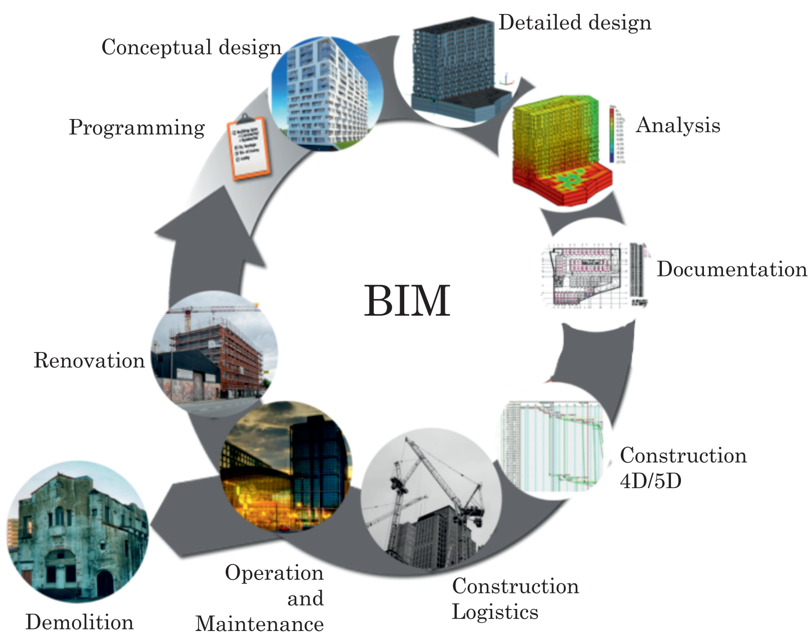

Fig. 2. The steps of data management in BIM from each life cycle structure
Source: own elaboration.

time associated with the analyzed object construction [4D models]. Also included data on cost management [5D models]. Also mentioned is the use of modeling 6D and 7D BIM technology in the management of the data appearing on the construction site (TOMALA 2016).

In BIM, an important role is played by the level of complexity of projects in construction (TOMALA 2016). The levels are the following:

– level 0: traditional concerns for the design, based on an manual preparation of project documentation, in the form of 2D drawings;

– level 1: Currently used in the preparation of project documentation, based on 2D and 3D models, developed specialized software, without sharing made them models;

– level 2: Development of design documentation occurs in electronic form and as BIM models for every industry project, which cooperate with creating construction project. Shared files for data exchange including 3D models, also taking into account the time duration of the construction process;

– level 3: It includes comprehensive documentation and documentation of BIM model, resulting from a combination of data from the models developed by individual industries. This represents the highest level of complexity of the project.

Follows from this that the use of BIM technology requires a comprehensive account of building structure, shape elements. It is associated with precise representation of building.

An additional assumption method of BIM is the level of detail of the object, determined by the document (BIMFORUM. 2013) according to the model drawn up on the basis of 5 criteria LOD (level of development). It is selected from the range LOD100 for graphically depicting a simple model, or by means of a symbol to LOD500 characterized highest degree of detail. Which take into account the actual dimensions of the object on the site, geometry, shape, orientation. Also, it is important here distinction between the use of project documentation, depending on the destination (visualization, simulation, calculation of static and endurance). The basic premise of BIM technology is also the possibility of free exchange of data files between the participants of the construction process, hence the requirements for data recording format in IFC standard (TOMALA 2016, Polish Ministry of Infrastructure and Construction. 2016).

The reason for the wider use of BIM in the design, and the whole process of the project construction, the legal provisions and European requirements governing the use of this method in the Member States (Directive 2014, TOMALA 2016). Arrangements laid by the European Commission, will need to implement investments co-financed from EU funds, using BIM technology. In the US, and also from the beginning of 2016 in the UK (Industrial Strategy

2012), all investments in the public procurement must be implemented using BIM technology.

A major problem is data exchange in the form of files. BIM uses among other the IFC format for recording and reading data. IFC format (Industry Foundation Class) is a format for data exchange between applications AEC (Architectural Engineering & Construction). Allows to save the same standard information about the project components. This format is obligatoryin public procurement, in many countries using this technology (including the US, Denmark, the Netherlands).

BIM in Polish conditions

In Poland, there are no clear regulations on the requirements, standards, and laws of governing investment implementation with the use of BIM technology. Taking the trend of the development BIM in other countries of the European Union and its popularity in the US, it is necessary to develop design standards with the use of BIM technology in Poland. Recent research carried out on behalf of the Polish Ministry of Infrastructure and Construction (2016) showed that more than half of the designers are interested in the implementation of BIM during create projects for the purposes of public procurement (Fig. 3).

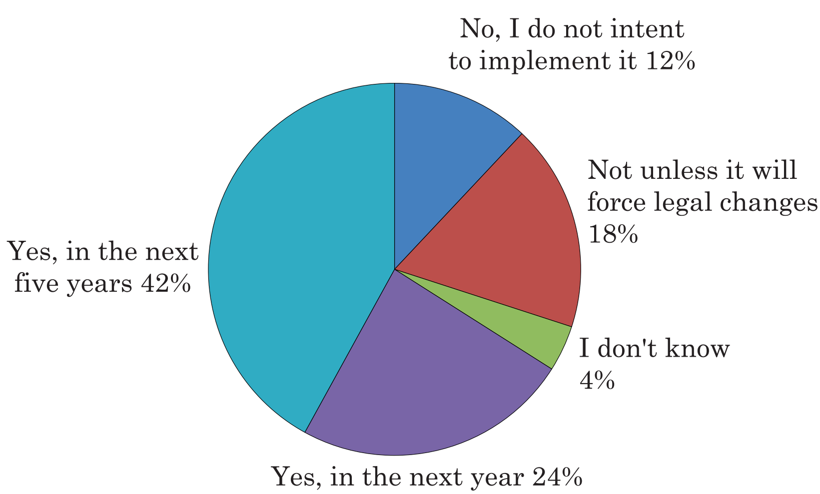

Fig. 3. Responses from a group of designers to the question: Does company considering investing in BIM technology in the future?
Source: based on *Building Information Modeling* (2016).

In the case of contractors, the majority of respondents also expressed interest in BIM technology. The main limitation is for contractors insufficient knowledge about new technology in the construction process (Fig. 4).

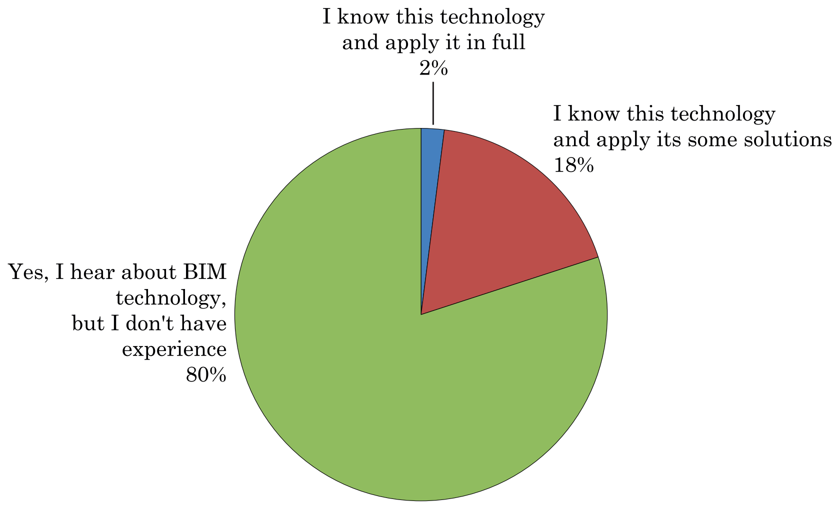

Fig. 4. Responses from a group of contractors to the question: Do you know the opportunity to use the BIM technology in the construction process. It is the technology of building information modeling, with the ability to design in 3D
Source: based on *Building Information Modeling* (2016).

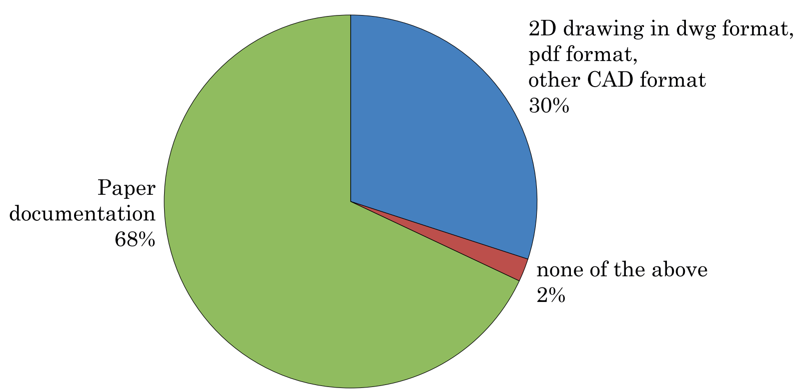

Fig. 5. Responses from a group of contractors to the question: In which form is most commonly transmitted design documentation in Mr./Ms company?
Source: based on *Building Information Modeling* (2016).

Also a major problem in the conditions of the Polish is a form of communication between designers and contractors. The research shows that the majority of respondents from the group of contractors said that dominates the paper documentations. Also 2D documentation in dwg format (Fig. 5).

From the data compiled in the research (*Building Information Modeling,* 2016) it shows that BIM technology has a good chance to improve the design process and cost management at all levels in the implementation a construction project. In the planning stage it is to use the experience of the UK and Finland (TOMALA 2016), in the correct definition of the model, data availability, interoperability between all participants in the construction process. The estimated cost of implementing BIM technology associated with the training of the participants a construction project (designers, contractors, sector specialists) will: 4.5 mld PLN. The costs of projects in the public procurement system in 2014 amounted to 133.2 mld PLN. Advantages of BIM confirmed in other countries where the technology has already been implemented, creating huge opportunities for effective use of funds from the state budget. This will allow the relocation of funds previously frozen on a particular investment.

BIM in high buildings

High buildings in the Polish regulations (PAWŁOSKI, CAŁA 2013) are constructions from 25 to 55 m height. The use of BIM in the design and da management with the implementation of high buildings, enables the capture of data from each cycle the emergence of a building. Take into account fixed and variable loads over time, staging construction, repeatable and unique segments. Define additional loads of scaffolding, masts, machines or stiffeners. BIM technology enables the collection and management of huge amounts of data from the construction process. It allows to take into account the orientation of the reinforcement element in reinforced concrete or seismic loads. The article presents of the possibilities of using BIM technology in the design of high buildings, based on a novel approach takes into account in a single project, both CAD models and analysis of static-strength CAE models based on the finite element method.

Conducted static and strength calculations of the building along with the analysis of the eigenvalues of the constructions. Analysis includes only the structural elements object. The application of BIM technology, along with a new approach to the design of CAE/CAD, realized on the example of the planned building “Mogilska Tower” in Cracow (Semaco Invest Group).

Material and methods

The analyzed building "Mogilska Tower" in Cracow, is a 15-storey building, with 3 additional underground levels, intended for car park. As one of the few in Cracow will be equipped with three-level underground car park. The planned investment has started in the spring of 2016 at the Mogilska street in Cracow. Construction has got a total height of 45 m a.s.l. The object serves as a multifamily residential building, with a separate service part on the ground floor. The building has a skeleton structure made of monolithic reinforced concrete supporting walls, pillars, floors and stairs as well as non load-bearing elements: walls of silicate blocks. Each floor plan is similar to each other. The values of material parameters, considered in the project were selected based on the standard (EN 1991-1-1:2002). The building visualization in presented at work SZWARKOWSKI, PILECKA (2017).

The adopted design assumptions in the model:

I. Geometry dimensions:
- the length of the building plan: 51 m; building width: 19.5 m,
- the length of the underground building plan: 51 m; underground building width: 56 m,
- supporting walls with monolithic reinforced concrete, 15 cm, 20 cm, 30 cm, 60 cm,
- walls of silicate blocks, 10 cm, 15 cm,
- slabs of monolithic reinforced concrete, 15 cm,
- stairs of monolithic reinforced concrete, gr. 15 cm.

II. Live loads (EN 1991-1-1:2002):
- living quarters, category A, qk1 = 2.0 kN/m^2,
- stairs, qk2 = 4.0 kN/m^2,
- balconies, qk3 = 2. kN/m^2,

III. Material properties (EN 1991-1-1:2002):
- volume weight of reinforced concrete elements, γc = 25 kN/m^3,
- volume weight of steel element, γs = 78 kN/m^3,
- volume weight of masonry elements from silicate blocks, γsil = 18 kN/m^3,

IV. Type of analysis

The modeling includes the analysis of linear-elastic model and eigenvalues. Results of the analysis will be used to generate internal forces in elements of the structural walls, lintels, beams and slabs and allow for the design of reinforcement by standard requirements (EN 1996-1-1:2005), (EN 1992-1--1:2008). According to the recommendations contained in (EN 1996-2:2006), elements of the structural walls, lintels, should be calculated taking account of the vertical loads, second order effects, eccentrics, depending on the location of walls cooperating with the slabs and walls stiffening. The project includes eccentric of individual components at the level of detail LOD3. The analysis was conducted in the Midas nGEN approach combining modeling with building CAD analysis (CAE method). FEM analysis of the object was carried out on the basis of flat finite elements. Adopted mesh size equal to 0.5 m. Adopted at the level of the foundation unmovable boundary conditions.

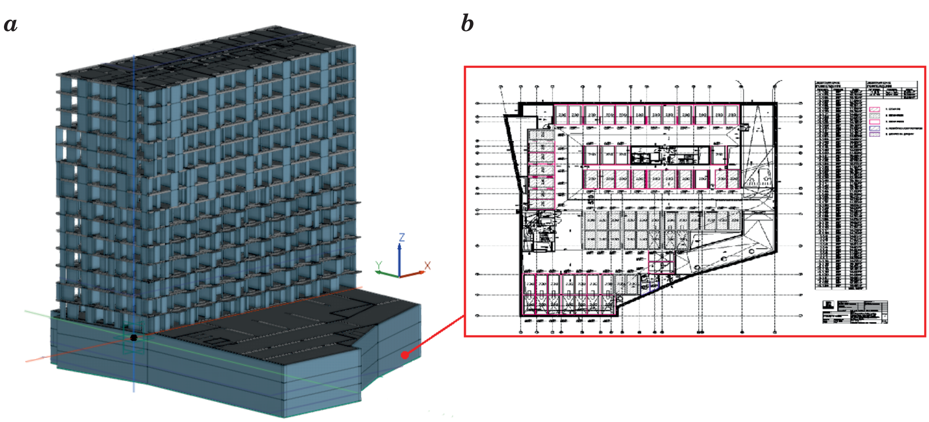

Fig. 6. Visualization model in program (*a*), underground floor of the building (*b*)
Source: own elaboration.

V. Dimensioning reinforcement

Elements of reinforced concrete, reinforced steel rods, designed based on (EN 1992-1-1:2008). The following assumptions:

- structural elements the aboveground part, f_{ck} = 25 MPa, for concrete class C25/30,
- structural elements the underground part, f_{ck} = 30 MPa, for concrete class C30/37,
- modulus of concrete, E_{cm} = 31 GPa, for strain ε_{c1} = 2.1%.
- reinforcing steel, f_{yk} = 400 MPa,

In the analysis of linear-elastic model was adopted reinforcing steel by Figure 7*a*.

At full nonlinear analysis, we should take advantage of the full characteristics of the stress-strain behavior of reinforcing steel and concrete. The building modeled in the Midas nGEN has the ability to export the model FEM programs take into account the full material nonlinearity.

- modulus of reinforcing steel, E_s = 200 GPa,
- minimum thickness of concrete cover, c_{nom} = 40 mm,

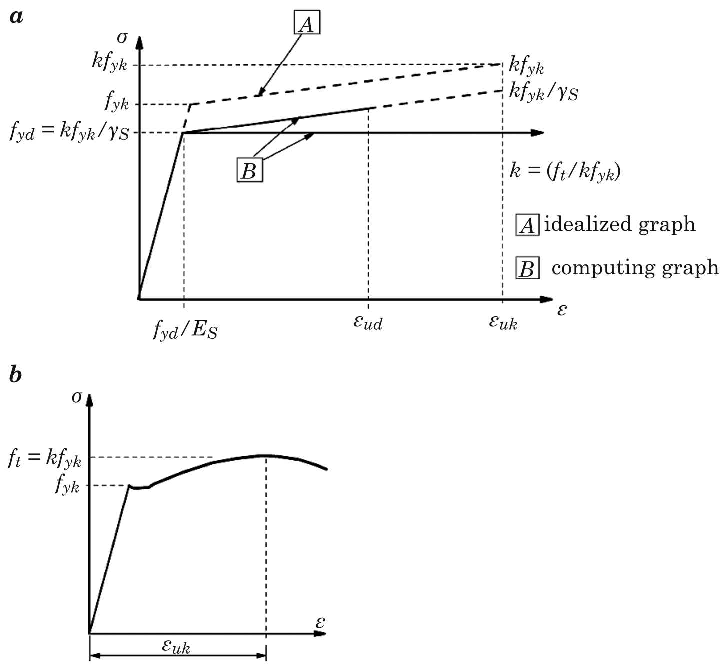

Fig. 7. Stress-strain graph of reinforcing steel, model in program (computing graph) (*a*), Stress-strain graph of a typical reinforcing steel (*b*)
Source: based on EN 1992-1-1:2008.

– the selection of the spacing rebar's was performed based on included requirements in EN 1992-1-1:2008.

VI. Serviceability Limit State (SLS)

Maximum deflection of model elements types: beams, plates, brackets, quasi static load should not be more than $f \leq L/250$, where L is the span element. Arrow deflection values can be determined on the basis of formulas contained in Eurocode 2 (EN 1992-1-1:2008). The maximum deflection of the highest parts of high building should not exceed $L/500$ (PAWŁOSKI, CAŁA 2013).

VII. Snow load

The characteristic values of snow load for a building modeled determined based on the standard (PAWŁOSKI, CAŁA 2013). The object is placed in Cracow, located in zone 2 of snow loads. The characteristic values of snow load of the building was set on the basis of the formula 1 with standard (EN 1991-1--4:2008):

$$s = \mu_i C_e C_t s_k = 0.96 \text{ kN/m}^2 \tag{1}$$

where:

μ_i – ratio of the roof shape, $\mu_i = 0.8$, flat roof,
s_k – characteristic value of snow loads, $s_k = 1.2$ kN/m^2,
C_e – exposure ratio, $C_e = 1.0$,
C_i – thermal ratio, $C_t = 1.0$.

VIII. Wind load

Wind load of the building was determined based on the standard (EN 1991-1-4:2008). It was assumed that wind direction operates in accordance with angle of 27 degrees to west elevation (Zone IX according to standard), and at an angle of 151 degrees to the south elevation (zone 6) (Fig. 8). The height of the building is equal 45 m. Overground floor plan has dimensions of 51 m × 19.5 m.

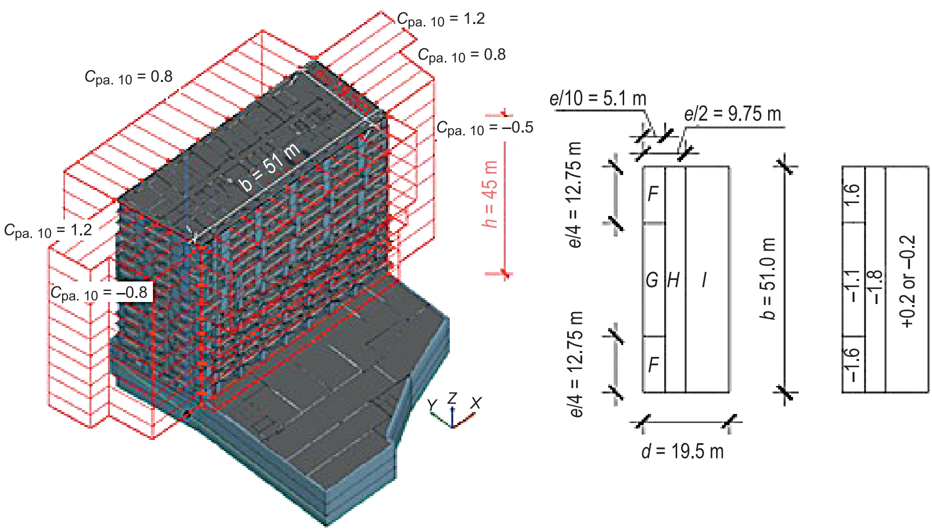

Fig. 8. Pressure peaks of wind speed, together with the distribution of external pressure $c_{pe,10}$
Source: own elaboration.

Calculation of the wind load object made according to standard (EN 1991-1-4:2008). Structural factor determined on the accordance with the logarithmic equation with standard (EN 1991-1-4:2008) and Article (ŻURAWSKI, GACZEK 2010) It assumes a fourth category of land for the urban area and the logarithmic decrement for concrete buildings equal to $\delta = 0.10$.

Results

Frequency and oscillation period of construction were chosen based on the first the form of vibrations generated by modeling (Fig. 9). Following show displacements of the building obtained for the first and second form of vibration.

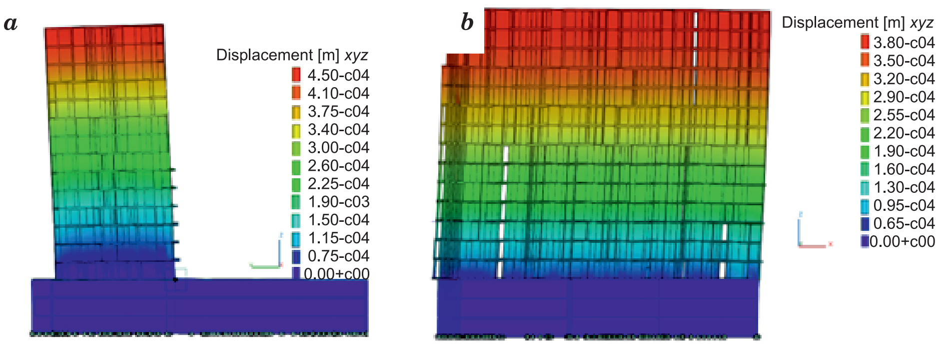

Fig. 9. First form of vibration model in the plane *zy*, for 2.71 Hz (*a*), second form of vibration model in the plane *zx*, for 3.01 Hz (*b*)
Source: own elaboration.

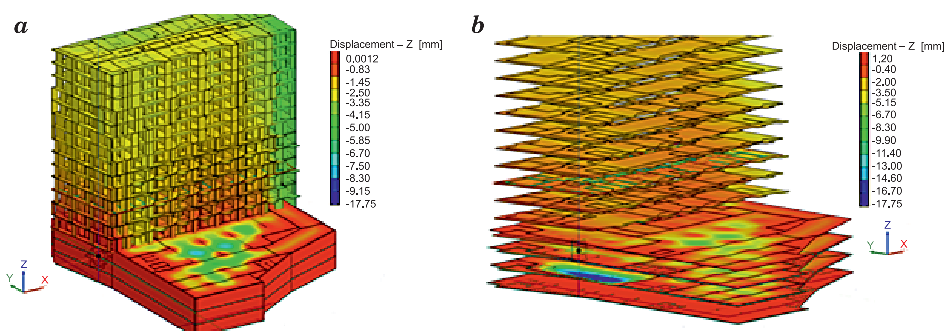

Fig. 10. Maximum vertical displacement building (*a*), maximum vertical displacement of slabs (*b*)
Source: own elaboration.

Figure 10*a* shows the vertical displacement of the building loaded with its own weight, live load and wind and snow loads. The obtained maximum vertical displacement slabs are equal 17.75 mm, and are lower than the limit value $L/250$ = 30 mm. In Figure 10*b* shows the maximum vertical slabs displacement.

Maximum vertical displacements lintels and substrings are equal 6 mm, and also meet the requirements of the SLS ($L/250$ = 27 mm).

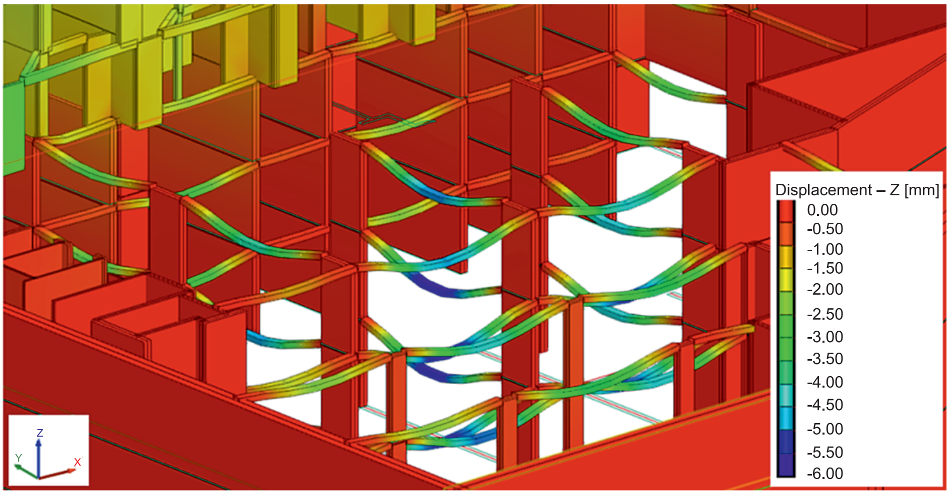

Fig. 11. Maximum vertical displacement of lintels and substrings
Source: own elaboration.

Figure 12*a* shows the horizontal displacements in the direction of x, in line with the greatest strength of wind pressure. While in Figure 12*b* shows the horizontal displacements in the direction of y. The value of horizontal displacements amounted to 2 mm in x-direction and 3.2 mm in the direction of y. Horizontal displacement value is less than the maximum value amounting to $H/900$ = 46 mm.

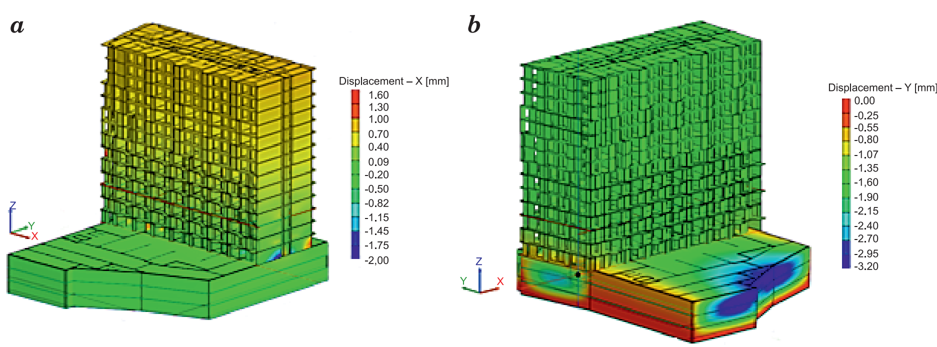

Fig. 12. Maximum horizontal displacement of construction in direction X (*a*), maximum horizontal displacement of construction in direction Y (*b*)
Source: own elaboration.

BIM technology allows the automatic generation of reports on the reinforcement and components used in the model. Parametric modeling of objects allows the changes made to the drawings are automatically included in the model space. Each element is defined in the project by the reference number (ID) to enable explicit definition of the model relative to other. This allows to optimize the structure of the arrangement of and the amounts of the reinforcing rebar sections or size of components.

Conclusion

The article highlighted the need for the implementation of the public procurement BIM in the design and preparation of project documentation and documentation which is updated at each stage of the construction process. The application of BIM technology shown on example model of high building "Mogilska Tower" in Cracow, which was modeled using a new approach taking into account both traditional modeling 3D CAD as well as direct analysis of static-strength using BIM. The application of design methods discussed in the article creates a lot of opportunities in the process faster and more efficient data management implemented building. Additional possibility of this technology is the ability to use dynamic data. The individual elements can be optimized at every stage of the project and are automatically included in the model. In addition, any change in dimension, cross section, reinforcement is also changed throughout the project. Due to the volume of the article, not included the possibility of optimal development of reinforcement for individual components, and it is also advantage of BIM. The enormous amount of data collected at each stage of the construction process offer opportunities for their M in Polish conditionsoptimal use. BIM technology allows their use. However, large amounts of data may cause that the site managers instead of being proficient engineers of construction, more time will have to spend an extra obligation to enter information into the database of the building.

References

Building Information Modeling. Ekspertyza dotycząca możliwości wdrożenia metodyki BIM w Polce. 2016. Polish Ministry of Infrastructure and Construction, KPMG Advisory Spółka z ograniczoną odpowiedzialnością sp.k., Warszawa.

Directive 2014/24/EU of the European Parliament and of the council of 26 February 2014 on public procurement and repealing Directive 2004/18/EC.

EN 1991-1-1:2002: Eurocode 1: *Actions on structures*. Part 1–1. *General Actions-Densities, self-weight, imposed loads for buildings*.

EN 1991-1-3:2005: Eurocode 1: *Actions on structures*. Part 1–3. *General actions-Snow loads*. Polish National Annex.

EN 1991-1-4:2008: Eurocode 1: *Actions on structures*. Part 1–4. *General actions-Wind actions*. Polish National Annex.

EN 1992-1-1:2008: Eurocode 2: *Design of concrete structures*. Part 1–1. *General rules and rules for buildings.*

EN 1996-1-1:2005: Eurocode 6: *Design of masonry structures*. Part 1–1. *General rules for reinforced and unreinforced masonry structures.*

EN 1996-2:2006: Eurocode 6: *Design of masonry structures*. Part 2. *Design considerations, selection of materials and execulation of masonry.*

Industrial Strategy. Government and industry in partnership, Building Information Modeling. 2012. HM Government, London.

KIVINIEMI A. 2010. *Proprietary vs open BIM-demand public project*. SCRI BIM Forum, School of the Built Environment.

Level of Development Specification. 2013. BIMForum.

PAWŁOSKI A.Z., CAŁA I. 2013. *Budynki wysokie*. Oficyna Wydawnicza Politechniki Warszawskiej, Warszawa.

Semaco Invest Group. Mogilska Tower. www.semaco-ig.pl/inwestycje/mogilska-tower/.

SZWARKOWSKI D., PILECKA E. 2017. *BIM technology in geotechnical engineering in terms of impact high building "Mogilska Tower" in Cracow of existing building development*. Technical Sciences, 20(3): 297–309.

TOMALA A. 2016. *BIM. Innowacyjna technologia w budownictwie. Podstawy, standardy, narzędzia*. PWB MEDIA, Kraków.

Value of BIM in North America Multi Year trend Analysis User Rating. 2012. BIM implementation the Business.

ŻURAWSKI J.A, GACZEK M. 2010. *Obciążenie wiatrem budynków w ujęciu normy PN-EN 1991-1-4:2008*. Inżynieria i Budownictwo, 9: 494–501.

Technical Sciences, 2017, 20(4), 391–404

Quarterly peer-reviewed scientific journal
ISSN 1505-4675
e-ISSN 2083-4527
TECHNICAL SCIENCES
Homepage: www.uwm.edu.pl/techsci/

SHEAR BEHAVIOR OF STEEL OR BASALT FIBER REINFORCED CONCRETE BEAMS WITHOUT STIRRUP REINFORCEMENT

Julita Krassowska, Marta Kosior-Kazberuk

Department of Building Structures
Faculty of Civil and Environmental Engineering
Bialystok University of Technology

Received 5 May 2017, accepted 24 September 2017, available online 2 October 2017

Key words: shear capacity, basalt fibers, steel fibers, SFRC; BFRC, two-span beams.

Abstract

The paper presents the results of a comprehensive investigation aimed at studying the shear behavior of basalt or steel fiber-reinforced concrete (BFRC or SFRC) beams, as well as analyzing the possibility of using basalt or steel fibers as a minimum shear reinforcement. Two-span reinforced concrete beams with the cross-section of 8×16 cm and length of 200 cm and diversified spacing of stirrups were tested. Steel stirrups or alternatively steel or basalt fibers were used as a shear reinforcement. Steel fiber content was 80 and 120 kg/m^3 and basalt fiber content was 2.5 and 5.0 kg/m^3. The shear behavior and/or bending capacity of SFRC and BFRC beams were studied. The result indicated that fibers can be safely used as a minimum shear reinforcement.

Introduction

The reinforced concrete (RC) beam with either little or no transverse reinforcement can fail prematurely in shear before reaching its full bending capacity. This type of shear failure is sudden in nature and usually catastrophic because it does not give ample warning. Beams are traditionally reinforced with stirrups to prevent shear failures. An alternative solution to stirrup reinforcement is the use of randomly oriented steel fibers, which cause

Correspondence: Julita Krassowska. Katedra Konstrukcji Budowlanych, Wydział Budownictwa i Inżynierii Środowiska, Politechnika Białostocka, ul. Wiejska 45E, 15-351 Białystok, e-mail: j.krassowska@pb.edu.pl

the increase in shear resistance (Dinh et al. 2010). Fibers are made from various materials e.g. steel, glass, carbon, basalt or synthetic material.

Concrete with evenly distributed steel fiber reinforcement is the homogeneous material (Jasiczak, Mikołajczak 2003). The shape and length of the steel fibers have a great influence on the bearing capacity of composite through adequate adhesion to the concrete. The use of steel fibers in bending elements causes the increase in resistance to cracking, prevents the development of shrinkage cracks and prevents brittle cracking of concrete through the quasi-plastic nature of the structure work. Property of concrete with the addition of steel fibers has the greatest influence on the tensile strength in bending. There was a lot of research on the use of concrete with fibers in Poland. Prefabricated heads regimes of slab pole made of fibers reinforced concrete were tested in the Silesian University of Technology. The studies showed the increase in their capacity to punching (Hulimka 2009). Pogan (2010) found that the addition of fibers in concrete structures leads to reduction in steel reinforcement bars, as well as to reduction of stirrup number. Research on the possibility of reducing shear reinforcement by adding steel fibers to concrete was carried out in the USA by Dinh et al. (2010).

Basalt fibers can also be used as reinforcement in concrete structures. Basalt is natural volcanic material, which is crushed and melted at a temperature 1300–1700°C, then squeezed using special probes into thin fibers. These fibers are coated with a polymer to provide adequate corrosion resistance. Their surface is irregular and rough. These fibers are resistant to corrosion, acidic and alkaline environment due to their chemical composition of the composite. Moreover, basalt fibers are resistant to high and low temperatures, the working temperature range of application ranges from -260°C to +750°C. The dimensions of the fibers are usually as follows: diameter 12 to 18 μ and length of 24–54 mm. Young's modulus of elasticity is in the range of 70–90 GPa, and a tensile strength is between 700–1680 MPa. The composite with this type of fibers is characterized by good mechanical properties (particularly tensile strength) (Kosior, Krassowska 2015). Composites with basalt fiber are used in special structures, such as housing nuclear reactors or facades of tall buildings (Jasiczak, Mikołajczak 2003). Basalt composites are used for production of ropes of hanging bridges. Abdulhadi (2014) studied the effect of basalt and polypropylene fibers and concluded that the compressive strength C30/37 concrete with two different type of fiber at different volume fraction. Ayub et al. (2014) studied the material properties of an economical HPFRC containing basalt fibers such as compressive strength, elastic modulus and tensile strength. Experimental results showed that the addition of basalt fibers up to 2% by volume together with mineral admixtures improved the compressive strength. The improvement in the strains corresponding to maximum compressive strength and splitting tensile strength results was observed at all fiber volumes, whereas there was a negligible influence of the fiber addition on the elastic modulus. SMRITI et al. (2013) presented study aims towards mechanical characterization of basalt fiber reinforced composite under compressive loading. The stress strain curve has been determined experimentally for optimal 0.5% volume fraction of basalt fiber reinforced composite and compared with that for unreinforced concrete. CORY et al. (2015) studied the use of basalt fiber bars as flexural reinforcement for concrete members and the use of chopped basalt fibers to enhance the mechanical properties of concrete. Test results indicate that flexural design of concrete members reinforced with basalt fiber bars should ensure compression failure and satisfying the serviceability requirements. ACI 440.1R-06 accurately predicts the flexural capacity of members reinforced with basalt bars, but it significantly underestimates the deflection at service load level. The use of chopped basalt fibers had little effect on the concrete compressive strength; however, it significantly enhanced its flexural strength. JIANG et al. (2014) analyzed the effects of the volume fraction and length of basalt fiber on the mechanical properties of FRC. The results showed that adding basalt fibers significantly improves the tensile strength, flexural strength and toughness index whereas the compressive strength showed no obvious increase. Furthermore, the length of basalt fibers presents an influence on the mechanical properties.

The experimental research on the shear behavior of SFRC beams has been conducted for the past three decades. Most of these test programs have investigated key parameters known to affect shear behavior, including shear span-to-effective depth ratio, longitudinal reinforcement ratio, fiber volume fraction, and concrete compressive strength. However, there are still parameters that have not been extensively investigated (DINH 2010).

The primary objective of the research was to study the shear behavior of double span beams and ultimate shear capacity of SFRC and BFRC beams without stirrup reinforcement and to analyze the possibility of using steel or basalt fibers as minimum shear reinforcement in RC beams.

Experimental program of testing mechanical properties of concrete with fibers

Material and sample preparation

The tests were performed on fine grained cement concrete. The cement (CEM I 42.5 R) content was constant – 320 kg/m^3 and the water to cement ratio of 0.50 was kept constant in all mixes. The river sand, fraction 0–2 mm and the natural aggregate with maximum diameter of 4 mm were used. The maximum size of aggregate was limited to reduce its influence on fracture properties and to provide the homogenous fibers distribution in concrete. The minimum size of sample exceeded the maximum size of aggregate more than tenfold.

Steel fibers (Fig. 1*a*) with hook-shaped ends with a length of 50 mm and a diameter of 1 mm were used for modification of concrete mix. They were characterized by tensile strength of 800 MPa. The test was performed for concrete mixtures with the steel fiber content of 80 and 120 kg/m^3.

The chopped basalt fiber (Fig. 1*b*) length was 50 mm and diameter of 20 μ. Fiber density was 2,650 kg/m^3. They were characterized by high tensile strength of 1680 MPa and Young's modulus of 90 GPa. The tests were carried out with the same composition of the cement matrix and diverse content of basalt fiber 2.5, 5.0 kg/m^3.

The fibres were added into concrete as a replacement of an adequate portion of aggregate by volume. The effect of fibres on mechanical properties was referee to the result obtained for reference concrete without fibres.

The dry aggregate was mixed with fibres followed by cement. The materials were dry mixed for 2 min before adding the water with superplasticizer. Mixing continued for further 4 min. The time of mixing was considered sufficient for the proper dispersion of fibres in the mix without causing a "balling" effect.

The specimens were vibrated in moulds and then stored under polyethylene cover for one day. After demoulding all specimens were cured in water at the temperature of 20±2°C till they were tested.

a ***b***

Fig. 1. The types of fiber used for testing: *a* – steel fibers, *b* – basalt fibers

Test methods

Compressive strength f_{ck}, flexural strength f_{ctm} and modulus of elasticity E_s of concretes with fibers were determined. Test of concrete compressive strength f_{ck} was performed according to standard PN-EN 12390-3 (2011) using cubic samples of size 100×100×100 mm. The flexural strength f_{ctm} was determined on samples of size 100×100×400 mm according to PN-EN 12390-5 (2011). Modulus of elasticity was determined according to PN-EN 12390-13 (2014), using cylindrical samples with a diameter of 150 mm and a depth of 300 mm.

Fracture behavior is the most important aspect of FRC. Nominal values of the material properties can be determined by performing a three-point bending test on a notched beam according to *fib* Model Code (2010).

The notched beams of size 100×100×400 mm were used in test. The initial saw-cut notch with a depth equal to 30 mm and width of 3 mm was located in the mid-span place. The geometry of sample and the way of load were presented in Figure 2.

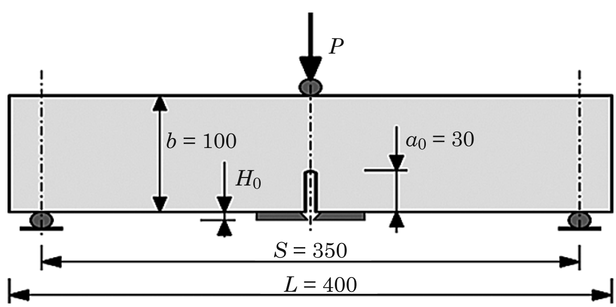

Fig. 2. Dimensions and method of load of test sample (in mm)

The universal testing machine (MTS 322) with closed loop servo control was used to achieve a stable failure of samples. The crack mouth opening displacement (CMOD) measured at the center of the notch was a feedback signal. The clip gauge was used to measure the CMOD values. The load – crack mouth opening displacement (P-CMOD) was determined for fracture behavior analysis in accordance with the general requirements of *fib* Model Code 2010.

Results

The test results of compressive strength f_{ck}, mean value of flexural strength of concrete f_{ctm} and modules of elasticity E_s determined after 28 days of curing were presented in Table 1. The steel fibers and basalt showed no significant effect on the compressive strength of concrete. A small increase in f_{ck} could be caused by scatter in the test results. The increase in flexural strength was 52% in the case of concrete with fibers in the amount of 120 kg/m^3. The increase in flexural strength f_{ctm} for concrete counting 5,0 kg/m^3 of basalt fibers was 47% in comparison to concrete without the fibers. Results of research of elastic modulus confirmed that the fibers do not significantly improve the elasticity of concrete.

Table 1

Mechanical properties of concrete with steel and basalt fibers

Type of fibers	Content of fiber	f_{ck}	Δf_{ck}	f_{ctm}	Δf_{ctm}	E_s	ΔE
	[kg/m^3]	[MPa]	[%]	[MPa]	[%]	[GPa]	[%]
Without fiber	0	28	–	4.01	–	28.59	–
Basalt fiber	2.5	30.8	10	5.13	27.93	33.5	17.17
	5.0	31.9	13.93	5.89	46.88	32.83	14.83
Steel fiber	80	29.01	3.61	5.49	36.91	30.53	6.79
	120	31.78	13.5	6.093	51.95	32.11	12.31

The characteristic curves of load P plotted versus CMOD for concretes with steel fibers and without fibers were presented in Figure 3.

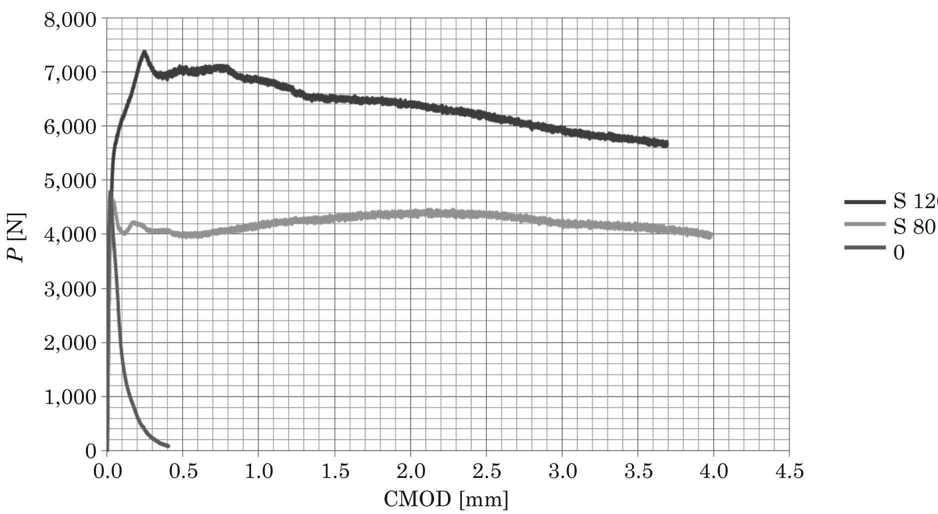

Fig. 3. Load P versus CMOD curves for concretes with various volume fraction of steel fibers and without fibers

The influence of steel fiber addition expresses itself by reaching a higher maximum ultimate load, larger displacement, and thus a larger area under the load-CMOD curve. In a typical load vs. CMOD diagram for sample under three-point loading, the material exhibits linear behavior up to its first crack stress (well marked first peak), a post-first-crack strain hardening phase up to its ultimate flexural load, and a post-ultimate-load phase. The descending parts of diagrams for concretes with different fiber dosage are characterized by apparent nonlinearity and significant scatter of test results. Both the strain softening and hardening were observed.

The characteristic curves of load *P* plotted versus CMOD with basalt fibers and without fibers were presented in Figure 4.

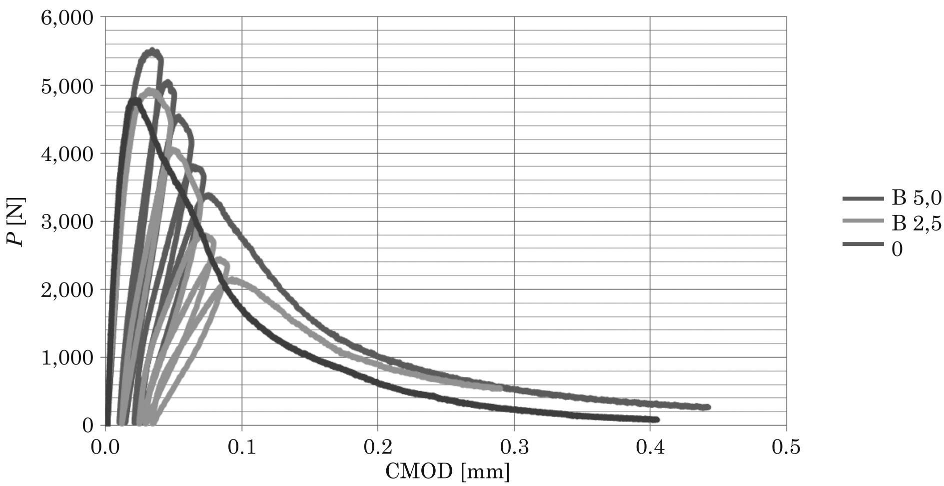

Fig. 4. Load *P* versus CMOD curves for concretes with various volume fractions of basalt fibers and without fibers

The analysis of *P*-CMOD plots for concretes with basalt fibers makes it possible to investigate the changes in concrete properties related to the loss of brittle material character. From the *P*-CMOD diagram, one can see that the initial parts of the curve for all concretes considered are almost linear and the strain of the notch tip under tension increases slightly with the increasing load. After the linear segment of *P*-CMOD curve, deviation from linear response is observed and the load reaches the maximum value, which indicates the onset of crack initiation at the tip of the notch. The increase in basalt fiber content causes the increase in the length of segment until reaching the peak. The crack mouth opening displacement, recorded for maximum load for individual samples, increased when the content of fiber increased. Generally, the $CMOD_{max}$ values for fiber reinforced concrete were greater than recorded for control concrete samples. However, the influence of basalt fiber content on the maximum load is not clear. The addition of fiber up to 2.5 kg/m^3 caused the increase in P_{max}, but further increase in fiber content up to 5.0 kg/m^3 caused the decrease in maximum load value.

Experimental program for testing model beams with basalt and steel fibers

Assumptions for the research program of model beams with mixed reinforcement

Five series of double-span model beams with dimensions of 80×180×2000mm were made. Each series contained five different elements of steel and basalt fiber, with different spacing of stirrups (Fig. 5).

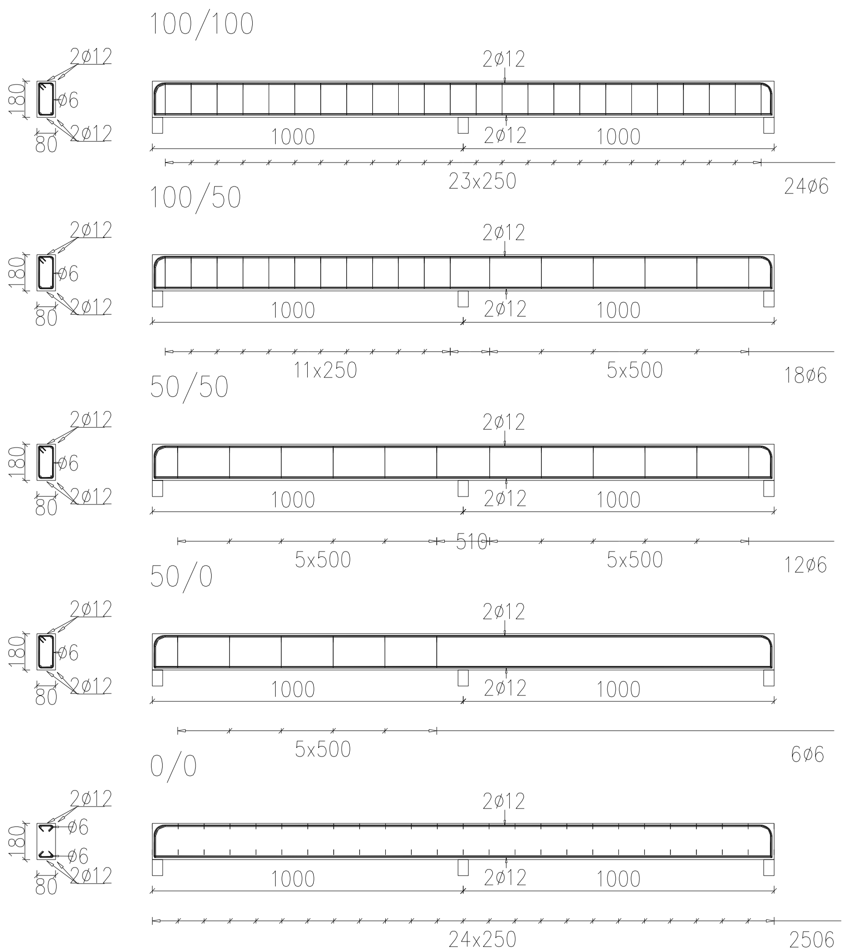

Fig. 5. The reinforcement of beams tested

Steel fibers in the amount of 80 and 120 kg/m^3 and the amount of basalt fibers in the amount of 2.5 and 5.0 kg/m^3 were chosen for testing the model beams. The reference beams of concrete without fibers were also prepared. Calculations of bending and shear reinforcement were performed in accordance with PN-EN 1992-1-1, assuming the force load concentrated in the center of each span. The bending reinforcement was identical in all beams tested and comprised two bars of Φ 12 mm (reinforcement degree of 0,8%) in each test series. A variable spacing of stirrups was used. The first series 100/100 was made with spacing stirrups calculated in accordance with EN 1992-1-1, and then for each series the stirrup spacing was reduced. In series 0/0 stirrup spacing was reduced to zero (beams without stirrups in both spans). The reinforcement of beams was shown in Figure 5.

The influence of fiber on the failure mode

Depending on the type of fibers used in each series, different ways of capacity loss have been observed. The failure mode is strongly dependent on the shear-span/depth ratio (a_v/d). The shear-span/depth ratio was 2.7 in tested beams, that means that beams should fail in shear. Tested elements have been destroyed by crushing the concrete in the compressive zone and large perpendicular cracks caused by bending in the beams of the series S100/100 with steel fibers in an amount of 120 kg/m^3 and B100/100 beams with basalt fibers in the amount of 5.0 kg/m^3 (in which stirrup shear reinforcement provided shear forces). In most cases, the failure was caused by shear in span with reduced spacing of the stirrups. Fail due to shear was similar in all tested beams. As the force increased, the cracks in the support zone would propagate towards the loading point, gradually becoming an inclined crack, which is known as a flexural-shear crack, but which is often referees to simple a diagonal crack. With further increases in force, the diagonals crack tends to stop. Then, near to longitudinal reinforcement random cracks start to occur. With the increase of force, the diagonal crack widens and propagates along the level of the tension reinforcement. The bond between the concrete and the steel was destructed. The beam was destroyed and collapsed. In case of RC beams the collapse was immediate with characteristic “crash” sound. In beams with the addition of steel fibers and basalt fibers destruction process proceeded in a gentle way. First, we observed significant increase in the deflection of beam mid span and an increase in crack width. Test elements with fiber reinforcement showed properties of quasi- plastic material. The beam after the uprising diagonal crack continued to carry loads. The examples of failure of beams were shown in Figure 6.

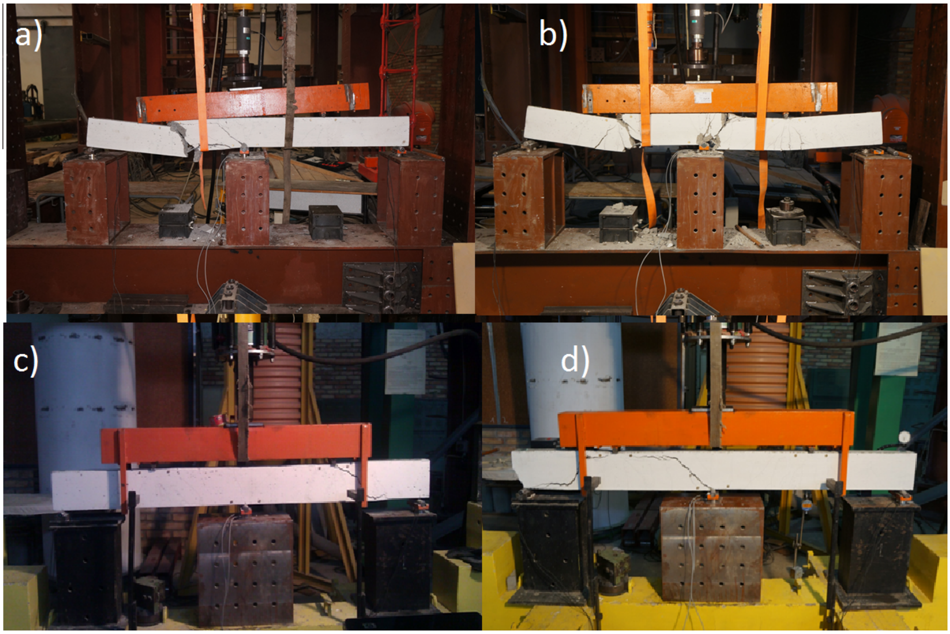

Fig. 6. Destruction of beams with steel fibers series: *a* – S80-50/0, *b* – S120-100/50/100 and basalt fibers, *c* – B2,5-50/50, *d* – B5,0-0/0

The effect of fibers on the shear capacity of beams

In the studies, reactions at the supports, as well as the total load of destruction were measured. The values of destructive forces and their increments compared to the values of the destructive forces for the reference beams (without fiber) were presented in Table 2. In the case of SFRC beams, the increase in destruction force volume was from 36.5% to 100.7%. In the case of BFRC the growth of destruction force was from 14.2% to 54.0%. The maximum increase in shear capacity was observed for beams of series S120-50/0. Beams series 50/50 with both basalt (5.0 kg/m^3) and steel (120 kg/m^3) fibers carried the same (or larger) destroying load as the beam series 100/100 without fiber only with stirrups reinforced.

The effect of fibers on support reactions

In test the dependence of the support reactions on the load in the tested beams series 50/0 (right span without stirrups, left span with stirrups in reduced spacing) was showed. Beams series 50/0 with addition of steel or basalt fibres and reference beam were presented in Figure 7.

Table 2

Destructive forces and their percentage increase for beams tested

Series	Beam with basalt fiber	Destructive force [KN]	Increase in force [%]	Beam with basalt fiber	Destructive force [KN]	Increase in force [%]
100/100	B0-100/100	80.6	–	S0-100/100	80.6	–
	B2.5-100/100	95.3	18.2	S1.0-100/100	110.0	36.5
	B5.0-100/100	106.7	32.4	S1.5-100/100	114.71	42.3
00/50	B0-100/50	57.8	–	S0-100/50	57.8	–
	B2.5-100/50	70.2	21.5	S1.0-100/50	93.4	61.6
	B5.0-100/50	75.3	30.3	S1.5-100/50	109.7	89.8
50/50	B0-50/50	60.7	–	S0-50/50	60.7	–
	B2.5-50/50	69.3	14.2	S1.0-50/50	64.1*	–
	B5.0-50/50	93.5	54.0	S1.5-50/50	102.7	69.2
50/0	B0-50/0	29.9	–	S0-50/0	29.9	–
	B2.5-50/0	33.5	12.0	S1.0-50/0	47.6	59.2
	B5.0-50/0	44.1	47.5	S1.5-50/0	60.0	**100.7**
0/0	B0-0/0	33.1	–	B0-0/0	33.1	–
	B2.5-0/0	37.9	14.5	S1.0-0/0	47.0	42.0
	B5.0-0/0	49.4	49.2	S1.5-0/0	52.8	59.5

* – beam was lateral-torsional buckling, 1 – beam was destroyed by bending

In the case of beam 50/0 without fibres, the all reactions with the increase in load had comparable values. The beam has been destroyed by shearing in the right span. There was only one main diagonal crack on the extreme support, which developed from the perpendicular cracks. The diagonal propagation was then followed in the direction of load application and in the direction of the level of the longitudinal reinforcement, and in the final stage also along the longitudinal reinforcement towards the support. The beams have been destroyed by shearing as a result of a sudden diagonal crack.

The beams of the series S120-50/0 or B5,0-50/0 have been destroyed at the centre support. The response on the centre support was much higher than for the rest of supports, meaning that most of the load has been transmitted by the centre support (here the plastic prosthesis has been created). For the series S120-50/0 in the initial phase of the load one can see the redistribution of transverse forces. After levelling forces at supports and cracks in the spans, the centre support took over the load transfer. In the beams of the series S120-50/0 or B5,0-50/0, the first cracks were orthogonal in the middle of the spans. As the load increased, more orthogonal cracks were created and their propagation at the sectional height took place. The slow and stabilized development of the perpendicular cracks was observed until diagonal crack appeared on the centre

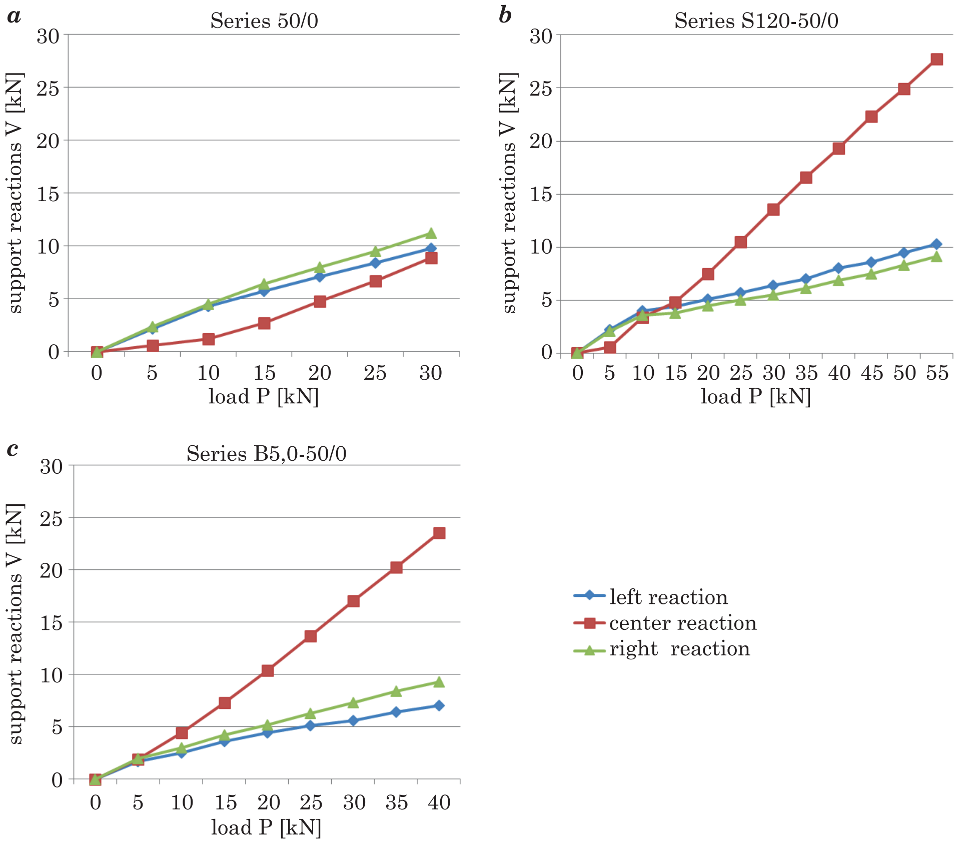

Fig. 7. A graph of the dependency of the support reaction to the load: *a* – 50/0 steel fibers, *b* – S120-50/0 and basalt fibers, *c* – B5,0-50/0

support at the side with reduced number of stirrups. Through the redistribution of internal forces, the central support has become the most loaded and external supports had similar values.

Conclusions

Steel fibers and basalt fibers had the slight impact on the compressive strength of concrete. In the case of flexural strength the changes were much bigger, for basalt fibers the maximum increase was 47% and for steel fiber similar increase was 51.95%.

The incorporation of considered volume fraction (2.5–5.0 kg/m^3) of thin, soft basalt fibers had an influence on concrete element improvement of pre-peak and post-peak behavior.

The stiff, hooked-end steel fibers (incorporated in the volume fraction of 80 and 120 kg/m^3) influenced concrete performance more efficiently than basalt fibers. The flexural tensile strength and the ductility increased with increasing fiber volume as expected. Steel fibers had relatively slight effect on pre-peak behavior of concrete samples. These parts of load-CMOD plot were more linear in comparison to plots obtained for basalt fiber reinforced concrete. In this phase, the steel fibers were particularly effective in the elimination of influence of pores and other microstructure defects on concrete sample behavior under load. The stable post-peak performance at larger CMOD values was dominated by the volume of steel fibers due to the presence of the hooks and its large embedded length.

Studies of double-span reinforced concrete beams showed the increase in shear capacity, increasing with the increase in fiber content. The increase in shear capacity for series tested was approx. 100% for steel fiber reinforcement and approx. 50% for basalt fiber. The lowest ultimate shear capacity for the SFRC and BFRC beams was still 2.5 and 1.5 times greater than that for the control RC beams. Although the lowest normalized shear strength for the beam series corresponded to one of the test beams with the smallest amount of fibers and reinforcement ratio (Beam 0/0). The results confirm the possibility of using the steel or basalt fibers as a minimum shear reinforcement in RC beams.

Acknowledgements

Studies have been carried out under the project ID 245084 funded by the National Centre for Research and Development.

References

Abdulhadi M. 2014. *A comparative Study of Basalt and Polypropylene fibres Reinforcement concrete on compressive and Tensile Behaviour*. International Journal of Engineering Trends and Technology, 300: 2231–5381.

ACI 440.1R-06 Guide for the Design and Construction of Structural Concrete Reinforced with FRP Bars.

Ajdukiewicz A., Walraven J. 2014. *Pre-norma konstrukcji betonowych*. Tom 1. *fib Model Code 2010*. Polski Cement Sp. z o.o., Kraków,

Ajdukiewicz A., Walraven J. 2014.. *Pre-norma konstrukcji betonowych*. Tom 2. *fib Model Code 2010*. Polski Cement Sp. z o.o., Kraków,

Ayub T., Shafiq N., Nuruddin M.F. 2014. *Mechanical Properties of High-Performance Concrete Reinforced with Basalt Fibers*. Fourth International Symposium on Infrastructure Engineering in Developing Countries, IEDC 2013. Procedia Engineering, 77: 131–139.

Dinh H.H. 2009. *Shear Behavior of steel fiber reinforced concrete beams without stirrup reinforcement*. Doctoral dissertation, Department of Civil and Environmental Engineering, University of Michigan, Ann Arbor, MI, Dinh H.H., Parra-Montesinos G.J., Wight J.K. 2010. *Shear Behavior of Steel Fiber-Reinforced Concrete Beams without Stirrup Reinforcement*. ACI Structural Journal/September-October.

High C., Seliem H.M., El-Safty A., Rizkalla S.H. 2015. *Use of basalt fibers for concrete structures*. Construction and Building Materials, 96: 37–46.

Hulimka J. 2009. *Strefa podporowa żelbetowego stropu płaskiego o podwyższonej nośności na przebicie*. Wydawnictwo Politechniki Śląskiej, Gliwice.

Jasiczak J., Mikołajczak P. 2003. *Technologia betonu modyfikowanego domieszkami i dodatkami*. Oficyna Wydawnicza Politechniki Poznańskiej, Poznań.

Jiang CH., Fan K., Wu F., Chen D. 2014. *Experimental study on the mechanical properties and microstructure of chopped basalt fibre reinforced concrete*. Materials and Design, 58: 187–193.

Kosior-Kazberuk M., Krassowska J. 2015. *Fracture behavior of basalt and steel fiber reinforced concrete*. Civil and Environmental Engineering, 6(2).

PN-EN 12390-13. 2014. *Testing hardened concrete. Determination of secant modulus of elasticity in compression*.

PN-EN 12390-3. 2011. *Testing hardened concrete. Compressive strength of test specimens.*

PN-EN 12390-5. 2011. *Testing hardened concrete. Flexural strength of test specimens*.

PN-EN 1992-1-1. 2008. Eurokod 2: *Projektowanie konstrukcji z betonu*. Część 1-1. *Reguły ogólne i reguły dla budynków*. PKN, Warszawa.

Pogan K. 2010. *Wzmacnianie konstrukcji kompozytami FRP*. Inżynier Budownictwa, http://www.inzynierbudownictwa.pl/technika,materialy_i_technologie,artykul,wzmacnianie_konstrukcji_kompozytami_frp,4178.

Raj S., Gopinath S., Iyer N.R. 2013. *Compressive behavior of Basalt Fiber Reinforced Composite*. Proc. of the Intl. Conf. on Advances in Civil, Structural and Mechanical Engineering, CSM.

Technical Sciences, 2017, 20(4), 405–413

Quarterly peer-reviewed scientific journal
ISSN 1505-4675
e-ISSN 2083-4527
TECHNICAL SCIENCES
Homepage: www.uwm.edu.pl/techsci/

AN EFFICIENT HARDWARE IMPLEMENTATION OF A COMBINATIONS GENERATOR

Tomasz Mazurkiewicz

Faculty of Cybernetics
Military University of Technology, Warszawa

Received 14 September 2017, accepted 24 September 2017, available online 2 October 2017.

Key words: information technology, generator of combinations, field programmable gate arrays.

Abstract

In this paper an area-efficient hardware implementation of a Bincombgen algorithm was presented. This algorithm generates all (n,k) combinations in the form of binary vectors. The generator was implemented using Verilog language and synthesized using Xilinx and Intel-Altera software. Some changes were applied to the original code, which allows our FPGA implementation to be more efficient than in the previously published papers. The usage of chip resources and maximum clock frequency for different values of n and k parameters are presented.

Introduction

The generation of combinatorial patterns is a well-known problem. KNUTH (2006) traces the history of this problem back to ancient China, India and Greece. Generation of (n, k) combinations has received much attention over the last couple of decades. Several algorithms were published in the 1960s. In those days a number of LEHMER articles (1960, 1964) attracted considerable interest. Since then, a number of algorithms were proposed (AKL 1987, CHEN, CHERN 1966, HOUGH, RUSKEY 1988, RUSKEY, WILLIAMS 2009, STOJMENOVIC 1992, TAKAOKA 1999, WEI 2014). Various applications of generators of combinations were found, e.g. parallel processing of combinatorial problems (KOKOSIŃSKI 1997b).

Correspondence: Tomasz Mazurkiewicz, Instytut Matematyki i Kryptologii, Wydział Cybernetyki, Wojskowa Akademia Techniczna, ul. Urbanowicza 2, 00-909 Warszawa, email: tomasz.mazurkiewicz@wat.edu.pl

KOKOSINSKI (1997a) proposed two algorithms called Combgen and Bincombgen. Both algorithms generate all (n, k) combinations using different combination representation: respectively conventional and binary. Especially the second one can be used to perform hardware mask/comparand vector generation efficiently.

This paper describes an area-efficient hardware implementation of Bincombgen algorithm. A basic model was implemented, which generates 1 combination per clock cycle. It takes $\binom{n}{k}$ clock cycles to generate all (n, k) combinations. We have obtained satisfactory results demonstrating that the generator can be efficiently implemented in a FPGA device. Our results are also compared to the results presented by BUBNIAK et al. (2004).

This paper is organized as follows. In the next section Bincombgen algorithm for generation of combinations is presented. In the third section details of its hardware implementation are described. Our results are compared to the results in the literature in Section 4. The last section contains a summary.

The algorithm description

Algorithm Bincombgen generates all (n, k) combinations in the form of n-bit binary vectors. A pseudocode of the algorithm is presented in Figure 1. Vectors are generated in a reverse lexicographic order in constant time per combination. In this paper some changes to the original algorithm were made to simplify hardware implementation. A modified pseudocode of the algorithm is presented in Figure 2. The order of operations as well as subsets of indexes for ONE2SUBSET operations have been changed. The potential gain on parallelization was presented in Figure 3. Operations in the same column can be done in parallel. Proposed modifications allows all operations in the generation phase to be performed in the same clock cycle in hardware implementation. It is possible since 3.1 and 3.3 operations can be done using combinatorial logic.

Table A and B are initialized at the same time. Table A is initialized by setting all (k) elements to 1. In the table B the first k bits are set to 1, while others $(n\text{-}k)$ are set to 0. This value will be used to generate first output vector. For example, if $n = 6$ and $k = 3$ the first generated vector will be 111000. At the same time S and IND registers are initialized. Initialization phase can be done in parallel (i.e. in one clock cycle).

```
//INITIALIZATION PHASE
1. MAX := n-k+1; IND := 1; S := 1;
2. do in parallel
   2.1. ONE2SUBSET(S, A, IND, k);
   2.2. ONE2SUBSET(0, B, 1, n);
3. do in parallel
   3.1. S := A(IND)+1;
   3.2. ONE2SUBSET(1, B, 1, k);
4. do in parallel
   4.1. output B;
   4.2. IND := k;
//GENERATION PHASE
5. while IND > 0 do
   5.1. do in parallel
        5.1.1. ONE2SUBSET(S, A, IND, K);
        5.1.2. v := IND+S;
   5.2. ONE2SUBSET(0, B, v-2, v-2);
   5.3. ONE2SUBSET(1, B, v-1, v-1);
   5.4. if A[IND] < MAX then
        5.4.1. S := A(IND)+1;
        5.4.2. if IND<k then
               5.4.2.1. do in parallel
                        5.4.2.1.1. ONE2SUBSET(0, B, v, n);
                        5.4.2.1.2. IND := k;
               5.4.2.2. ONE2SUBSET(1, B, v, IND+S-2);
     else
        5.4.3. IND := IND – 1;
        5.4.4. S := A(IND)+1;
   5.5. output B;

ONE2SUBSET(VALUE, SET, LEFT, RIGHT)
   for i:=LEFT to RIGHT
         do in parallel
               SET[i] := VALUE
```

Fig. 1. Pseudocode of the Bincombgen algorithm
Source: BUBNIAK et al. (2004).

In the generation phase values of A, B, S and IND change in parallel on the edge of CLK signal. All modifications of B can be applied in one clock cycle, because subsets of indexes for ONE2SUBSET operations are disjunctive. Bits from 1 to v-3 are left unchanged. Value of v is modified by combinational logic. Combinations are generated as long as.

Exemplary sequences generated by modified Bincombgen algorithm for $n = 6$ and $k = 3$ are presented in Table 1.

```
//INITIALIZATION PHASE
1. do in parallel
   1.1. MAX := n-k+1;
   1.2. ONE2SUBSET(1, A, 1, K);
   1.3. ONE2SUBSET(1, B, 1, K);
   1.4. ONE2SUBSET(0, B, K+1, N);
   1.5. IND := k;
   1.6. S := 2;
2. output B;
//GENERATION PHASE
3. while IND > 0 do
   3.1. v := IND + S;
   3.2. do in parallel
        3.2.1. ONE2SUBSET(S, A, IND, K);
        3.2.2. ONE2SUBSET(0, B, v-2, v-2);
        3.2.3. ONE2SUBSET(1, B, v-1, v-1);
        3.2.4. if S < MAX then
               3.2.4.1. if IND < k then
                        3.2.4.1.1. ONE2SUBSET(0, B, K+S, N);
                        3.2.4.1.2. ONE2SUBSET(1, B, v, K+S-1);
                        3.2.4.1.3. IND := k;
               3.2.4.2. S := S + 1;
         else
               3.2.4.3. S := A(IND) + 1;
               3.2.4.4. IND := IND – 1;
        3.3. output B;

ONE2SUBSET(VALUE, SET, LEFT, RIGHT)
        for i:=LEFT to RIGHT
                do in parallel
                        SET[i] := VALUE
```

Fig. 2. Modified pseudocode of the Bincombgen algorithm

Table 1

Sequences generated using (6,3) generator

No.	IND	S	A[1]	A[2]	A[3]	B (bin)	B (hex)
1	3	2	1	1	1	111000	38
2	3	3	1	1	2	110100	34
3	3	4	1	1	3	110010	32
4	2	2	1	1	4	110001	31
5	3	3	1	2	2	101100	2c
6	3	4	1	2	3	101010	2a
7	2	3	1	2	4	101001	29
8	3	4	1	3	3	100110	26
9	2	4	1	3	4	100101	25
10	1	2	1	4	4	100011	23
11	3	3	2	2	2	011100	1c
12	3	4	2	2	3	011010	1a

cont. table 1

No.	IND	S	A[1]	A[2]	A[3]	B (bin)	B (hex)
13	2	3	2	2	4	011001	19
14	3	4	2	3	3	010110	16
15	2	4	2	3	4	010101	15
16	1	3	2	4	4	010011	13
17	3	4	3	3	3	001110	0e
18	2	4	3	3	4	001101	0d
19	1	4	3	4	4	001011	0b
20	0	5	4	4	4	000111	07

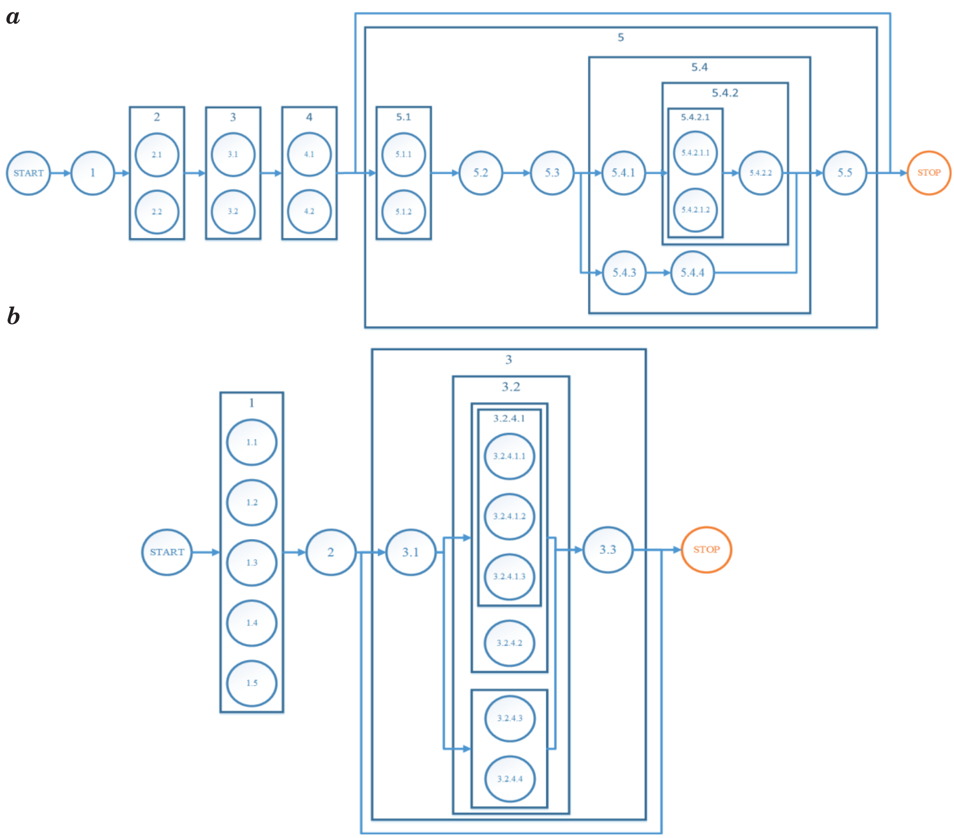

Fig. 3. Possible parallelization of original (*a*) and modified (*b*) pseudocode

Hardware implementation

Algorithm described in the section 2 was implemented using a basic model, which consists of singular registers B (of size n bits), S and IND and table A of size k. Each element of a table A is p bit wide, where $p = \lceil \log_2(\text{MAX}) \rceil$. In this model 1 output vector per clock cycle is generated. It makes an implementation small and compact and allows the device to work with high clock frequencies. Both n and k are the inputs of the algorithm, provided to the module as parameters, which can be modified during module instantiation. Such implementation can also be easily used to perform efficient hardware mask/comparand vector generation.

In order to compare our results with those described by BUBNIAK et al. (2004), similar interface was used (see Fig. 4). There are three input signals: CLK, RST_N and START. The first one is a clock signal. The second one is used to reset the generator if necessary. This input is negative-edge triggered. Signal START is used to start computations. In each clock cycle an output (OUT_DATA) of n bits is produced. Signal BUSY indicates that calculations are in progress.

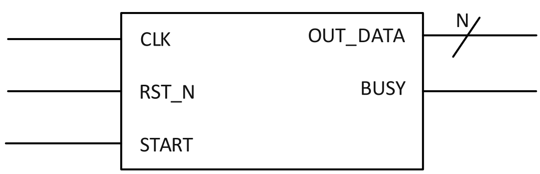

Fig. 4. Block diagram of the implemented generator

Described algorithm was implemented using Verilog language. Created generator of combinations was tested and verified using ISE Design Suite 14.7, Intel Quartus Prime 16.0 and ModelSim-Altera 10.4d. Test values were generated using software implementation of described algorithm that was created in Python.

To verify whether the implementation is producing correct results, the prototypes of the (6,3) and (20,10) generators were synthesized and loaded onto FPGA devices. Our experiments were carried out on two development kits:

– Terasic DE2-115 that features Altera (Intel-FPGA) Cyclone IV E device,
– Atlys Trainer Board that features Xilinx Spartan 6 device.

Results for (6,3) generator (implemented on the DE2-115 board), captured using SignalTap Logic Analyzer, are presented in Figure 5. Clock frequency for testing purpose was set to 50 MHz. All generated sequences are equal to values presented in Table 1.

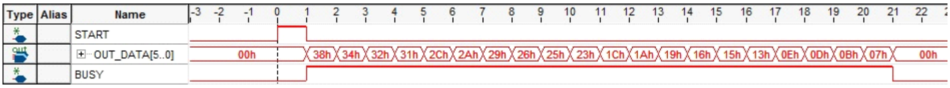

Fig. 5. Captured results for (6,3) generator

Table 2

Usage of resources and time parameters obtained from synthesis

(*n*, *k*)	Reference	Slices	4-input LUTs	Max. freq. [MHz]
(4, 2)	This paper	27	48	231.038
	Bubniak et al. 2004	665	1,276	35.155
(6, 3)	This paper	42	60	207.308
	Bubniak et al. 2004	948	1,835	28.395
(8, 4)	This paper	71	135	113.610
	Bubniak et al. 2004	1,144	2,193	29.428
(10, 5)	This paper	92	173	119.669
	Bubniak et al. 2004	1,422	2,734	32.505
(12, 6)	This paper	93	173	105.396
	Bubniak et al. 2004	1,658	3,196	31.614
(14, 7)	This paper	117	220	110.868
	Bubniak et al. 2004	1,891	3,630	31.387
(16, 8)	This paper	157	295	94.757
	Bubniak et al. 2004	2,099	4,028	31.114
(18, 9)	This paper	161	297	98.865
	Bubniak et al. 2004	2,408	4,628	30.146
(20, 10)	This paper	188	330	95.469
	Bubniak et al. 2004	2,715	5,233	29.273
(40, 20)	This paper	353	658	80.176
(60, 30)	This paper	506	937	79.399
(80, 40)	This paper	718	1,339	71.045

Generation of the combinations starts when START signal is driven high. In the following clock cycles consecutive combinations are generated, starting with 111000 (0×38). Output values change on the positive edge of CLK signal. Signal BUSY remains driven high as long as the generator produces next vectors. After completion of computations, BUSY is driven to a logical low and the value of OUT_DATA output is set to 000000. In case when START signal is driven high once more, all combinations are generated all over again.

Results

Results obtained from synthesis using ISE WebPACK 6.1 for XC2S100 device were presented by BUBNIAK et al. (2004). Unfortunately, this device in no longer available in ISE Design Suite 14.7. Therefore, newer Xilinx Spartan III XC3S50 was chosen as a target device. This device allows implementation to use up to 1536 4 input LUTs and 768 slices.

Usage of FPGA resources for several values of n and k ($k = n / 2$) are presented in Table 2. Additionally, maximum clock frequency was determined.

An implementation described by BUBNIAK et al. (2004) resulted in a high consumption of logical resources. Synthesis of generators for n>8 and k>4 was impossible in targeted XC2S100 device due to insufficient FPGA resources. In contradiction with those results, utilization level of the FPGA resources for our implementation is quite low. It is interesting to note that XC2S100 offers more logic resources than used in this paper XC3S50, i.e.1200 slices and 2400 4 input LUTs. However, in this paper different target device and newer version of software were used. Presented results thus need to be interpreted with caution.

In case of the smallest synthesized generator ($n = 4$, $k = 2$) around 3% of available resources is used. In case of the biggest one presented in the referenced literature ($n = 20$, $k = 10$) utilization level does not exceed 25%. Synthesis of (80,40) generator was possible and it did not exceed the size of the chip.

Summary

Implemented generator of combinations, based on Bincombgen algorithm, generates all (n, k) combinations in $\binom{n}{k}$ clock cycles. We have obtained satisfactory results demonstrating that the generator can be efficiently implemented in a FPGA device. A consumption of logical resources is quite low and maximum clock frequency is relatively high.

We believe our work will be helpful in a hardware implementation of linear decomposition algorithm (MAZURKIEWICZ, ŁUBA 2017). The hardware implementation of this algorithm require generating a discernibility matrix (stored in RAM). Generated values are then read from the memory and a possible linear decomposition is sought. Generator of combinations could be used to perform efficient memory addresses generation in this operation, since all n-bit vectors with Hamming weight equal to $k \in [2,n]$ must be generated.

References

AKL S.G. 1987. *Adaptive and Optimal Parallel Algorithms For Enumerating Permutations and Combinations*. The Computer Journal, 30: 433–436.

BUBNIAK G., GÓRALCZYK M., KARP M., KOKOSIŃSKI Z. 2004. *A Hardware Implementation of a Generator of (N,K)-Combinations*. IFAC Proceedings Volumes, 37(20): 228–231.

CHEN G.H., CHERN M.-S. 1966. *Parallel Generation of Permutations and Combinations*. BIT Numerical Mathematics, 26(3): 277–283.

HOUGH T., RUSKEY F. 1988. *An Efficient Implementation of the Eades, Hickey, Read Adjacent Interchange Combination Generation Algorithm*. Journal of Combinatorial Mathematics and Combinatorial Computing, 4:. 79–86.

KNUTH D.E. 2006. *The Art of Computer Programming*. 4, Fasc. 4, Addison-Wesley.

KOKOSIŃSKI Z. 1997a. *An Associative Processor for Multicomparand Parallel Searching and Its Selected Applications*. Proc. of Int. Conf. on Parallel and Distributed Processing Techniques and Applications PDPTA, pp. 1434–1442.

KOKOSIŃSKI Z. 1997b. *On Parallel Generation of Combinations in Associative Processor Architectures*. Proc. of IASTED Int. Conf. on Parallel and Distributed Systems Euro-PDS, pp. 283–289.

LEHMER D.H. 1960. *Teaching combinatorial tricks to a computer*. Proc. of Symposium Appl. Math, 10: 179–193.

LEHMER D.H. 1964. *The machine tools of combinatorics*. Applied combinatorial mathematics, pp. 5–31, John Wiley.

MAZURKIEWICZ T., ŁUBA T. 2017. *Redukcja liczby zmiennych do reprezentacji funkcji generowania indeksów*. Przegląd Telekomunikacyjny i Wiadomości Telekomunikacyjne, 8-9: 795–798.

RUSKEY F., WILLIAMS A. 2009. *The Coolest Way to Generate Combinations*. Discrete Mathematics, 309(17): 5305–5320.

STOJMENOVIC I. 1992. *A Simple Systolic Algorithm for Generating Combinations in Lexicographic Order*. Computers Math. Applic., 34(4): 61–64.

TAKAOKA T. 1999. *O(1) Time Algorithms for Combinatorial Generation by Tree Traversal*. The Computer Journal, 42(5): 400–408.

WEI Y. 2014. *The Grouping Combination Generating Algorithm*. Proc. of International Conference on Computer, Network Security and Communication Engineering, pp. 670–674.

Reviewers of Years – book 2017

Joseba Albizuri
Ugo Andreaus
Krystyna Araszkiewicz
Giuseppe Artese
Piotr Artiemjew
Francesco Aymerich
Riccardo Barzaghi
Tomasz Błachowicz
Michele Bottone
Ben Nathan Bridgens
Noemi Emanuela Cazzaniga
Ionica Circiu
Costin Chiru
Yalçın Coşkuner
Robertas Damasevicius
Ricardo Dias Martins de Carvalho
Paul Dobre
Vilis Dubrovskis
German Efremov
Ole Ellegaard
Mitra Fouladirad
Marcin Gabryel
Stefano Gialanella
Bülent Güzel
Tomasz Jeliński
Geert Haarlemmer
Adam Kawalec
Michał Knapik
Raju Krishnamurthy
Grzegorz Królczyk
Zbigniew Krzysiak
Jitendra Kumar Singh
Kamil Kwiatkowski
Magdalena Lahodova
Xingxing Li
Jan Limanowski
Xianfei Liu
Marco De Lorenzo
Daniela Lovarelli
Pavel Lukáč
Jordan Mackenzie
Algirdas Maknickas
Saeid Mehdizadeh
Darius Migilinskas
Maciej Mikulski
Ryszard Myhan
Krystyna Nagrodzka-Godycka
Juan J. Nieto
Aleksander Nowak
Yuriy Povstenko
Eypór Rafn Pórhallsson
Rahul V. Ralegaonkar
Bosko Rasuo
Marcelo S. Rocha
Vishakha Sakhare
Pavel Šimáček
Wojciech Sobieski
Dinara Sobola
Vlada Sokolovic
Jan Stabryła
Anita Strkalj
Piotr M. Szczypiński
Agnieszka Tajner-Czopek
Joel Thambi
Wojciech Tylman
Kosta Urumović
Sławomir Wierzbicki
Bertram Wolf
Marcin Woźniak
Boming Yu
Izabela Zamorska
Milan Zmindak

Guide for Autors

Introduction

Technical Sciences is a peer-reviewed research Journal published in English by the Publishing House of the University of Warmia and Mazury in Olsztyn (Poland). Journal is published continually since 1998. Until 2010 Journal was published as a yearbook, in 2011 and 2012 it was published semiyearly. From 2013, the Journal is published quarterly in the spring, summer, fall, and winter.

The Journal covers basic and applied researches in the field of engineering and the physical sciences that represent advances in understanding or modeling of the performance of technical and/or biological systems. The Journal covers most branches of engineering science including biosystems engineering, civil engineering, environmental engineering, food engineering, geodesy and cartography, information technology, mechanical engineering, materials science, production engineering etc.

Papers may report the results of experiments, theoretical analyses, design of machines and mechanization systems, processes or processing methods, new materials, new measurements methods or new ideas in information technology.

The submitted manuscripts should have clear science content in methodology, results and discussion. Appropriate scientific and statistically sound experimental designs must be included in methodology and statistics must be employed in analyzing data to discuss the impact of test variables. Moreover there should be clear evidence provided on how the given results advance the area of engineering science. Mere confirmation of existing published data is not acceptable. Manuscripts should present results of completed works.

There are three types of papers: a) research papers (full length articles); b) short communications; c) review papers.

The Journal is published in the printed and electronic version. The electronic version is published on the website ahead of printed version of Technical Sciences.

Technical Sciences does not charge submission or page fees.

Types of paper

The following articles are accepted for publication:

Reviews

Reviews should present a focused aspect on a topic of current interest in the area of biosystems engineering, civil engineering, environmental engineering, food engineering, geodesy and cartography, information technology, mechanical engineering, materials science, production engineering etc. They should include all major findings and bring together reports from a number of sources. These critical reviews should draw out comparisons and conflicts between work, and provide an overview of the 'state of the art'. They should give objective assessments of the topic by citing relevant published work, and not merely present the opinions of individual authors or summarize only work carried out by the authors or by those with whom the authors agree. Undue speculations should also be avoided. Reviews generally should not exceed 6,000 words.

Research Papers

Research Papers are reports of complete, scientifically sound, original research which contributes new knowledge to its field. Papers should not exceed 5,000 words, including figures and tables.

Short Communications

Short Communications are research papers constituting a concise description of a limited investigation. They should be completely documented, both by reference list, and description of the experimental procedures. Short Communications should not occupy more than 2,000 words, including figures and tables.

Letters to the Editor

Letters to the Editor should concern with issues raised by articles recently published in scientific journals or by recent developments in the engineering area.

Contact details for submission

The paper should be sent to the Editorial Office, as a Microsoft Word file, by e-mail: techsci@uwm.edu.pl

Referees

Author/authors should suggest, the names, addresses and e-mail addresses of at least three potential referees. The editor retains the sole right to decide whether or not the suggested reviewers are used.

Submission declaration

After final acceptance of the manuscript, the corresponding author should send to the Editorial Office the author's declaration. Submission of an article implies that the work has not been published previously (except in the form of an abstract or as part of a published lecture or academic thesis or as an electronic preprint), that it is not under consideration for publication elsewhere, that publication is approved by all authors and tacitly or explicitly by the responsible authorities where the work was carried out, and that, if accepted, it will not be published elsewhere in the same form, in English or in any other language.

To prevent cases of ghostwriting and guest authorship, the author/authors of manuscripts is/are obliged to: (i) disclose the input of each author to the text (specifying their affiliations and contributions, i.e. who is the author of the concept, assumptions, methods, protocol, etc. used during the preparation of the text); (ii) disclose information about the funding sources for the article, the contribution of research institutions, associations and other entities.

Language

Authors should prepare the full manuscript i.e. title, abstract and the main text in English (American or British usage is accepted). Polish version of the manuscript is not required.

The file type

Text should be prepared in a word processor and saved in doc or docx file (MS Office).

Article structure

Suggested structure of the manuscript is as follows:

Title
Authors and affiliations
Corresponding author
Abstract
Keywords
Introduction
Material and Methods
Results and Discussion
Conclusions

Acknowledgements (*optional*)
References
Tables
Figures

Subdivision – numbered sections

Text should be organized into clearly defined and numbered sections and subsections (optionally). Sections and subsections should be numbered as 1. 2. 3. then 1.1 1.2 1.3 (then 1.1.1, 1.1.2, ...). The abstract should not be included in numbering section. A brief heading may be given to any subsection. Each heading should appear on its own separate line. A single line should separate paragraphs. Indentation should be used in each paragraph.

Font guidelines are as follows:
– Title: 14 pt. Times New Roman, bold, centered, with caps
– Author names and affiliations:12 pt. Times New Roman, bold, centered, italic, two blank line above
– Abstract: 10 pt. Times New Roman, full justified, one and a half space. Abstract should begin with the word Abstract immediately following the title block with one blank line in between. The word Abstract: 10 pt. Times New Roman, centered, indentation should be used
– Section Headings: Not numbered, 12 pt. Times New Roman, bold, centered; one blank line above
– Section Sub-headings: Numbered, 12 pt. Times New Roman, bold, italic, centered; one blank line above
– Regular text: 12 pt. Times New Roman, one and a half space,full justified, indentation should be used in each paragraph

Title page information

The following information should be placed at the first page:

Title

Concise and informative. If possible, authors should not use abbreviations and formulae.

Authors and affiliations

Author/authors' names should be presented below the title. The authors' affiliation addresses (department or college; university or company; city, state and zip code, country) should be placed below the names. Authors with the same affiliation must be grouped together on the same line with affiliation information following in a single block. Authors should indicate all affiliations with a lower-case superscript letter immediately after the author's name and in front of the appropriate address.

Corresponding author

It should be clearly indicated who will handle correspondence at all stages of refereeing and publication, also post-publication process. The e-mail address should be provided (footer, first page). Contact details must be kept up to date by the corresponding author.

Abstract

The abstract should have up to 100-150 words in length. A concise abstract is required. The abstract should state briefly the aim of the research, the principal results and major conclusions. Abstract must be able to stand alone. Only abbreviations firmly established in the field may be eligible. Non-standard or uncommon abbreviations should be avoided, but if essential they must be defined at their first mention in the abstract itself.

Keywords

Immediately after the abstract, author/authors should provide a maximum of 6 keywords avoiding general, plural terms and multiple concepts (avoid, for example, 'and', 'of'). Author/authors should be sparing with abbreviations: only abbreviations firmly established in the field may be eligible.

Abbreviations

Author/authors should define abbreviations that are not standard in this field. Abbreviations must be defined at their first mention there. Author/authors should ensure consistency of abbreviations throughout the article.

Units

All units used in the paper should be consistent with the SI system of measurement. If other units are mentioned, author/authors should give their equivalent in SI.

Introduction

Literature sources should be appropriately selected and cited. A literature review should discuss published information in a particular subject area. Introduction should identify, describe and analyze related research that has already been done and summarize the state of art in the topic area. Author/authors should state clearly the objectives of the work and provide an adequate background.

Material and Methods

Author/authors should provide sufficient details to allow the work to be reproduced by other researchers. Methods already published should be indicated by a reference. A theory should extend, not repeat, the background to the article already dealt within the Introduction and lay the foundation for further work. Calculations should represent a practical development from a theoretical basis.

Results and Discussion

Results should be clear and concise. Discussion should explore the significance of the results of the work, not repeat them. A combined Results and Discussion section is often appropriate.

Conclusions

The main conclusions of the study may be presented in a Conclusions section, which may stand alone or form a subsection of a Results and Discussion section.

Acknowledgements

Author/authors should include acknowledgements in a separate section at the end of the manuscript before the references. Author/authors should not include them on the title page, as a footnote to the title or otherwise. Individuals who provided help during the research study should be listed in this section.

Artwork
General points

– Make sure you use uniform lettering and sizing of your original artwork
– Embed the used fonts if the application provides that option

– Aim to use the following fonts in your illustrations: Arial, Courier, Times New Roman, Symbol
– Number equations, tables and figures according to their sequence in the text
– Size the illustrations close to the desired dimensions of the printed version

Formats

If your electronic artwork is created in a Microsoft Office application (Word, PowerPoint, Excel) then please supply 'as is' in the native document format

Regardless of the application used other than Microsoft Office, when your electronic artwork is finalized, please 'Save as' or convert the images to one of the following formats (note the resolution requirements given below):

EPS (or PDF): Vector drawings, embed all used fonts

JPEG: Color or grayscale photographs (halftones), keep to a minimum of 300 dpi

JPEG: Bitmapped (pure black & white pixels) line drawings, keep to a minimum of 1000 dpi or combinations bitmapped line/half-tone (color or grayscale), keep to a minimum of 500 dpi

Please **do not**:
– Supply files that are optimized for screen use (e.g., GIF, BMP, PICT, WPG); these typically have a low number of pixels and limited set of colors
– Supply files that are too low in resolution
– Submit graphics that are disproportionately large for the content

Color artwork

Author/authors should make sure that artwork files are in an acceptable format (JPEG, EPS PDF, or MS Office files) and with the correct resolution. If, together with manuscript, author/authors submit color figures then Technical Sciences will ensure that these figures will appear in color on the web as well as in the printed version at no additional charge.

Tables, figures, and equations

Tables, figures, and equations/formulae should be identified and numbered consecutively in accordance with their appearance in the text.

Equations/mathematical and physical formulae should be presented in the main text, while tables and figures should be presented at the end of file (after References section). Mathematical and physical formulae should be presented in the MS Word formula editor.

All types of figures can be black/white or color. Author/authors should ensure that each figure is numbered and has a caption. A caption should be placed below the figure. Figure must be able to stand alone (explanation of all symbols and abbreviations used in figure is required). Units must be always included. It is noted that figure and table numbering should be independent.

Tables should be numbered consecutively in accordance with their appearance in the text. Table caption should be placed above the table. Footnotes to tables should be placed below the table body and indicated with superscript lowercase letters. Vertical rules should be avoided. Author/authors should ensure that the data presented in tables do not duplicate results described in figures, diagrams, schemes, etc. Table must be able to stand alone (explanation of all symbols and abbreviations used in table is required). Units must be always included. As above, figure and table numbering should be independent.

References

References: All publications cited in the text should be presented in a list of references following the text of the manuscript. The manuscript should be carefully checked to ensure that the spelling of authors' names and dates of publications are exactly the same in the text as in the reference list. Authors should ensure that each reference cited in the text is also present in the reference list (and vice versa).

Citations may be made directly (or parenthetically). All citations in the text should refer to:

1. Single author

The author's name (without initials, with caps, unless there is ambiguity) and the year of publication should appear in the text

2. Two authors

Both authors' names (without initials, with caps) and the year of publication should appear in the text

3. Three or more authors

First author's name followed by et al. and the year of publication should appear in the text

Groups of references should be listed first alphabetically, then chronologically.

Examples:

"... have been reported recently (ALLAN, 1996a, 1996b, 1999; ALLAN and JONES, 1995). KRAMER et al. (2000) have recently shown..."

The list of references should be arranged alphabetically by authors' names, then further sorted chronologically if necessary. More than once reference from the same author(s) in the same year must be identified by the letters "a", "b", "c" etc., placed after the year of publication.

References should be given in the following form:

KUMBHAR B.K., AGARVAL R.S., DAS K. 1981. *Thermal properties of fresh and frozen fish*. International Journal of Refrigeration, 4(3), 143–146.

MACHADO M.F., OLIVEIRA F.A.R., GEKAS V. 1997. *Modelling water uptake and soluble solids losses by puffed breakfast cereal immersed in water or milk*. In Proceedings of the Seventh International Congress on Engineering and Food, Brighton, UK.

NETER J., KUTNER M.H., NACHTSCHEIM C.J., WASSERMAN W. 1966. *Applied linear statistical models* (4th ed., pp. 1289–1293). Irwin, Chicago.

THOMSON F.M. 1984. *Storage of particulate solids*. In M. E. Fayed, L. Otten (Eds.), Handbook of Powder Science and Technology (pp. 365–463). Van Nostrand Reinhold, New York.

Citation of a reference as 'in press' implies that the item has been accepted for publication.

Note that the full names of Journals should appear in reference list.

Submission checklist

The following list will be useful during the final checking of an article prior to the submission. Before sending the manuscript to the Journal for review, author/authors should ensure that the following items are present:

– Text is prepared with a word processor and saved in DOC or DOCX file (MS Office). One author has been designated as the corresponding author with contact details: e-mail address

– Manuscript has been 'spell-checked' and 'grammar-checked'

– References are in the correct format for this Journal

– All references mentioned in the Reference list are cited in the text, and vice versa

– Author/authors does/do not supply files that are too low in resolution

– Author/authors does/do not submit graphics that are disproportionately large for the content